

UC Santa Barbara

UC Santa Barbara Electronic Theses and Dissertations

Title

Instrument and Method development for High Field Dynamic Nuclear Polarization with Magic Angle Spinning Spectroscopy at 25 K

Permalink

<https://escholarship.org/uc/item/0kj7p95q>

Author

Smith, Alicia

Publication Date

2017

Peer reviewed|Thesis/dissertation

UNIVERSITY OF CALIFORNIA

Santa Barbara

Instrument and Method development for High Field Dynamic Nuclear Polarization with
Magic Angle Spinning Spectroscopy at 25 K

A dissertation submitted in partial satisfaction of the
requirements for the degree Doctor of Philosophy
in Chemistry

by

Alicia Smith Lund

Committee in charge:

Professor Songi Han, Chair

Professor Bradley Chmelka

Professor Frederick Dahlquist

Professor Mark Sherwin

September 2017

The dissertation of Alicia Lund is approved.

Bradley Chmelka

Frederick Dahlquist

Mark Sherwin

Songi Han, Committee Chair

September 2017

Vita for Alicia Smith Lund

Education

Ph.D., Department of Chemistry and Biochemistry, University of California Santa Barbara
Expected Graduation date: September 2017
Concentration: Physical Chemistry

B.S. Chemistry, Western Washington University, June 2011
Minors: Math, Physics

Research Experience

Graduate Student Researcher, July 2011-Present
University of California Santa Barbara
P.I.: Professor Songi Han
Project: Instrumentation development and applications of surface enhanced solid state dynamic nuclear polarization nuclear magnetic resonance

Undergraduate Researcher, June 2009-June 2011
Western Washington University
P.I.: Professor Elizabeth Raymond
Project: Study of atmospheric pollutant participation between oil-water interfaces through second harmonic generation spectroscopy

Publications

Lund, Alicia; Perea, Armin; Engelke, Frank; Han, Songi; *Optimization of Microwave Transmission through a Magic Angle Spinning Dynamic Nuclear Polarization Probe*. (paper in progress)

Lund, Alicia; Kaminker, Ilia; Han, Songi; *Reductions of Nuclear Depolarization under MAS of Mono-, Bi- and Tri-Nitroxide Radicals for Dynamic Nuclear Polarization*, (paper in progress)

Lund, Alicia; Hsieh, Ming-Feng; Siaw, Ting Ann; Han, Songi; *Direct ^{27}Al Dynamic Nuclear Polarization of Reactant Accessible ^{27}Al Catalytic Surface Sites*, Phys. Chem. Chem. Phys. (2015)

Siaw, Ting Ann; Leavesley, Alisa; **Lund, Alicia**; Kaminker, Ilia; Han, Songi; *A Versatile and Modular Quasi Optics-Based 200 GHz Dual Dynamic Nuclear Polarization and Electron Paramagnetic Resonance Instrument*, J. Mag. Reson. (2016)

Siaw, Ting-Ann; Fehr, Matthias; **Lund, Alicia**; Latimer, Allegra; Walker, Shamon; Edwards, Devin; Han, Songi; *Role of Electron Spin Dynamics on Solid-State Dynamic Nuclear Polarization Performance*, Phys. Chem. Chem. Phys. (2014)

Conference Presentations

Oral Presentations

Direct Dynamic Nuclear Polarization of Surface-Accessible Aluminum in Mesoporous Material, presented at FGMR Discussion Meeting on Advanced Magnetic Resonance, Methods and Applications (2014)

Poster Presentations

Method and Hardware Development for MAS DNP at 25 K, presented at the Experimental NMR Conference (2017)

¹H Magic-Angle Spinning Depolarization at Temperatures <100 K with Mono-, Bi-, and Tri- Nitroxide Radicals, presented at the Experimental NMR Conference (2016)

Direct DNP of ²⁷Al NMR as a Surface Probing Tool at 7 T and Liquid Helium Temperatures, presented at the Rocky Mountain Conference on Magnetic Resonance (2014)

Direct (non-CP) DNP of ²⁷Al NMR as a Surface Probing Tool at 7 T, presented at the Experimental NMR Conference (2014)

Method Development of Solid State Dynamic Nuclear Polarization 20 K, presented at the Experimental NMR Conference (2013)

Awards

University of California Santa Barbara Central Fellowship Award (2016)

Aachen-California Network of Academic Exchange Award (2014)

Experimental NMR Conference Student Travel Grant (2014)

Rocky Mountain Conference on Magnetic Resonance Student Travel Award (2014)

Teaching Experience

Teaching Assistant, October 2011-April 2014

University of California Santa Barbara

Courses: General Chemistry Lab, Analytical Chemistry Lab, Physical Chemistry Lab, Biophysical Chemistry Lecture

ABSTRACT

Instrument and Method development for High Field Dynamic Nuclear Polarization with Magic Angle Spinning Spectroscopy at 25 K

by

Alicia Smith Lund

The aim of the work presented here has been to optimize the sensitivity of nuclear magnetic resonance (NMR) through the use of the technique of dynamic nuclear polarization (DNP) and magic angle spinning (MAS). DNP is a technique where the polarization from free electron “DNP agent” can be transferred to hyperfine coupled nuclei through microwave irradiation of the sample. The greatest nuclear polarizations are to be expected when the starting thermal electron and nuclear polarization is maximized by operating MAS at a helium cryogenic temperatures. Through a collaboration with Revolution NMR LLC and Bruker Biospin we have development a Cryo DNP-MAS probe operation at a temperature of 25 K and spin rates of 8 kHz. We have measured the microwave beam transmission through each component of the Cryo DNP-MAS probe and optimized the NMR coil and rotor material to maximize the microwave transmission to the sample. We have found that changing the geometry of the radio frequency NMR coil allowing for greater transmission of microwaves doubled the resulting nuclear signal enhancement.

Much of the current development in DNP has focused on tethered nitroxide radicals as the DNP agents, but the design of potent radicals for DNP, in particular under magic angle spinning (MAS) conditions, is still debated and relies on empirical trial and error as the contributing factors for MAS DNP enhancement are not entirely understood. Significant instrumental effort is needed to measure the electron paramagnetic resonance EPR parameters at magnetic fields of 7 T or greater. This work presents the development of an EPR spectrometer at 7 T in order to measure the electron spin dynamics contribution factors to DNP. We have found that the nuclear depolarization induced by MAS is determined by the spin-lattice relaxation time of the nitroxide DNP agent, and once this depolarization is accounted for different tethered nitroxide radical designs have the same DNP signal enhancement. Finally the signal enhancement capabilities of the Han labs home built DNP system is demonstrated through direct enhancement of aluminum spins on the surface of a mesoporous material targeting catalytically active aluminum spins on the surface. When the nitroxide radical is tailored to have a favorable electrostatic interaction with the surface species, the aluminum NMR signal enhancement can be up to 10 fold.

TABLE OF CONTENTS

I. Introduction	1
A. Motivation and Objectives.....	1
B. Overview of Nitroxide Radicals EPR	4
C. DNP Mechanism Under Static and MAS	7
II. Instrumentation Development of a 7 T Pulsed EPR Spectrometer	18
A. Introduction.....	18
B. EPR Instrument Overview	24
C. Demonstration of EPR capabilities on Model Systems	33
D. Conclusion	39
III. Effect of Nitroxide Radical Electron Spin Dynamics on Nuclear Depolarization under MAS.....	41
A. Introduction.....	41
B. Experimental	44
C. Results	46
D. Conclusion	61
IV. Optimizing Microwave Transmission Through a Custom 20 K DNP MAS Probe	63
A. Introduction.....	63
B. Details of the Revolution NMR Cryo MAS probe	64
C. Simulation and Experimental Methods.....	67
D. Results and Discussion	72
E. Conclusion.....	78

V. Resolving TEMPO and ^{27}Al interaction with Direct DNP and EPR in Al-SBA-1579	
A. Introduction.....	79
B. Experimental Methods	82
C. Results and Discussion.....	85
D. Conclusion	92
VI. Conclusion and Outlook	93
References.....	97
Appendix.....	104
The solid effect	104
Cryostat:.....	105
Probe insert:	106
MW bridge support structure:.....	108
QO MW bridge:	109

I. Introduction

A. Motivation and Objectives

Electrons and nuclei contain an intrinsic unit of angular momentum called “spin” such that when placed in a large static magnetic field, the spin aligns either parallel or antiparallel with the static magnetic field vector and begins to process around the magnetic field with a characteristic frequency that can be used as a fingerprint for specific types of nuclei or electrons. This idea became the basis for electron paramagnetic resonance spectroscopy (EPR) and nuclear magnetic resonance spectroscopy (NMR), first observed in the years 1944^[1,2] and 1946^[3,4] respectively. NMR in particular has become an extremely powerful spectroscopic characterization technique that is commonly used across all fields of science. Applications of NMR include magnetic resonance imaging (MRI),^[5] structural determinations of organic compounds in solution, and molecular level structural characterization of inorganic and biological solids (solid state NMR). Solid state NMR combined with magic angle spinning (MAS) has been shown to be a powerful tool for elucidating molecular structural information in a variety of biological compounds and material systems. Researchers, especially in materials science, have found NMR to be important for atomic level structural information in heterogeneous amorphous catalysts.^[6] However, the inherently low signal sensitivity of NMR makes it exceptionally difficult to selectively examine surface or sub-surface species. The signal sensitivity for a two energy level spin $\frac{1}{2}$ system is related to the population of the two energy levels, known as the Boltzmann spin polarization.

The Boltzmann polarization of 100% natural abundance ^1H nuclear spins is 10^{-3} % at 300 K and 7 T. This situation is exacerbated when the NMR active isotope is of low natural

abundance such as ^{13}C (1.1 % abundance) or ^{15}N (0.4 % abundance). To combat this sensitivity issue one can cool the sample temperature, increasing the Boltzmann polarization, but even at 20 K the polarization of ^1H spins is only $10^{-1}\%$. In addition this method of cooling the sample alone will still not give surface selectivity desired for structure determination in catalytic material without further enhancing surface spins. Recently there has been a renaissance in the development of dynamic nuclear polarization (DNP), creating highly localized NMR signal enhancement by using microwave irradiation to transfer polarization from highly polarized unpaired electron spins ($\sim 8\%$ electron polarization at 90 K) to low polarized nuclear spins ($\sim 0.008\%$ ^1H polarization at 90 K) that are coupled to an electron spin probe. MAS DNP has been shown to be a powerful tool for elucidating molecular structural information in a variety of biological compounds^[7,8] and surface structures in various material systems^[9-12], with rapid development towards surface, materials^[10,11,13-22] and biosolid^[8,23-33] characterization methods. The potential for DNP to transform NMR into a staple materials and biosolids characterization tool stems from the ability of this technique to generate an enhancement of NMR signal by $O(10^1-10^3)$ fold via polarization transfer from the electron spin of DNP-suitable radicals (also termed DNP agents) to the target nuclear spins. This signal gain, combined with a thermal polarization gain of $O(10^1-10^2)$ fold from cryogenic cooling to liquid nitrogen or helium temperatures and high magnetic fields, yields a total gain in nuclear spin polarization of $O(10^2-10^5)$ including the extreme ends.^[34,35] The signal enhancement from DNP-MAS has led to drastic time savings, reducing experiment times from days to hours, allowing NMR experiments that were not previously feasible such as natural abundance heteronuclear correlation measurements.^[13,36] Because of the broad potential of DNP to enhance the capabilities of

solid-state MAS NMR well beyond its current state of the art, much work has gone into designing the ideal radical-based DNP agents for maximum signal enhancement at high magnetic fields.^[37] Much of the current development has focused on tethered nitroxide radicals such as the bi-radicals totapol,^[38] amupol^[39] and tekpol,^[40] while there are also studies of tri-radicals like dotopa,^[41] radical mixtures,^[42,43] and more recently mixed bi-radical species.^[44] But the design of potent radicals for DNP, in particular under MAS conditions, is still debated and relies on empirical trial and error as the contributing factors for MAS DNP enhancement are not entirely understood. Through theoretical simulation, the spin dynamics of the free radical electron spin have been shown to be a dominating factor in determining the efficiency the MAS DNP process,^[45,46] yet significant instrumental effort is needed to measure these parameters at magnetic fields of 7 T or greater. Through the development of a pulsed EPR spectrometer and a cryo MAS DNP probe operational at 25 K and 7 T, we seek to understand the relationship between electron spin dynamics and the polarization transfer process from electrons to surrounding nuclei in DNP in order to aid in the design of polarizing radicals for high magnetic fields, towards the specific application of surface enhanced DNP of mesoporous catalytic materials.

The following sections of chapter one will familiarize the reader with high field EPR of nitroxide radicals used for DNP and lend insight on the difficulties of measuring electron spin parameters such as spin-lattice relaxation time and spectral diffusion which require custom instrumentation not commercially available. Chapter one will also provide a current theoretical understanding of the mechanism of MAS DNP, demonstrating why the electron spin parameters are so important to the polarization process. Chapter two will describe in detail the instrument design of the EPR spectrometer developed in Songi Han's lab at the

University of California, Santa Barbara, and demonstrate the unique electron-electron double resonance measurements capabilities with this spectrometer design. Chapter three will demonstrate how, using this EPR spectrometer, the electron spin dynamics were measured and directly correlated with cryo MAS DNP measurements in order to determine absolute DNP enhancement and electron spin effects on nuclear depolarization. Chapter four will detail applications of our instruments towards surface enhanced NMR measurements of aluminosilicates. Finally, Chapter five will describe ongoing efforts to optimize the microwave transmission through the cryo MAS probe in collaboration with Revolution NMR LLC, and give a preview of current efforts toward EPR detection under MAS with modifications to the Revolution NMR probe head.

B. Overview of Nitroxide Radicals EPR

The nitroxide radical is the most ubiquitous radical used in both DNP/NMR and EPR measurements. This is largely due to the stability of the free radical in organic and aqueous solvents, the ability to use nitroxides in site-directed spin labeling of a protein complex.^[47] The 2,2,6,6-Tetramethylpiperidin-1-yl)oxyl or (2,2,6,6-tetramethylpiperidin-1-yl)oxidanyl (TEMPO) nitroxide radical pictured in Figure 1(a), where R=H, has a free electron spin that is delocalized between the nitrogen and oxygen atoms. The free electron spin itself is an $S=1/2$ spin, which when placed in a magnetic field is governed by the Zeeman interaction given in equation (1),

$$\text{Equation (1).} \quad H_z = \frac{\mu_B}{\hbar} \mathbf{g} S_z B_0$$

where μ_B is the Bohr magneton, \hbar is Planck's constant, S_z is the spin operator in the z -direction, B_0 is the static magnetic field, and (\mathbf{g}) is a tensor that is dependent on the electron

orbital angle to the magnetic field. The g tensor orientation dependence is analogous to chemical shift anisotropy (CSA) in solid state NMR. For the nitroxide radical the g -factor is anisotropic, i.e. dependent on the orientation of the nitroxide radical. The g -factor is largest along the axis of the N-O bond g_x (2.0090), and smallest along the axis the p-orbital of the nitrogen g_z (2.0025), with g_y at an intermediate value of 2.0060. As shown in Figure 1(b), at 7 T the g -anisotropy spans ~ 1 GHz. Due to the delocalized nature of the free electron in the nitroxide, the nitroxide spectrum shows a triplet lineshape and the ^{14}N $I=1$ spin causes a large hyperfine splitting on top the Zeeman splitting of the electron spin. Figure 1(a) shows the derivative of the EPR lineshape in order to highlight the hyperfine splitting along the x , y , and z direction of the molecular axis of the nitroxide moiety. The hyperfine interaction is largest along the p-orbital of the ^{14}N nuclei (z -direction) with $A_{zz} \sim 3.4$ mT, and smallest perpendicular to the p-orbital in the x and y direction with A_{xx} and $A_{yy} \sim 0.6$ mT.

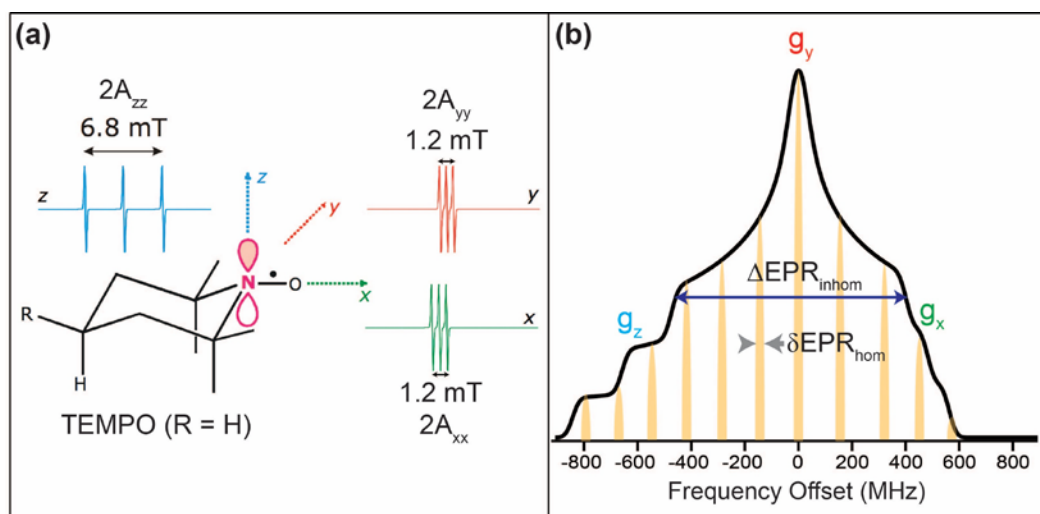


Figure 1. (a) The TEMPO radical cw derivative lineshape showing g and A -anisotropy in the EPR spectrum. (b) Simulated adsorption lineshape at 7 T orange bars show different homogeneously broadened spin packets across the inhomogeneously nitroxide line. Nitroxide lineshape simulations performed with EasySpin simulations package for Matlab.

The nitroxide lineshape shown in Figure 1(b) at 7 T is composed of spin packets, an ensemble of electron spins which experience the same time-averaged local magnetic fields. These spin packets are shown in orange in Figure 1(b). The linewidths (δEPR_{hom}) of these spin packets are homogeneously broadened corresponding to the transverse relaxation time (T_2) of the spin packets. The superposition of these homogeneously broadened spin packets with distinct Larmor frequencies make up the inhomogeneously broadened EPR lineshape with linewidth ($\Delta EPR_{\text{inhom}}$). The main source of inhomogeneous broadening in the nitroxide EPR spectrum at high magnetic field is the g tensor anisotropy.^[48] The relaxation properties of these spin packets and how one electron spin packet interacts with other spin packets across the EPR spectrum are important parameters in determining the DNP enhancement efficiency as will be discussed in the following section. In order to obtain an accurate picture of how these electron spin parameters effect the DNP process, high field EPR measurements are necessary.

Commercial EPR instruments are available from 0.35 T to 3.5 T for pulsed EPR using traveling wave tube (TWT) amplifiers to reach ~1 kW of microwave power. However, the work presented in this thesis was performed at 7 T where the nitroxide spin is resonant at ~197 GHz with a microwave wavelength of 1.4 mm, and TWT amplifiers have yet to be built with dimensions this small. Gyrotrons provide up to 100s of watts of microwave power at frequencies of 200 GHz but are not suitable for creating pulses in the 100 ns range required for pulsed EPR.^[49,50] The recent development of gyrotron amplifiers have shown promise in overcoming this challenge but are not widely available.^[51] Thus far the most

available option for pulsed microwave sources at our desired frequency of ~ 200 GHz is using a 12 GHz frequency synthesizer, which is then amplified using a set of Schottky diode frequency multipliers in order to reach the desired output frequency, these sources are available from Virginia Diode Inc. (VDI) with 140 mW of power. However, the VDI low power source are not able to excite the full nitroxide spectrum, with an excitation bandwidth of ~ 0.4 MHz which is much less than the nitroxide spectral width extending ~ 2 GHz at 7 T. This type of solid state diode source has the advantage of being easily implemented into a pulsed EPR circuit and switching between multiple synthesizers for electron-electron double resonance (ELDOR) experiments which are of great interest to the DNP community.^[52–55]

C. DNP Mechanism Under Static and MAS

The concept of transferring Boltzmann spin polarization from unpaired electrons to surrounding nuclei through microwave irradiation of the electron spin was first proposed in 1953 by Overhauser.^[56] The result could yield a theoretical signal enhancement (ϵ) corresponding to the ratio of the gyromagnetic ratio (γ) between the electron and nuclei which is equal ~ 660 for ^1H and ~ 1200 for ^{13}C nuclei. The Overhauser DNP effect requires mobile electrons, either in solution state or conduction band electrons,^[57] in order to allow for cross relaxation pathways between electrons and nuclei. Recent studies have also shown the Overhauser effect is possible in insulating solids when rotated at the magic angle.^[58] Since Overhauser first introduced the concept of DNP there have been a handful of theoretical and empirical descriptions of other mechanisms for transferring the polarization between the electron and nuclear spins. The following section will give a brief introduction

to the polarization mechanisms which are most relevant for solid state MAS DNP experiments at temperatures of 100 K and below.

When there is a low concentration of electron spins, less than 2 mM, the DNP process is governed by isolated dipolar coupled electron nuclear spin pairs.^[59] This mechanism is called the well resolved solid effect (S.E.) and was first described by Abragam and Proctor in 1958.^[60] This mechanism relies on the mixing of nuclear states due to the hyperfine coupling of the electron and nuclei. Microwave irradiation of the classically forbidden transition will cause excitation of the double quantum and zero quantum transitions which will lead to enhancement of positive and negative NMR signals respectively.^[61] The mixing of states depends inversely on the separation of the energy levels in the spin system, $\frac{1}{B_0}$,

therefore the probability of the forbidden transition is proportional to $\frac{1}{B_0^2}$, and the S.E. efficiency decreases with increasing magnetic field.^[62] More on the quantum mechanical description of the S.E. is detailed in Appendix A.

In contrast, at high electron concentration, >50 mM, where homogenous broadening of the EPR line is greater than the nuclear Larmor frequency a multi-spin effect has been proposed called thermal mixing (TM). In this regime a spin temperature approach can be used as a theoretical basis for the polarization process. A spin temperature is used to describe the Boltzmann polarization for the electron Zeeman, electron dipolar, and nuclear Zeeman spin bath. Microwave irradiation results in the cooling of the electron Zeeman bath which quickly equilibrates through the electron dipolar network to a common spin temperature.^[25] This creates a spin temperature gradient between the electron dipolar network and the nuclear Zeeman reservoir, which results in a spin temperature exchange that

generates nuclear polarization. Hovav et al.^[63] demonstrated the spin temperature characteristics of TM using a spin density matrix formulation without a priori assumption of the spin temperature model, validating the usage of a spin temperature model to describe the TM process under certain sample conditions. In their simulations, they found that TM requirements are difficult to fulfill for typically employed nitroxides that possess EPR lines that have strong inhomogeneous broadening.

The dominant mechanism of nitroxide radicals at high magnetic fields and radical concentrations ~10-40 mM, where the majority of MAS DNP experiments are performed, is the cross effect mechanism (CE). This mechanism was first reported by Hwang and Hill in 1967.^[64,65] The CE mechanism involves two dipolar coupled electron spins S_1 and S_2 that have frequencies ω_{e1} and ω_{e2} respectively, and S_2 is hyperfine coupled to a nuclear spin I with Larmor frequency ω_n . The Hamiltonian for such a three spin system is summarized in Equation (2), with the following contributions to the Hamiltonian: the Zeeman interaction terms for the two electrons and nuclei H_{Ze1} , H_{Ze2} , and H_{Zn} , the dipolar interaction between H_{e1e2} , the hyperfine interaction between the electron and nuclei H_{e2n} , and the applied microwave field H_{MW} with frequency f_{MW} and amplitude ω_{MW} .

$$\text{Equation (2)} \quad H = H_{Ze1} + H_{Ze2} + H_{Zn} + H_{e1e2} + H_{e2n} + H_{MW}$$

$$H_{Ze1} = \omega_{e1} S_{1z}$$

$$H_{Ze2} = \omega_{e2} S_{2z}$$

$$H_{Zn} = \omega_n I_z$$

$$H_{e1e2} = d(2S_{1z}S_{2z} - S_{1x}S_{2x} - S_{1y}S_{2y})$$

$$H_{e2n} = h_{zz} 2I_z S_{2z} + h_{xz} 2I_x S_{2z} + h_{yz} 2I_y S_{2z}$$

$$H_{MW} = \omega_{MW} [(S_{1x} + S_{2x}) \cos(f_{MW} t) + (S_{1y} + S_{2y}) \sin(f_{MW} t)]$$

This three spin Hamiltonian yields an eight energy state system as depicted in Figure 2, where $\omega_{e1} - \omega_{2e} = \omega_n$ creating a degeneracy in states 4 and 5, or 3 and 6. Microwave irradiation at the allowed EPR transition of ω_{e1} causes an energy conserving spin flip of ω_{2e} , and will simultaneously cause a flip of the nuclear spin. Irradiating at ω_{2e} will cause a buildup of nuclear polarization in state 5 which will give a positive NMR enhancement, while irradiation at ω_{e1} will yield a negative NMR signal enhancement. In order for the CE condition to be fulfilled ($\omega_{e1} - \omega_{2e} = \omega_n$) the inhomogeneous EPR (ΔEPR_{inhom}) linewidth must be larger than ω_n and the homogenous linewidth smaller than ω_n . The EPR linewidth scales with $1/B_0$ and therefore the degeneracy condition becomes more difficult to fulfill, and the efficacy of this mechanism decreases with increasing magnetic field. Much of the work to optimize sample conditions for DNP MAS has been done empirically. The radical of choice in these experiments is usually a nitroxide radical derivative, with $S=1/2$. The free

electron of the nitroxide moiety resides partially in a p orbital of the nitrogen atom, leading to a large inhomogeneously broadened EPR line, which scales with magnetic field, as shown in Figure 3. This inhomogeneously broadened EPR line means nitroxides are a good candidate for fulfilling the cross effect mechanism, and have been shown to be an effective radical to achieve DNP enhancement in a variety of biological and material systems.^[13,66,67] The design of bi-nitroxide radicals, two nitroxide species tethered by a covalent linker, has increased the effectiveness of the cross effect mechanism under MAS. Much work has been done to design the ideal bi-radical for DNP, and again this has largely been done empirically.^[38,41,54] One trend that has become apparent through empirical observations is that there is a clear connection between electron spin dynamics, such as spin-lattice relaxation and electron spectral diffusion, and DNP enhancement. Therefore, the pursuit of the perfect radical would greatly benefit from the ability to measure these electron spin parameters at high magnetic fields, i.e 7 T or greater.

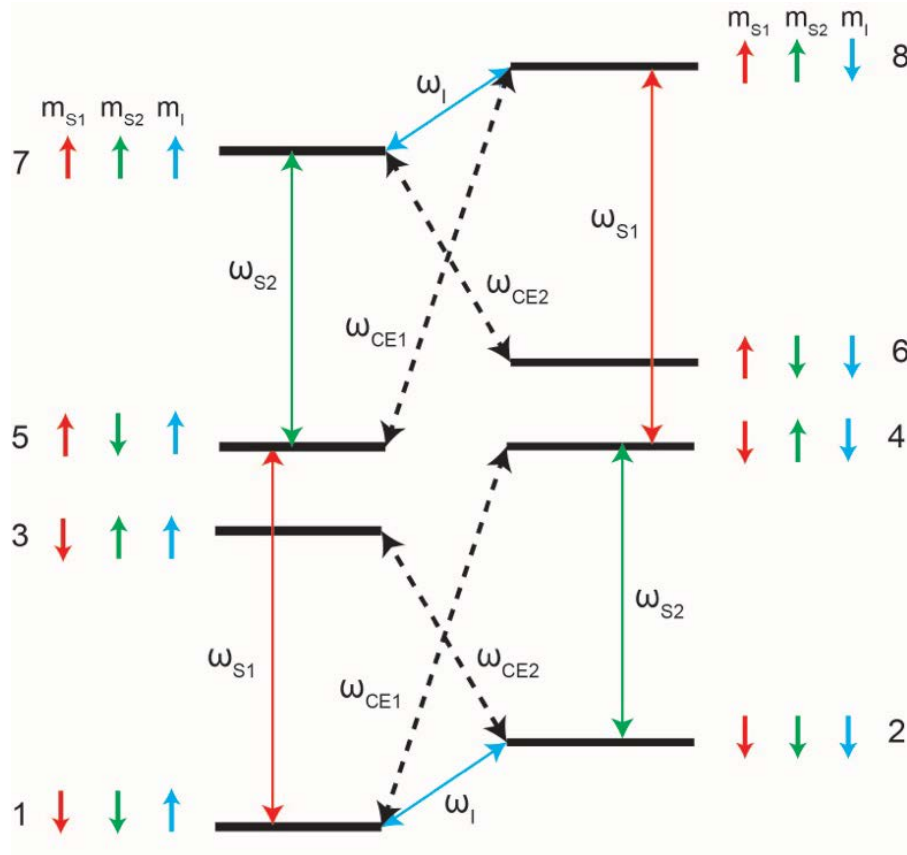


Figure 2. Energy level diagram for three spin CE Hamiltonian in Equation 2. When the frequency difference of the two electron spins is equal nuclear Larmor frequency energy levels 5 and 4 or 3 and 6 become degenerate and irradiation with microwaves at ω_{CE1} will drive a build up in nuclear polarization.

However, these kinds of instruments are not commonly available, a summary of the few

high field pulsed EPR spectrometers are discussed in the introduction of chapter 2. To understand why the CE have become the most ubiquitous mechanism for MAS DNP one needs to understand how the energy in Figure 2 are affected by MAS. Under static conditions only a small portion of the nitroxide radicals in the sample will have the correct frequency difference to fulfill the CE condition, yet the CE the most commonly used mechanism at high magnetic fields for DNP enhancement under MAS. When a radical with a large g-anisotropy like a nitroxide radical with the energy diagram in Figure 2 is rotated about the magic angle, the energy states become dependent on the rotor period as shown in Figure 3. Figure 3 shows an example of a spin system where the CE condition is met under the static case. Spinning the sample now makes the C.E. condition time dependent and there are multiple points over the rotor period where the polarization transfer from the electron to nuclei will happen. Figure 4 takes the initial static condition where the CE condition is not met ($\omega_{e1} - \omega_{2e} \neq \omega_n$), in this case spinning the sample causes the energy levels to cross during the rotor period and participate in the electron polarization transfer to the nuclei. This means the effect of spinning the sample greatly increases the cross effect mechanism. The theory of the cross effect mechanism under MAS has yet to be fully explored with only a handful of articles detailing a quantum mechanical description of the three spin process under MAS by Tycko, Thurber and Vega.^[45,46,68,69]

If there is a large polarization difference between e_1 and e_2 this will result in a net gain of nuclear polarization at the crossing points in Figure 3 (yellow dots). Irradiation with microwaves at ω_{e1} creates the polarization difference that drives the nuclear polarization process. The C.E. condition and polarization transfer itself does not require microwave

irradiation when the sample is under MAS, i.e. the nuclear polarization can be altered without microwaves but just by spinning the sample. If the difference in polarization between the two electrons is small or almost zero, spinning the sample about the magic angle will result in a reduction of the nuclear polarization to a value less than the Boltzmann polarization. This effect is known as nuclear depolarization and has been observed with various bi- and tri- nitroxide radicals at 20 K and 90 K.^[69,70] This effect has been shown to inflate the enhancement value by a factor of 20 % at 90 K and 60 % at 20 K when enhancement is measured as the ratio of the NMR signal with and without microwaves. The extent of nuclear depolarization with MAS depends on how the electron spins equalize polarization, i.e. the extent of the electron flip-flop crossings shown by the blue dots in Figure 3. This is dependent on the electron spin dynamics of the radical moiety, i.e. T_{1e} , and spectral diffusion. Recently much work has been done to design mixed bi-radicals with a nitroxide and narrow line radicals such a trityl or BDPA to eliminate this depolarization effect,^[44] but the underlying electron spin properties of these radicals are still not understood. With the development of pulsed EPR instrumentation in Songi Han's lab, we have measured the T_{1e} and spectral diffusion of various mono-, bi-, and tri- nitroxide radicals and have demonstrated how these parameters influence the efficiency of the CE mechanism and nuclear depolarization effect.

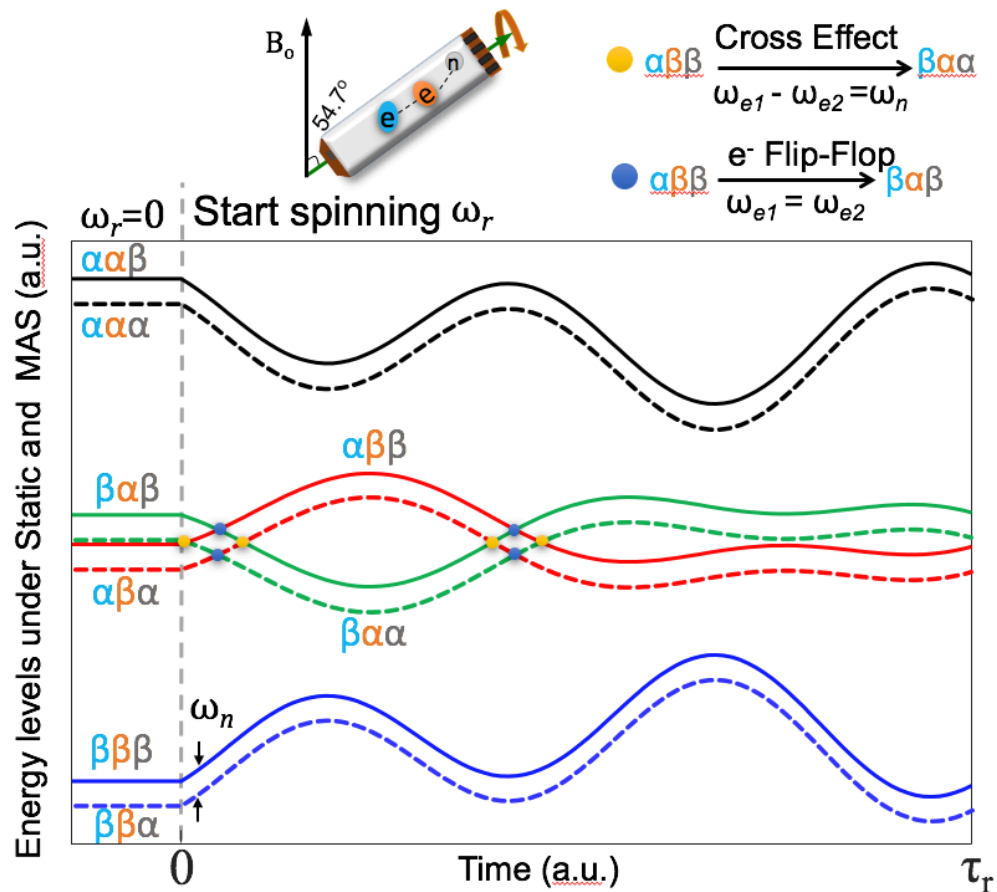


Figure 3. Energy level diagram of three spin cross effect system under static and MAS conditions. The CE condition becomes time dependent under MAS (yellow dots). The electron frequency crossing (blue dots) also becomes time dependent, making it possible for exchange of electron polarization over the course of the rotor period. This simulation was performed with the NMR simulation software SpinEvolution.

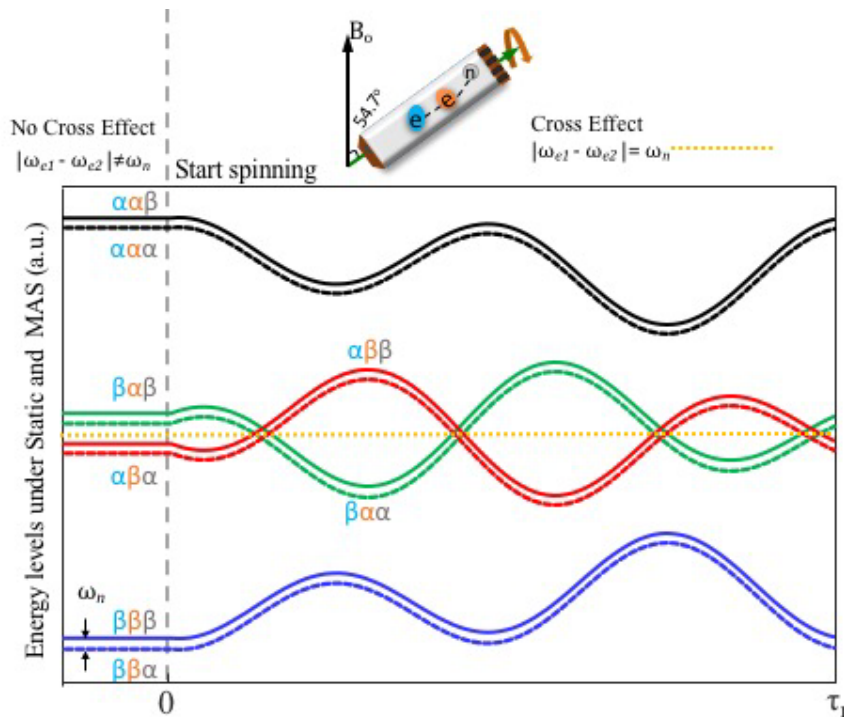


Figure 4. Initially without MAS the CE condition is not fulfilled, shown in the yellow dashed line. Spinning about the magic makes the CE condition fulfilled at multiple time points over the rotor period. This simulation was performed with the NMR simulation software SpinEvolution.

The gaps in instrumentation and knowledge presented above inspired the work presented in this thesis. The need to measure electron spin parameters under similar DNP conditions (i.e cryo temperatures and high field) has inspired the building of a dual DNP/EPR spectrometer for static conditions and the development of MAS for EPR measurements. Our MAS instrumentation has allowed for quantification of this depolarization effect and its correlation to electron spin parameters such as T_{1e} and electron spectral diffusion. The low power VDI source employed in this DNP/EPR spectrometer is simple to implement pulsed microwave manipulation but the low power output of this source comes with a great cost to the DNP enhancement. In collaboration with Revolution NMR LLC we have optimized

various aspects of the NMR probe for optimal microwave transmission to the sample inside to MAS rotor. Finally we show how static EPR and DNP measurements can be used to track how various nitroxide radical derivatives imbibe themselves in the pores of alumino-silicate materials, opening the possibility of selective DNP enhancement.

II. Instrumentation Development of a 7 T Pulsed EPR Spectrometer

A. Introduction

Solid-state (ss)-DNP is rapidly becoming a powerful surface structural characterization tool, however much is still unknown about the principle operation of ssDNP, where the basic theoretical models for ssDNP even under static, and undoubtedly under magic angle spinning (MAS) conditions require further developments. In recent years, several articles detail improvements to the MAS CE formalism as discussed in chapter one. From the theory level, crossing in the cross effect under MAS it is clear that electron spin parameters are important for determining the polarization transfer. These include electron T_{1e} and T_{2e} , and at the same field and temperatures of the DNP operation, electron spectral diffusion rate and EPR saturation profile. The need to further develop the understanding of ssDNP mechanisms and to generate practically useful theoretical models is illuminated by highly interesting observations reported on in the literature that are contrary to conventional wisdom. The need to better understand ssDNP processes, coupled with the need to explore a wide EPR parameter space for performance optimization, calls for versatile pulsed EPR hardware. The required hardware performance is reflected in the type of experiments that yielded MW frequency/field modulation, MW power stepping, EPR detection (particularly ELDOR), MW frequency sweeps, EPR relaxation measurements, all done at high magnetic fields where the electron spin resonance frequency for nitroxides is around 200 GHz. The combination of these hardware capabilities is not offered with any commercial instrument platform. Instead, select capabilities are available through different ssDNP setups, as listed below. The following is by no means a comprehensive list of DNP instrumentation

developed but highlights developments of dual DNP/EPR instrumentation and compares the DNP performance with commercial DNP systems.

1) **Gyrotron-powered MAS DNP systems:** High resolution MAS-gyrotron systems operating at >5 T and 90-150 K have been developed by Griffin et al. and commercialized by Bruker Biospin. Gyrotron systems offer high microwave power output between 5-35 W, allowing for DNP operation at higher temperatures of 90-150 K,^[49,50,71–77] while recent developments by Idehara et al. and Gaël de Paëpe et al. also enable liquid helium operation around 30 K with gyrotron-powered DNP systems.^[78,79] Notably, the Matsuki, Idehara and Fujiwara et al.^[80] system relies on a dual gyrotron source at 460 GHz and 459-461 GHz for MAS DNP operation at 16.4 T and liquid helium temperatures. Additionally, Pike et. al.^[28] have developed a system that uses the fundamental (187 GHz) and second harmonic (395 GHz) of a gyrotron source for DNP signal detection at 6.7 and 14 T. In general, a gyrotron source can offer a frequency bandwidth of up to 3 GHz, but the MW power is not constant over this frequency range. This means that DNP spectra can only be acquired reliably using a field sweep, instead of a frequency sweep. At the moment, EPR detection is not feasible with these systems due to amplitude fluctuations of the gyrotron source output. The gyrotron system has been successfully applied for enhanced structural resolution of biological systems^[8,23,25,26,28–33] and the characterization of materials surfaces.^[22,36,81] Significant progress in DNP-enhanced MAS NMR can be attributed to the design and development of novel DNP polarizing agent design, such as TOTAPOL, AMUPOL, bTbk, etc. with superior performance compared to mono-nitroxide radicals under typical MAS DNP operating conditions.^[37,82–84]

2) **Nottingham Kockenberger lab ssDNP/EPR systems:** One of the Kockenberger dissolution DNP systems was built around a two-center magnet for polarization at 3.35 T and NMR detection at 9.4 T with a non-zero field transition between the two and included a QO bridge for cw-EPR detection at 94 GHz. This system was designed to minimize polarization loss when transferring the sample from the polarizing field (3.35 T) to the detection field (9.4 T).^[85] Another unique spectrometer in the Kockenberger lab is a 3.35 T dissolution DNP spectrometer with longitudinal EPR detection capabilities.^[53] This spectrometer employs a 200 mW diode source with a swappable range of 650 MHz, which allows for the acquisition of frequency or amplitude modulated cw-EPR spectra as well as for ELDOR experiments. The Kockenberger group was the first group to measure the TEMPO ELDOR spectrum under DNP conditions for the purpose of directly measuring the extent to which the EPR line of TEMPO is affected upon prolonged microwave irradiation.

3) **Massachusetts Institute of Technology (MIT) Griffin lab ssDNP/EPR system:** A dual pulsed-EPR/DNP spectrometer operating at 5 T (140 GHz electron / 212 MHz ^1H) is described by Smith et. al.^[86] This instrument was designed to perform pulsed EPR and DNP at temperatures of less than 100 K under static (non-MAS) conditions. This system was built in order to study the mechanism of the DNP process, where knowledge of the spin relaxation times of the electron spins in the sample are important for understanding the DNP enhancement process. This spectrometer also has the capability to perform ELDOR and electron nuclear double resonance (ENDOR) experiments. With these capabilities one can directly measure the saturation profile of an EPR spectrum upon microwave irradiation of the sample under DNP conditions.

4) **Weizmann Institute Vega and Goldfarb lab ssDNP/EPR system:** A dual EPR/DNP spectrometer operating at 3.34 T (95 GHz electron / 144 MHz ^1H) was built at the Weizmann Institute of Science by a joint effort of the groups of Daniella Goldfarb and Shimon Vega. This instrument was designed to concurrently perform EPR and DNP experiments at low temperature (< 100 K) under static (non-MAS) conditions and at 3.34 T fields.^[87] The EPR MW bridge of this DNP system was constructed based on a design previously refined by the Goldfarb group.^[88] The Vega and Goldfarb groups have contributed significantly to the quantum mechanical understanding^[52,61,63,89–92] of DNP processes through ELDOR^[52] and DNP data^[59,93,94] acquired using this spectrometer.

5) **NIH Tycko lab ssDNP system:** A MAS-DNP system operating at 9.4 T and down to 25 K temperatures, initially utilizing a low power diode MW source,^[95] and recently upgraded with a higher power extended interaction oscillator (EIO) MW source,^[95] was developed by Tycko, Thurber, and co-workers at the National Institute of Health (NIH). This MAS system is able to operate at liquid helium temperatures down to 25 K by using a novel MAS design consisting of an elongated MAS rotor where the ends of the rotor are spun with cold nitrogen gas and the center of the rotor cooled with liquid helium.^[96] Tycko and co-workers have been performing ssDNP-enhanced NMR studies of frozen samples of peptides^[41,95] and protein fibrils of amyloid beta.^[24] Tycko and co-workers have also contributed to the design of oligoradicals.^[41,95]

6) **UCSB Han lab ssDNP/EPR system:** A dual EPR/DNP spectrometer operating at 7 T and liquid helium temperatures powered by a tunable solid-state diode source (193-201 GHz) was developed by Han and co-workers at the University of California, Santa Barbara (UCSB).^[97] A quasi optical (QO) MW bridge is used to manipulate the quality, amplitude,

frequency and shape of the transmitted and reflected microwaves (e.g. for EPR detection). The QO DNP setup operates at room temperature down to 4 K on static samples, and at room temperature down to 25 K under MAS operation. Han et al. have observed the effect of oversaturation for a 40 mM nitroxide glass solution at 4 K,^[55] and also recently demonstrated targeted adsorption of DNP polarizing agents for characterizing catalyst active sites.^[15]

<i>System</i>	<i>Field</i>	<i>Temperature</i>	<i>MW source output</i>	<i>Current system capabilities</i>
<i>Gyrottron-powered DNP</i>	9.4 T 14 T 18.8 T	> 90 K	5-35 W	MAS acquisition, field swept DNP spectra
	9.4 T 14 T	30 K	5-35 W	MAS acquisition, field swept DNP spectra
<i>Nottingham Kockenberger lab dissolution DNP/EPR</i>	3.35 T	1-2 K	180 mW (diode)	Frequency swept DNP spectra, solution state DNP-enhanced spectroscopy, frequency swept cw-EPR
	3.35 T	1.5 K	200 mW (diode)	Pulsed and cw-EPR, frequency modulation, amplitude modulation, frequency swept DNP spectra, ELDOR, solution state DNP-enhanced spectroscopy
<i>MIT Griffin lab DNP/EPR</i>	5 T	1.4-290 K	120 mW (diode)	Pulsed and field swept echo-EPR, frequency swept DNP spectra, ELDOR, ENDOR, static NMR acquisition
<i>Weizmann Institute Vega and Goldfarb DNP/EPR</i>	3.34 T	2.5-290 K	1 W (diode)	Pulsed and cw-EPR, frequency modulation, frequency swept DNP spectra, ELDOR, static NMR acquisition
<i>NIH Tycko lab DNP/cw EPR</i>	9.4 T	20-290 K	0.8 W (EIO) 30 mW (diode)	MAS acquisition, frequency swept DNP (diode source only), field sweep, quasi optics manipulation of MW
<i>UCSB Han lab DNP/EPR</i>	7 T	4-290 K	140 mW (diode)	cw-EPR and pulsed, frequency swept DNP spectra, static and MAS NMR acquisition, quasi optics manipulation of MW

Table 1. Summary of the main types of modern ssDNP spectrometers, highlighting dual DNP/EPR spectrometers and their current capabilities.

From the summary of ssDNP systems provided above and summarized in Table 1, it can be seen that the hardware capabilities vary significantly between the different ssDNP systems available. Most ssDNP systems are focused on particular application targets, while the hardware improvements pursued are often centered on the saturation performance by MW irradiation, notably by higher power output or frequency modulation. However, systematic ssDNP studies focused on the spin physics of the electron-nuclear polarization transfer mechanism and quantification of DNP enhancement require additional hardware capabilities, such as ssDNP frequency sweeps and cw- and pulsed EPR experiments- such capabilities are currently available at 3.34 T,^[87] and some at 5 T.^[86] The UCSB ssDNP system in the Han lab operating at 7 T is complementary to existing hardware, and consists of a modular DNP hardware platform that allows for static and MAS NMR operation, and is designed to perform CW and pulsed EPR experiments. The versatility of the UCSB Han lab's ssDNP system arises from relying on a QO MW bridge, which is a common mode of operation for high field EPR setups^[98–104] as first demonstrated by Freed and co-workers,^[100] and provides the means for low loss transmission of MWs, which is critical when employing low power solid-state diode sources to drive DNP or EPR experiments. Furthermore, QO is the only approach in the sub-terahertz MW frequency regime to efficiently combine, isolate and re-direct MWs for EPR detection and experiments. The same QO bridge is compatible with alternative MW sources to a solid-state diode source, e.g. Klystron oscillators or high-power gyrotron sources. The NIH ssDNP setup by Tycko and coworkers that was originally powered by a diode source (Virginia Diodes Inc.) has already been modified to be powered by a Klystron amplifier (Communications & Power Industries LLC) that can output around 0.8 W of MW power.^[41] However, for the most versatile DNP and EPR operation, the use of

a solid-state source, despite its lower MW power output, is necessary to enable broadband (10 GHz frequency sweep width) MW tuning, precise MW amplitude and frequency control (10 Hz or better resolution), and the ability to apply amplitude (including pulsing ability and shaped waveforms) and frequency modulation of the transmitted microwaves. The UCSB system is built to maximize the versatile operation to enable the measurement of a wide range of DNP mechanism-relevant EPR parameters.

This chapter will describe the construction of the UCSB EPR system by building upon an already existing 7 T Bruker superconducting magnet and spectrometer system. Finally, I will describe the acquisition of cw-EPR spectra using frequency swept, field-modulated detection in lieu of the conventional field swept (and field-modulated) EPR detection, by presenting proof-of-principle data of standard Mn^{2+} and BDPA samples acquired at room temperature. We also describe the QO bridge design for future pulsed EPR implementations and superheterodyne detection as well as a two microwave source setup for electron-electron double resonance (ELDOR) experiments. It is important to note that this type of operation, in addition to the EPR detection discussed earlier, is currently not possible with a gyrotron MW source.

B. EPR Instrument Overview

The current EPR system discussed in this section is a result of hardware additions and modifications to an existing magnet and spectrometer system,^[35,97] specifically a 300 MHz, 89 mm wide bore Bruker superconducting magnet and a Bruker Avance D300WB console with a 1 kW rf amplifier. In order to enable EPR detection the following additions were made to the existing NMR spectrometer system. Figure 5 shows an overall sketch of the DNP NMR/EPR spectrometer with the following components.

- (1) MW source
- (2) MW pulse forming unit
- (3) quasi-optical system
- (4) NMR/EPR probe
- (5) EPR detection system
- (6) centralized control software

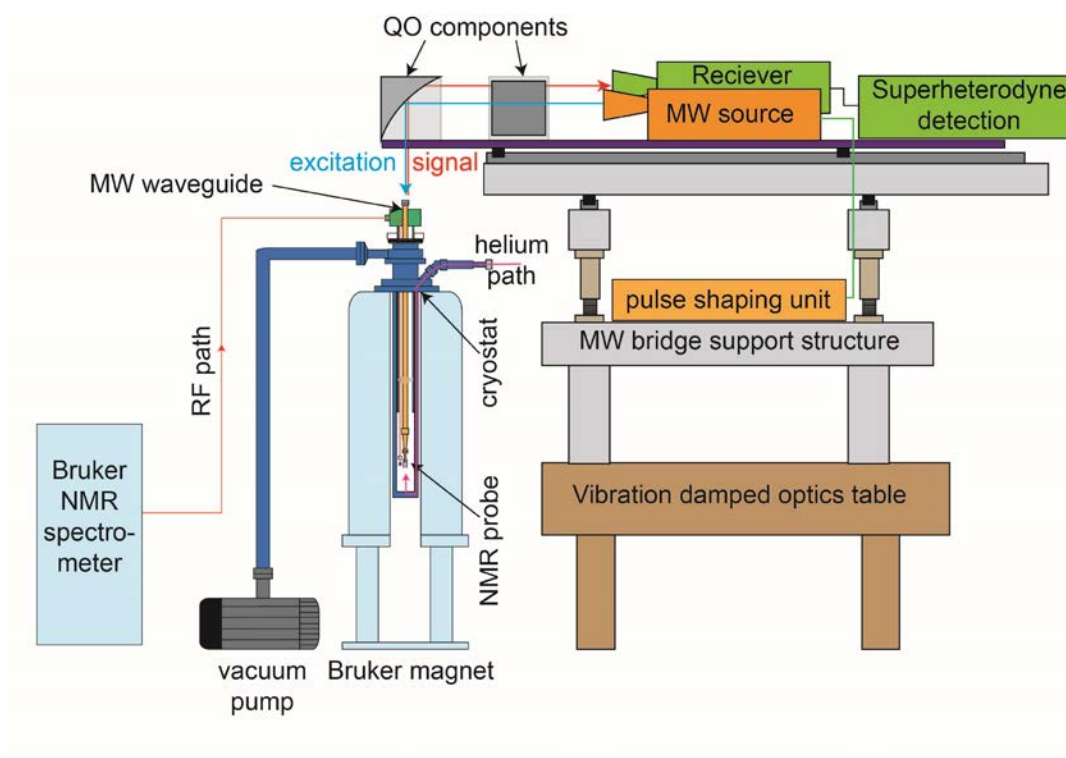


Figure 5. Sketch of overall configuration of the UCSB 200 GHz dual EPR/DNP system.

(1) Microwave Source

The 200 GHz MW source is a MW transmitter system by Virginia Diodes Inc. It consists of a 12 GHz Yttrium Iron Garnet (YIG)-based synthesizer (Micro Lambda Wireless Inc.) connected to a 16x amplifier-multiplier chain (AMC) that results in a final frequency of 193-201 GHz and a MW power output of up to 140 mW. The MW amplitude control is integrated into the system and is controlled using an analog input (0-5 V). The MW frequency of the 12 GHz YIG-synthesizer is controlled by a PC with 1 Hz resolution and <12 ms setting time using the Specman4EPR software (Femi Instruments, LLC). The use of a diode synthesizer at 12 GHz allows for manipulation of the microwaves using a PIN switch at 12 GHz before amplification to 200 GHz, while at 200 GHz the microwave manipulation must be done quasi-optically.

(2) Pulse Forming Unit

One key benefit of a solid state MW transmitter is the ability to incorporate various MW electronics between the MW source and the AMC to manipulate the MW field. In particular, pulsed EPR ELDOR experiments are of interest for monitoring the electron polarization profile across the inhomogeneously broadened EPR line. Figure 6 shows the schematics of the pulse forming unit implemented for our spectrometer that enables pulsed EPR and pulsed ELDOR capabilities is presented by integrating two synthesizers which can be independently controlled from double resonance experiments. Source 1 passes through a SP2T switch which creates the microwave pulse and sends the pulse to a phase shifter or bypass channel path. The voltage controlled phase shifter is adjusted to provide a 11.25°

phase shift at $F_S/16$ frequency which will result in a 180° phase shift after the $16\times$ frequency multiplication at the F_S frequency, allowing for a two-step phase cycling process to be implemented. A pair of switches is used to direct either source 1 or source 2 to the AMC, the output of which is directed through a transmitter horn to the quasi-optical circuit.

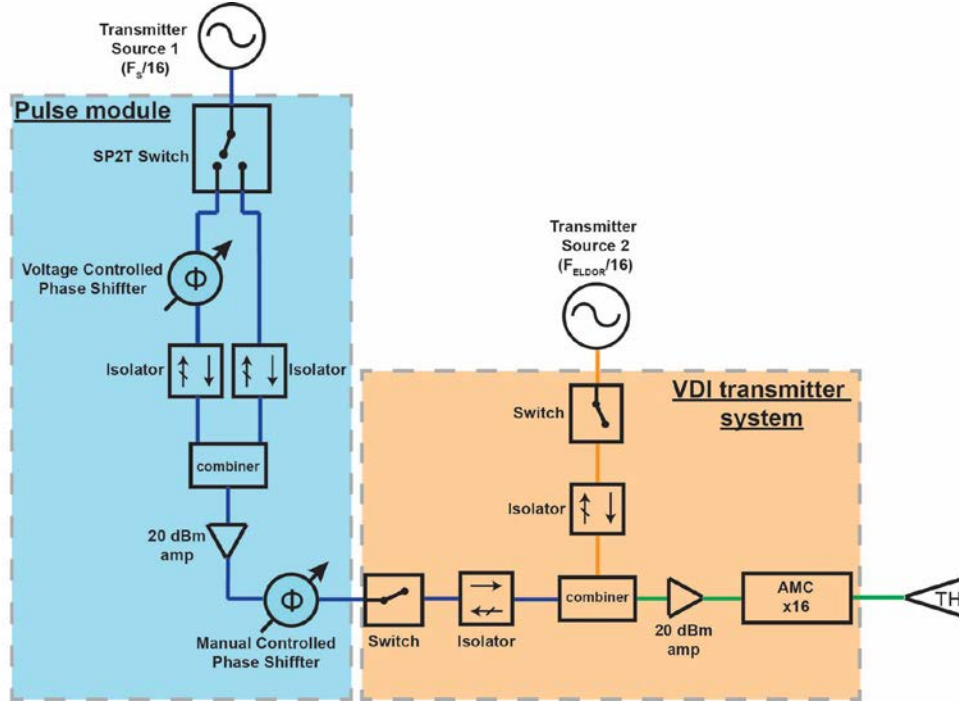


Figure 6 Schematic representation of the 12 GHz pulse forming unit. Orange block denotes MW components provided as part of the VDI transmitter system; blue block details the components of the homemade pulse forming unit. Blue line denotes the path of ~ 12 GHz signal at main (F_S) frequency generated by transmitter source 1. Orange line denotes the path of ~ 12 GHz signal at 2^{nd} (F_{ELDOR}) frequency generated by transmitter source 2. Green line denotes the path shared by both F_S and F_{ELDOR} signals. The detailed list of the MW components used in the pulse forming unit is provided in Appendix 10.3.

(3) Quasi-Optical System

A low loss QO system is important to ensure efficient MW transmission to the sample, isolating the reflected signal for EPR detection, and preventing reflected microwaves from damaging the transmitter source. In the QO configurations described below and shown in

Figure 7, each cube represents half of the 25 cm focal length (f) of the elliptical mirrors used in the system. All QO components described here are purchased from Thomas Keating Ltd. After exiting the MW source transmission horn, the incident vertically polarized MW beam (black arrows) passes through an isolator with the resulting polarization rotated by 45° . Subsequently, a 45° tilted wire grid polarizer is placed after the isolator such that the wires are perpendicular to the E-field of the microwave beam in order to allow complete transmission of the beam through the polarizer. The beam is then coupled to the waveguide and propagates to the sample.

The most sensitive EPR detection is achieved when the EPR signal is separated from the reflected microwave beam, known as induction mode detection. The incident microwave beam is linearly polarized and consists of an equal mixture of left and right circularly polarized MW, of which only one of the circularly polarized MW is resonant with the electron spins in the sample. The partial absorption of MWs by the sample results in a reflected MW polarization that is elliptical instead of linear. The elliptical MWs which travel back along the waveguide and exit back to enter the QO circuit will be split at the 45° tilted wire grid polarizer mentioned before, with the EPR signal reflected into the EPR detection system described below (dashed red arrows), while the rest of the MW beam passes through the wire grid polarizer and is dumped into the absorber that is part of the isolator (solid red arrows).

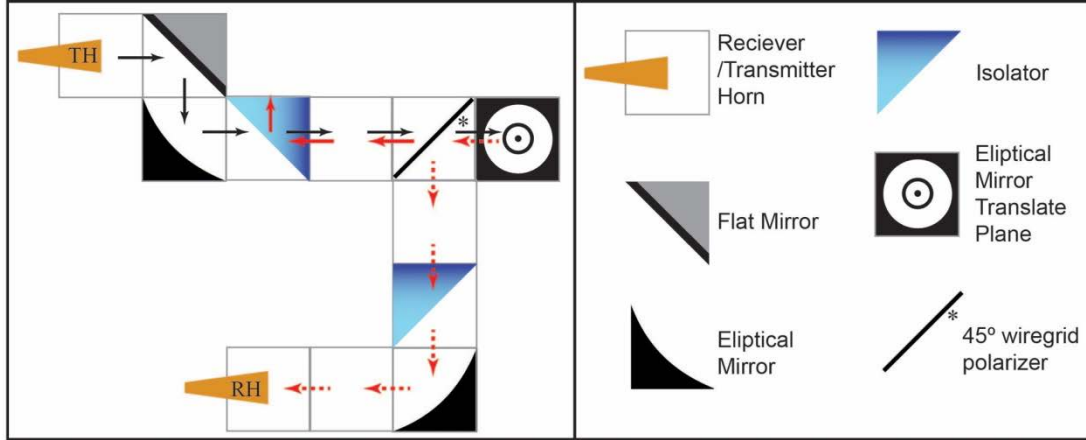


Figure 7. Schemes of different quasi optical circuits: (a) low-loss DNP configuration (b) Martin-Puplett DNP configuration, (c) dual DNP/EPR configuration. Each tile represents a distance of 12.5 cm ($f/2$). The dark portion of isolator indicates the position of the 45° Faraday rotator. Black arrows represent the incident mw beam; green arrows represent the microwave beam after recombining in a Martin-Puplett interferometer; solid red arrows indicate the reflected beam not carrying the EPR signal, which are directed to a MW absorber; dashed red arrows represent the reflected beam carrying the EPR signal directed to the receiver.

(4) EPR probe

From the QO circuit shown in Figure 7 the microwave beam is coupled to a corrugated waveguide spanning the length of the probe insert, shown in Figure 8. The corrugated MW waveguide (Thomas Keating, LTD) is held in the center of the probe insert and consists of a hollow cylinder made of german silver that is smooth on the outside but corrugated on the inside, such that the MWs guided to the sample are in contact with these corrugations. The corrugations of the waveguide ensure minimal MW power loss (~ 0.5 dB) of the HE_{11} MW mode. For a corrugated waveguide, the optimal coupling between the Gaussian TEM_{00} mode

and the HE_{11} mode of the waveguide requires a MW beam radius that is 0.64 times that of the waveguide radius.^[105] This will result in 98% coupling, where the 2% power difference is mainly converted to higher order modes.^[106,107] The inner diameter (ID) of the corrugated MW waveguide is 12.5 mm, and tapers to 5.3 mm to concentrate the MW beam to a smaller waist compatible with the sample size. After this waveguide taper, another 43 mm smooth wall copper waveguide extension guides the 5.3 mm waist MW beam to the sample and NMR probe located at the sweet spot of the magnet. The probe module (Figure X insert) and sample are placed at the end of the waveguide extension. To perform cw EPR, the probe module consists of a solenoid coil for B_0 field modulation, wound with 100 turns of 30 AWG magnet wire on an 11 mm outer diameter (OD) quartz tube.

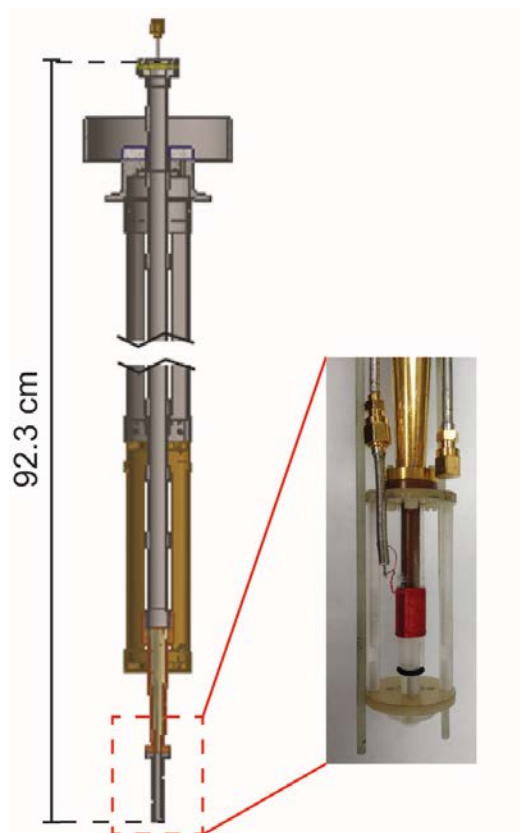


Figure 8. Details of the probe insert for NMR and EPR detection. (a) Structure of the probe insert with corrugated waveguide, (b) cross sectional sketch showing dimensions of the waveguide extensions

(corrugations not shown), (c) the four waveguide extensions listed from left to right: gold with Kel-F support, gold with plastic support, zirconia, and copper, (d) the probe modules with an inductively coupled ^1H Alderman-grant coil for DNP/NMR detection, (e) a modulation coil for EPR detection.

(5) EPR detection scheme

Superheterodyne detection (SHDD) is a conventional high field EPR detection method, since it combines high sensitivity with the added benefit of phase sensitive quadrature detection. Figure 9 shows a scheme of how phase-sensitive detection using the SHDD scheme is implemented in our system. In SHDD, the MW beam carrying the EPR signal at 200 GHz (F_{Signal}), is captured by the receiver horn and routed to a sub-band mixer (Virginia Diodes Inc.). The sub-band mixer down-converts the EPR signal into an intermediate frequency (IF) by mixing the EPR signal at frequency F_{Signal} ($\sim 200\text{GHz}$) with the reference frequency of the receiver system frequency F_{Receiver} ($\sim 98.5\text{GHz}$) to obtain a 3 GHz intermediate frequency EPR signal ($F_S - 2 * F_R = 3 \text{ GHz}$). A reference 3 GHz intermediate frequency is also generated by mixing receiver synthesizer, identical to the one used in the transmitter system, generates the frequency of $F_R/8$, which is subsequently fed into a x8 AMC to arrive at the required reference frequency of F_R . Note that the reference frequency F_R is selected such that the intermediate frequency is always exactly equal to 3 GHz by setting the receiver and transmitter MW (X-band) synthesizers 187.5 MHz apart ($F_S/16 - F_R/8 = 187.5 \text{ MHz}$). The 3 GHz EPR signal from this sub-band mixer is mixed again with an intermediate frequency reference at 3 GHz using an IQ mixer to arrive at two quadrature, absorption and dispersion, EPR signals at DC. In the case of pulsed EPR experiments

presented here, the EPR signal from the IQ mixer is sent directly to a fast (1 GHz), dual channel digital-to-analog converter (Acqiris; U1082A-002, Keysight Technologies). Depending on the particular experimental needs, the echo signal is digitized, and either the full (2 μ s) long trace is stored to the computer or the relevant part of the echo is integrated in real time and only the integral value is stored to the computer memory. In the case of CW EPR detection using SHDD, one would need to implement two synchronized lock-in amplifiers to demodulate each output of the IQ mixer independently.

The reference 3 GHz signal is created by mixing the outputs of the transmitter and receiver synthesizers, resulting in a 187.5 MHz frequency output from the mixer. This 187.5 MHz signal is subsequently multiplied x16 to arrive at the 3 GHz reference frequency to be inputted into the IQ mixer. A more detailed description of the IF stage showing every electronic component is presented in the Appendix, Fig. A2. Note that such a detection

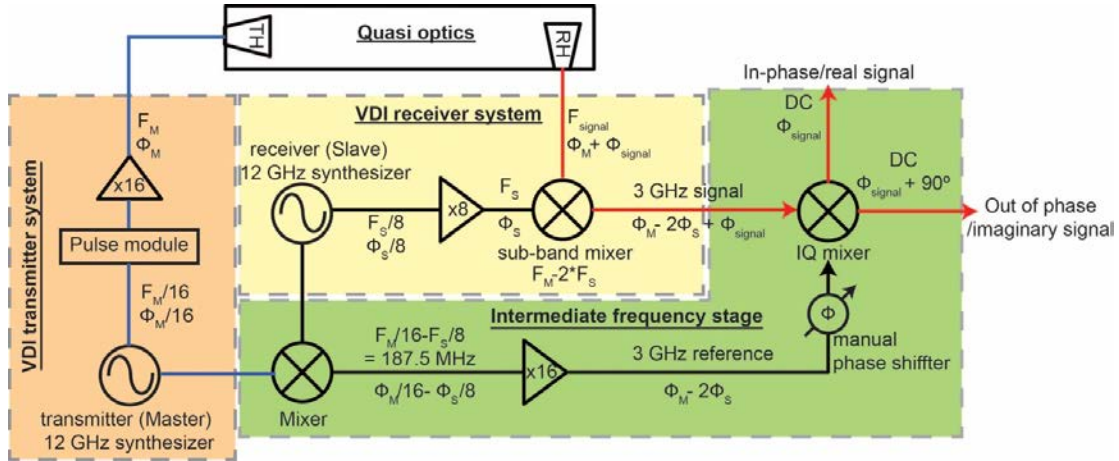


Figure 9. Schematic representation of the 200 GHz superheterodyne detection system. The yellow block denotes the VDI receiver system; orange block the VDI transmitter system and the green block denotes the IF stage (for full IF stage schematics see Appendix 10.2). Incident transmitted MW beam is denoted as dark blue lines; MW beam carrying EPR signal is shown as red lines. Reference frequencies are shown as black lines.

scheme involving an IF stage is insensitive to the relative phases between the transmitter and receiver sources, which allows for the acquisition of frequency-stepped EPR spectra if the two sources are stepped synchronously, maintaining the 187.5 MHz frequency difference, as was implemented in the frequency stepped echo detected experiments presented in the following section of this chapter. The phase and frequency at each stage in the EPR detection scheme are given in Figure 9.

C. Demonstration of EPR capabilities on Model Systems

To illustrate the CW EPR capabilities of our 200 GHz EPR system, we performed room temperature EPR experiments on a modeling clay sample containing Mn^{2+} ($S=5/2$; $I=5/2$) typically employed in testing EPR instrument performance. Figure 10 shows an overlay of the two CW EPR spectra of the Mn^{2+} containing clay sample. The spectrum shown in black was acquired with our 200 GHz EPR spectrometer stepping the frequency through the EPR spectrum. While stepping the frequency through the EPR spectrum is not a conventional EPR detection method, this method has been attempted by several groups with great success.^[108,109] This spectrum is overlaid with the spectrum shown in red after correct scaling, which was obtained with a 240 GHz EPR spectrometer in the laboratory of Professor Mark Sherwin (UCSB)^[101,110] using conventional field-swept CW EPR detection. The field-swept spectrum was converted to frequency units and inverted relative to its center, and then the center frequency subtracted from both spectra to allow for alignment of the frequency axis. Gratifyingly, the two spectra are in excellent agreement with one another. Both spectra show the typical Mn^{2+} sextet due to hyperfine interaction with the nuclear spin of ^{55}Mn ($I=5/2$). The six lines are equally spaced with 266 MHz separation, in

good agreement with values typically obtained for Mn^{2+} .^[111] Slight differences in the intensity of the two leftmost lines between the two spectra are attributed to the presence of residual standing waves in the QO system or to variations in incident MW power in the 200 GHz system that likely affects the effective B_1 field at the sample position in a MW frequency-dependent way. Fine tuning of the unique frequency stepped EPR experimental

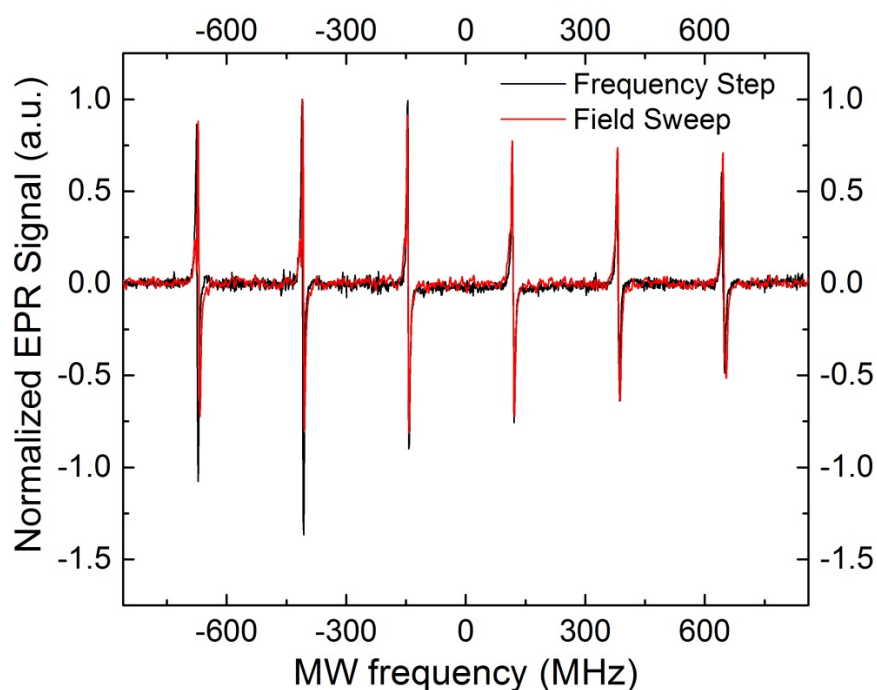


Figure 10. EPR spectrum of modeling clay containing Mn(II) for frequency swept EPR (black solid line) compared to a field swept spectrum of the same sample taken at 8.5 T (red dashed line). Experimental parameters- frequency sweep spectrum at 7.05 T (~ 200 GHz): MW power when irradiated with 22 ± 1 mW; modulation frequency: 20 kHz, modulation amplitude 0.26 mT, time constant: 30 ms, 10 scans, frequency stepping rate 10 Hz. Field sweep spectrum at 240 GHz: MW power 0.05 mW, field sweep rate: 0.1 mT/s, modulation frequency: 20 kHz, modulation amplitude 0.1 mT, time constant: 200 ms, 1 scan.^[110]

setup and dealing with these complications that are unique to the frequency stepped EPR approach is in progress.

To demonstrate the pulsed EPR capabilities of this system several standard pulsed EPR experiments were performed as shown in Figure 11. Fig. 11a shows the overlay of the echo detected *frequency stepped* spectrum of P1 (nitrogen) centers of a type 1b diamond acquired on our 200 GHz system (black trace) with the echo detected *field swept* EPR spectrum (red trace) acquired at 240 GHz in the laboratory of Professor Mark Sherwin (UCSB), where both spectra were acquired at room temperature for the same sample. The two spectra show the characteristic triplet due to the hyperfine interactions of the unpaired electron in the P1 center with ^{14}N . Similar to what is previously observed in the CW EPR spectra comparison (Figure 10) between the two systems, the line positions and linewidth are consistent between the two, while the line intensities are not. Again, this is attributed to the presence of frequency dependent standing waves in the 200 GHz system and to variations of incident power across the frequency range used to acquire the EPR spectrum.

One of the strengths of pulsed EPR in relation to elucidating DNP mechanism lies in its ability to directly probe the relaxation properties of the electron spins participating in DNP. Accordingly, we demonstrate relevant pulsed EPR capabilities by measuring the phase memory time, T_M , (Figure 11b) using a two-pulse (t_p - τ - t_p - τ -echo) solid echo pulse sequence (see Fig. 13b inset) where τ is varied, and the electron spin-lattice relaxation time, T_{1e} , (Figure 11c) using a three-pulse saturation recovery (t_{sat} - t_d - t_p - τ - t_p - τ -echo) pulse sequence (Figure 11c inset) where t_d is varied. Both experiments were carried out on the central line of the P1 center triplet of the same diamond sample at room temperature (290 K). Both curves could be satisfactorily fitted with a single exponential, and the obtained values of $T_M = 965$

ns and $T_{1e} = 1.6$ ms are in good agreement with measurements performed using the 240 GHz EPR setup in the Sherwin group at UCSB on the same diamond sample.

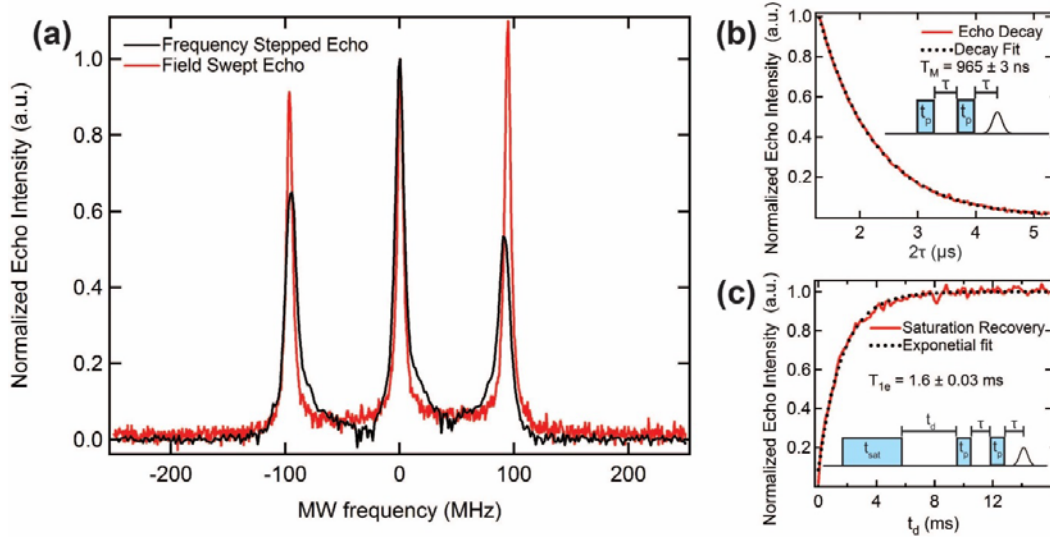


Figure 11. (a) 200 GHz frequency stepped echo detected spectrum (black) and 240GHz field swept echo detected EPR spectra of P1 centers in diamond. (b) Two pulse echo decay (red) and mono-exponential fit (black). (c) Saturation recovery experiment using the $t_{sat} - t_d - t_p - \tau - t_p - \tau$ -echo pulse sequence (inset of c) varying the t_{sat} (red) and mono-exponential fit (black). The pulse sequence $t_p - \tau - t_p - \tau$ -echo (inset of b) was used in (a) and (b); Experimental parameters (a, black): $F_S = 197.3$ GHz – 197.8 GHz; $t_p = 300$ ns; $\tau = 500$ ns; repetition time 2 ms; (a, red): magnetic field 8.578 T – 8.589 T; $t_p = 500$ ns; $\tau = 900$ ns; repetition time 10 ms; no phase cycling (b) $t_p = 300$ ns; varying $\tau = 500$ ns – 2600 ns; repetition time = 2 ms. (c) $t_{sat} = 20$ ms; $t_p = 300$ ns; $\tau = 900$ ns; varying $t_d = 1$ μs – 16000 μs; repetition time = 40 ms. For all experiments the magnetic field was set to 7.05 T.

Similar to NMR, nutation experiments by pulsed EPR can be used to directly determine the strength of the oscillatory magnetic field B_1 at the sample position. A three pulse nutation experiment ($t_{sat} - t_d - t_p - \tau - t_p - \tau$ -echo) (Fig. 12a inset) where the length of the first “ t_{sat} ” pulse is varied was used to probe the B_1 strength. The experiment was carried out at 4 K and 7 T, with 40 mM 4-amino-TEMPO radical in a frozen glass of 60:30:10 v% D₈-glycerol:D₂O:H₂O, using the full available MW power of ~140 mW at $F_M = 197.925$ GHz. The EPR nutation curve is presented in Fig. 12a, with the nutation trace showing a decaying

oscillation typical of echo detected nutation experiments, where the decay of the oscillation is attributed to inhomogeneous B_1 field distribution over the sample. The first minimum of the nutation curve occurs at 850 ns (black arrow in Fig. 12a) corresponding to a nutation frequency of ~ 0.6 MHz, and a conversion factor of $1.66 \frac{\text{MHz}}{\sqrt{\text{Watt}}}$. This B_1 field at 7 T is consistent with non-resonant MW excitation schemes used for other ~ 200 GHz EPR setups where ~ 100 mW output MW sources result in several hundred nanosecond $\pi/2$ pulses.^[112,113] For MAS-type DNP setups with non-resonant MW excitation, much higher MW powers might be needed, such as 17 W to produce a 0.84 MHz B_1 strength, as recently calculated by Barnes et al. for a gyrotron powered setup.^[114]

The two transmission synthesizers in the Han lab EPR spectrometer allow for the acquisition of double resonance EPR experiments such as ELDOR, where the electron echo is detected at one frequency (F_{detect}) after prolonged MW irradiation F_{ELDOR} frequency. The F_{ELDOR} frequency is then swept over the entire EPR spectrum. The overall pulse sequence of the ELDOR experiment $t_{\text{sat}}(F_{\text{ELDOR}}) - t_d - t_p(F_{\text{detect}}) - \tau - t_p(F_{\text{detect}}) - \tau - \text{echo}$ is shown in the insert of Fig. 14b. In this experiment the echo intensity at F_s frequency is monitored as a function of the F_{ELDOR} frequency. An example of such an ELDOR spectrum acquired at 4 K on the 40 mM 4AT radical in d_8 -glycerol: D_2O : H_2O (60:30:10 v%) is shown in Fig. 12b. Here the detection F_s frequency was set to the maximum EPR signal of the nitroxide spectrum at 197.925 GHz and the F_{ELDOR} frequency was varied across the whole nitroxide spectrum between 197.3-198.4 GHz. The spectrum shows full depolarization at $F_{\text{ELDOR}} = F_s$ with a significant depolarization observed up to $F_{\text{ELDOR}} = 197.5$ GHz on the low frequency and $F_{\text{ELDOR}} = 198.3$ GHz on the high frequency side of the spectrum, spanning almost 1 GHz. The broad depolarization pattern is attributed to a strong spectral diffusion previously

reported for nitroxide radicals at similar concentrations as measured by similar ELDOR experiments at 95 GHz,^[52] but at much lower temperatures of 4 K where the effect of EPR saturation will be greater, in part owing to the long T_{1e} . It was demonstrated that from a series of such ELDOR spectra acquired for several “probe” F_S frequencies, it is possible to reconstruct the saturation pattern of the EPR operating conditions. These types of experiments will reveal the extent (width spectrum under DNP conditions—which is drastically different from any normal EPR and depth) of saturation under conditions where maximum DNP enhancement or oversaturation occurs in systematic future studies. The benefit of ELDOR measurements to help rationalize DNP mechanisms under static conditions has been demonstrated recently at 3.3 T and 95 GHz EPR frequency by Hovav et al.^[52,89] However, ELDOR under CW DNP conditions and at higher magnetic fields such as our 7 T system is not reported to date. Taken together, we have demonstrated here that the versatility of our combined DNP/EPR approach that relies on the frequency-tunable and amplitude modulation-capable solid state MW source and QO transmission enables a variety of pulsed EPR experiments, and that many more variations of EPR experiments can be implemented with ease.

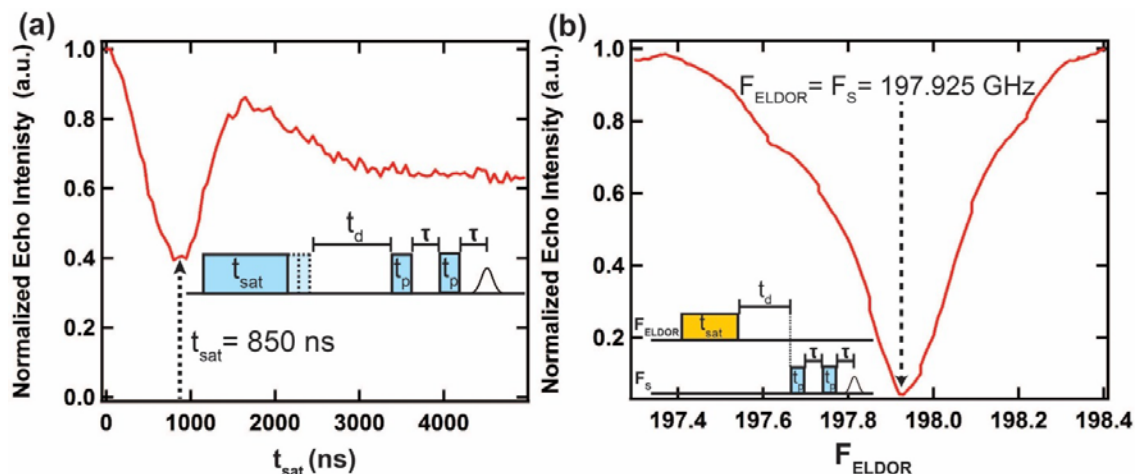


Figure 12. (a) Echo detected nutation experiment at $F_S = 197.925$ GHz; Experimental parameters: $F_S = 197.96$ GHz; $t_p = 500$ ns; $\tau = 500$ ns; variable $t_{\text{sat}} = 0 - 5000$ ns; $T = 4$ K; magnetic field 7.05 T. (b) 200 GHz ELDOR spectra of 40 mM 4AT acquired using the $t_{\text{sat}}(F_{\text{ELDOR}}) - t_d - t_p(F_S) - \tau - t_p(F_S) - \tau$ -echo pulse sequence shown in the insert. Experimental parameters: $F_S = 197.925$ GHz; $F_{\text{ELDOR}} = 197.3 - 198.4$ GHz; $t_{\text{sat}} = 50$ ms; $t_p = 500$ ns; $\tau = 500$ ns; two step phase cycle.

D. Conclusion

This chapter has presented an operational conversion of a DNP/NMR spectrometer to an EPR instrument and system operating at a B_0 field of 7 T and powered by a solid-state MW source, whose MW transmission and detection is controlled by a QO MW bridge. The versatility of the solid-state MW source and modularity of the QO transmission system enables the manipulation of the system to perform different types of measurements, such as carry out CW and pulsed EPR measurements, including double resonance measurements

with the addition of a second synthesizer. Our VDI synthesizers and low loss QO allows for $\pi/2$ time of 600 ns for a spin $1/2$ system corresponding to 0.4 MHz, which is on par or greater than similarly configured EPR spectrometers. A comparison of our method of microwave frequency stepped CW measurements and frequency stepped pulsed echo measurements as a method for acquiring the EPR lineshape shows good agreement with the traditional field swept measurements. However it is clear from the amplitude mismatch that standing waves are present in the system and effect the measured intensity of spectrum. This can be combatted by the addition of an isolator at the end of the waveguide before the sample, but this will also increase the microwave transmission loss through the system. The implementation of pulsed EPR also enables insightful ELDOR experiments that will facilitate the understanding of DNP processes such as nuclear depolarization. The dual EPR/DNP capabilities will greatly increase the ability to explore the DNP parameter space. In summary, we have demonstrated that the reliability, versatility, and modularity of our dual DNP/EPR instrument creates an excellent configuration to explore the DNP performance of different samples and experimental conditions in order to study the spin physics of DNP.

III. Effect of Nitroxide Radical Electron Spin Dynamics on Nuclear Depolarization under MAS

A. Introduction

Dynamic Nuclear Polarization (DNP) combined with Magic Angle Spinning (MAS) Nuclear Magnetic Resonance (NMR) has been shown to be a powerful tool for elucidating molecular structural information of a variety of biological compounds^[7,8,67] and surface structures of material systems.^[10,11,115,116] The signal enhancement from DNP-MAS has led to drastic time savings, reducing experiment times from days to hours and enabling NMR experiments that were not feasible before such as natural abundance heteronuclear correlation measurements.^[9,13] DNP is a method of transferring the polarization from unpaired electron spins on DNP polarizing agents to dipolar coupled nuclear spins. Because of the broad potential for DNP to enhance the capabilities of solid-state MAS NMR well beyond its current state of the art, much work has gone into designing the ideal radical-based DNP agents for maximum signal enhancement at high magnetic fields.^[37,38,40,54,58,81,83,84] Much of the current development has focused on tethered nitroxide bi-radicals such as totapol,^[38] amupol^[39] and tekpol,^[37] while there are also studies of tri-radicals such as dotopa^[41] and radical mixtures,^[42,43] but the design of potent multi-radicals for DNP, in particular under MAS conditions, is still debated and relies on empirical trial and error as the contributing factors are not entirely understood. Much of the theory of the cross effect mechanism under MAS has been detailed by Tycko, Thurber and Vega.^[45,46,68,69]

The cross effect (CE) mechanism can simplistically be defined as the following: two dipolar coupled electron spins which have a frequency offset that is approximately equal to the hyperfine coupled nuclear Larmor frequency undergo an energy conserving polarization

transfer that can cause a buildup of nuclear spin polarization. Microwaves are used to create a large polarization difference between the two electron spins that fulfill the CE condition, $\omega_{e1}-\omega_{e2}=\omega_n$, through saturation of a portion of the EPR spectrum of the nitroxide radical—this large polarization difference is then transferred to the coupled nuclear spins. The large g-anisotropy of the nitroxide radical causes the resonant frequency of the electron spin to oscillate over the course of the MAS rotor period, resulting in multiple different crossings of dipolar coupled electron spins and fulfilling the CE conditions throughout the rotor period, as detailed by Thurber et. al.^[45] These crossing events increase the effectiveness of the CE under MAS with microwave irradiation, however this process can also lead to a depolarization of the nuclear spins under MAS in the absence of microwave irradiation. Thurber and Tycko^[89] first reported that spinning a sample with a nitroxide spin causes a reduction in the nuclear polarization below thermal Boltzmann polarization. Typically signal enhancement factors from DNP have been the main factor in demining the effectiveness of a DNP radical, where the signal enhancement is calculated by the NMR signal area with microwave irradiation divided by the NMR signal without microwave irradiation. This nuclear depolarization effect artificially lowers the unenhanced (microwave off) NMR signal, i.e. the denominator in calculating the enhancement factor, and therefore can result in DNP enhancement factors that do not represent the true NMR signal sensitivity gain by DNP, as systematically presented by recent studies.^[70,117]

One variable that appears to be a critical modulator of nuclear spin depolarization is the spin lattice relaxation time of the electron spin (T_{1e}). The polarization difference between electron spins that fulfill the CE requirement ($\omega_{1e}-\omega_{2e} = \omega_n$) is shifted by MAS depending on the spinning rate relative to $1/T_{1e}$, simulated at 9.4 T by Thurber and Tycko.^[69] This finding

is consequential because many contemporary bi-radicals are designed to increase the efficiency of the cross-effect mechanism through an increase in T_{1e} . However, direct measurements of T_{1e} under the conditions of DNP experiments are missing in the literature. In addition, thus far the majority of theoretical descriptions of the CE do not extend beyond the three-spin system, with the notable exception of Vega and Goldfarb, who introduced a semi-empirical method of determining how a network of dipolar coupled electron spins affects the DNP process by quantifying the extent of electron spectral diffusion through electron double resonance measurements (ELDOR). The extent to which spectral diffusion plays a role in equalizing the polarization the electron spins in the CE process and its effect on nuclear depolarization have not been discussed in literature.

In order to develop rational models for describing CE DNP processes under MAS, as well as to design optimal DNP agents and choose favorable DNP experimental conditions, it is important to experimentally test and validate key assumptions made with EPR measurements at the same DNP conditions, i.e. high magnetic field. Here we employ the Han lab's home-built EPR spectrometer, described in Chapter 2, to empirically measure the T_{1e} and spectral diffusion parameters of various mono-, bi-, and tri- nitroxide radicals at 7 T and compare these T_{1e} measurements with the strength of the nuclear spin depolarization effect under MAS. These types of EPR measurements have great potential to aid in development of radicals for magnetic fields of 11 T and greater, where CE DNP efficiency has been shown to greatly decrease when employing nitroxide bi-radicals.^[118]

B. Experimental

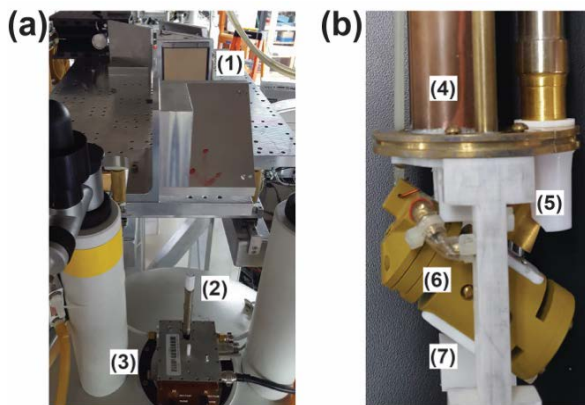


Figure 13. (a) Quasi-optical Bridge with (1) isolator and two focusing parabolic mirrors, (2) microwave waveguide extending from top of (3) 4 mm Revolution NMR LLC. probe. (b) Bottom of probe head, (4) radio frequency transmission line, (5) Thomas Keating Ltd. corrugated waveguide with miter bend, (6) stator, and (7) cooling helium gas inlet

MAS-DNP/NMR Measurements

NMR/DNP measurements were performed with a Revolution NMR LLC MAS probe outfitted with a Thomas Keating Ltd corrugated waveguide inside a 7 T Bruker wide bore magnet. A Virginia Diode Inc. microwave source with a frequency range from 193-201 GHz with nominal output power of 140 mW was employed in a quasi-optical bridge as shown in Figure 13. Two parabolic focusing mirrors focus the microwave into the corrugated waveguide that extends from the top of a MAS probe. Room temperature nitrogen gas is used for the bearing and drive of the probe, and cold helium gas is used to cool the sample space, using a stator similar to that described by Thurber et. al.^[96] A 20 mM electron spin concentration solution of each radical species was made by dissolving the radicals in 60:30:10 v/v% D₈-glycerol:D₂O:H₂O. A zirconia rotor with an outer diameter of 4 mm, an inner diameter of 2.36 mm, a length of 46 mm, and a total sample volume of 0.044 mL was employed. The sample was centered in the rotor using two Teflon spacers at either end of the rotor. The sample was packed by first loosely packing 60 mg of KBr, then 20 mg of the

radical solution was pipetted in the rotor and gently mixed. KBr was added in order to monitor the sample temperature *in situ* through the measurement of ^{79}Br $T_{1\rho}$ as well as to increase the DNP enhancement as observed by Thurber and Emsley. The ^{79}Br $T_{1\rho}$ temperature calibration and enhancement increase are detailed in Appendix C. The resulting NMR signal was recorded with a Bruker Advance 300 MHz spectrometer.

7 T Pulsed EPR Measurements

All EPR measurements were performed on the Han lab's home-built dual static DNP/EPR spectrometer operational at 193-201 GHz, described in Chapter 2. This spectrometer employs the same Virginia Diode Inc. microwave source used in the MAS-DNP measurements. A quasi-optic scheme focuses the Gaussian microwave beam to a corrugated waveguide at the center of a home built static EPR probe inside a Bruker 7 T wide bore magnet. This EPR spectrometer employs a phase sensitive induction mode detection scheme, where the ~200 GHz EPR signal is mixed down to 3 GHz then mixed with a 3 GHz reference signal. The DC in-phase and out-of-phase signal components are then processed using the SpecMan4EPR software. Details of the dual EPR/DNP spectrometer quasi-optic, probe, and detection design are detailed by Siaw et. al.^[119] The electron spin-lattice relaxation time (T_{1e}) of the nitroxide radical solutions were measured using a saturation recovery solid echo detection pulse sequence. A second VDI source is employed for EPR double resonance measurements (ELDOR), where the second source provides a saturation pulse to the electron spin system and the first source detects the resulting electron spin echo. The saturation source frequency is then stepped across the entire EPR spectrum while the detection frequency is held constant. The ELDOR spectrum

was collected for three different constant detection frequencies, $F_{\text{detect}} = 193.52$ GHz, 193.887 GHz, and 194.1 GHz. The ELDOR spectra were simulated using the Matlab software package EasySpin and a modified simulation script developed by Hovav et. al.^[89] in order to derive a relative spectral diffusion parameter for each nitroxide radical frozen solution.

C. Results

Depolarization and Absolute DNP enhancement

The packed rotor was placed in the MAS stator and liquid helium was used to cool the sample space until an average temperature of 24 K was reached, while room temperature nitrogen gas was used for the bearing and drive. The sample temperature was recorded by measuring the $T_{1\rho}$ of ^{79}Br before and after the enhancement measurement, and the average sample temperature was 24 K \pm 2 K. Appendix C Figure 1 shows the temperature stability for all samples measured. The ^1H enhancement of each radical solution was determined by the ratio of ^1H NMR signal with microwave irradiation divided by the NMR signal without microwave irradiation ($\epsilon_{\text{MWon/off}}$). Figure 14 shows the $\epsilon_{\text{MWon/off}}$ as the spinning speed is increased. The various mono, bi, and tri-radicals follow a similar enhancement factor trend: there is an initial increase in enhancement from static to 1 kHz for each radical, with amupol yielding the largest $\epsilon_{\text{MWon/off}}$ of all the radicals at 1 kHz spin rate with an $\epsilon_{\text{MWon/off}} = 38$. As the spinning speed is increased, there is a significant decrease in $\epsilon_{\text{MWon/off}}$ for all radicals measured. At 3 kHz the $\epsilon_{\text{MWon/off}}$ of amupol falls below the $\epsilon_{\text{MWon/off}}$ of Dotopa-ethanol and at 5 kHz spin rate DOTOPA-ethanol showed the largest $\epsilon_{\text{MWon/off}} = 17$, followed by amupol, then totapol and 4AT which both gave an $\epsilon_{\text{MWon/off}} \sim 5$ at 5 kHz. From just looking at the $\epsilon_{\text{MWon/off}}$ one would conclude that Dotopa-ethanol is the best radical for 20 K MAS DNP.

However, as discussed in the introduction, recent observations show that the $\epsilon_{\text{MWon/off}}$ is not an accurate representation of the NMR signal gained through DNP because the addition of the nitroxide radicals can lower the observed NMR signal without microwave irradiation through the depolarization and paramagnetic bleaching effects described in the introduction. Figure 14(b) shows the ^1H NMR signal reduction for each frozen radical solution as the sample spin rate is increased, where the NMR signal has been normalized to the ^1H NMR signal at 0 kHz spin rate. Both bi-radicals (totapol and amupol) and the tri-radical dotopa-ethanol show a signal decrease as spinning speed is increased, whereas 4-amino TEMPO and the sample without a radical remain fairly constant with spinning speed. This reduction below thermal polarization as the spin rate is increased is characteristic of the depolarization effect as described by Thurber and Tycko. The depolarization factor was quantified as the ^1H NMR signal intensity at 0 kHz / ^1H NMR signal intensity at 5 kHz spin rate without microwave irradiation.

In order to calculate the absolute sensitivity gain ($\epsilon_{\text{absolute}}$) one must take into account the paramagnetic bleaching, where proximity to a free electron spin causes the nuclear T_2 shorten beyond detection.^[70,117,120] The paramagnetic bleaching factor is defined as the static (0 kHz) ^1H NMR signal intensity without radical in the solvent divided by the ^1H NMR intensity of the sample with the nitroxide radical at 0 kHz. The absolute signal enhancement ($\epsilon_{\text{absolute}}$) at 24 K is the $\epsilon_{\text{MWon/off}}$ divided by the depolarization factor and paramagnetic bleaching factor. The $\epsilon_{\text{absolute}}$ for each radical is shown in Figure 14(c). Here we see that Dotopa-ethanol shows marginally larger enhancement than the rest of the radicals measured at 1 kHz but as the spinning speed is increased to 5 kHz all the radicals show similar enhancement. Mentink-Vigier et. al. observed with a commercial Bruker DNP system at 94

K and 9.4 T the $\epsilon_{\text{absolute}}$ of amupol was only ~ 1.5 times that of totapol as opposed to an $\epsilon_{\text{MWon/off}}$ 3.3 times that of totapol.^[70] In our QO DNP system at 24 K at 7 T we observe that when accounting for depolarization and paramagnetic quenching amupol and totapol have the same absolute enhancement. We hypothesize that this is due to the power limit of our 140 mW microwave source- with such low power the DNP enhancement is not enough to fully overcome the depolarization effect. This will be tested in future studies with a 500 mW microwave source from Virginia Diode Inc., since with higher microwave power the enhancement difference between toapol and amupol should be more pronounced.

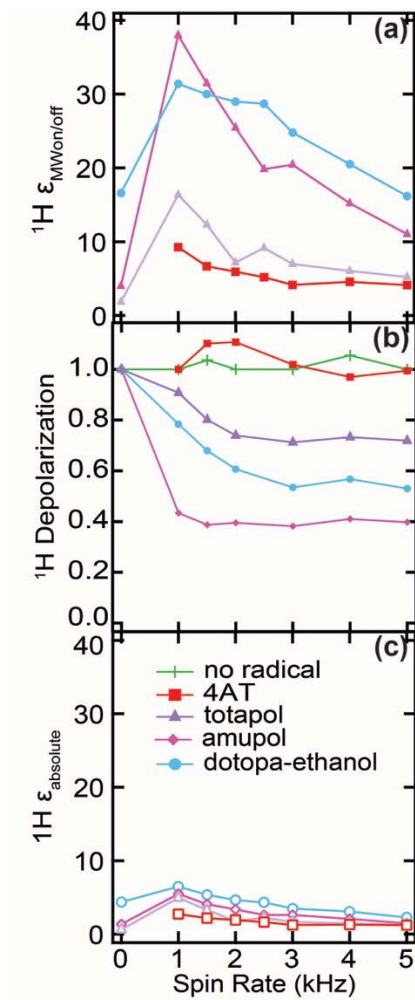


Figure 14. (a) Enhancement vs. spin rate, the enhancement was calculated from MW on / MW off signal of 4amino-TEMPO (red), totapol (purple), amupol (pink), and dotopa-ethanol (blue). (b) The NMR signal decrease vs. spin rate without microwave irradiations, normalized to the NMR signal at 0 kHz. (c) The absolute ^1H NMR signal enhancement vs. spin rate for each radical frozen solution after correcting for paramagnetic bleaching and depolarization effect.

Effect of Electron Spin-Lattice Relaxation Time on Depolarization

Using our static 7 T EPR spectrometer we have measured the T_{1e} for these radical species at 24 K with an echo detected saturation recovery pulse sequence shown in the inset of Figure 15(a) at a microwave frequency of 193.887 GHz. The resulting saturation recovery decay curve is shown in Figure 15a. This is fit to equation (3),

$$\text{Equation (3)} \quad M_t = 1 - a \cdot \exp\left[-\frac{t}{T_{1e}}\right] - b \cdot \exp\left[-\frac{t}{T_{SD}}\right]$$

where T_{1e} is the electron spin lattice relaxation time and T_{SD} is a faster spectral diffusion time that is due to the microwave pulses only exciting a portion of the EPR line.^[121] Figure 15(b) shows the measured depolarization factor plotted against the experimentally measured T_{1e} for each frozen radical solution. Figure 15(b) shows that longer T_{1e} correlates to larger ^1H depolarization under MAS, with amupol having the longest T_{1e} and largest depolarization. To further demonstrate this relationship between T_{1e} and depolarization, GdCl_3 was added to the dotopa-ethanol solution at a concentration of 0.1 mM and 1 mM. These concentrations have been shown to not affect the NMR linewidth or T_{1n} .^[122] Here we observe with 0.1 mM Gd^{3+} the T_{1e} of the dotopa-ethanol is reduced from 4 ms to 2 ms and the depolarization factor correspondingly reduced by 32%. After the addition of 1 mM of Gd^{3+} to the dotopa-ethanol solution the T_{1e} is reduced to 0.1 ms and the depolarization factor is reduced by 98 %, so essentially no nuclear depolarization was observed.

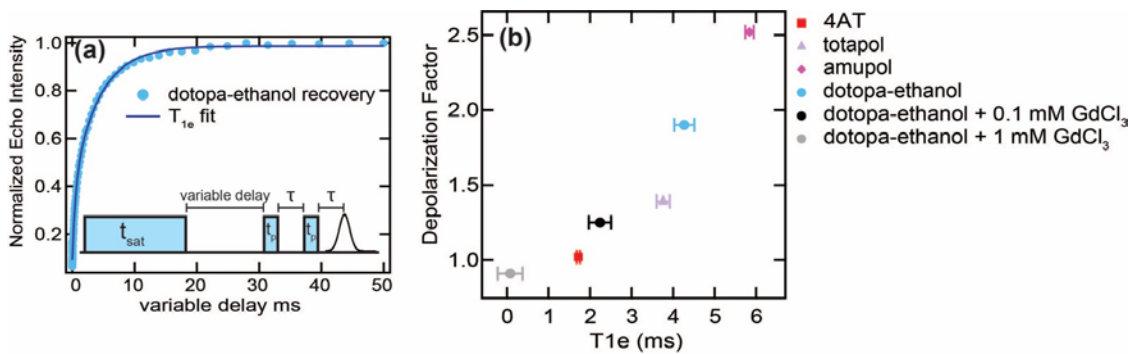


Figure 15. (a) Example electron echo saturation recovery and T_{1e} fit. (b) Depolarization factor measured at 5 kHz vs. T_{1e} of all radicals measured. There is a clear correlation between longer T_{1e} and larger depolarization factor.

To understand the effect of T_{1e} on nuclear depolarization under MAS we again invoke the description of the three spin CE process described in Chapter I section C. Figure 16 shows the energy level diagram for a two electron one nuclear spin system. The CE condition is fulfilled at multiple time points during the rotor period where an electron nuclear flip-flop may occur. The direction of this polarization transfer, either resulting in DNP enhancement or nuclear depolarization, is dependent on the polarization difference between the two electron spins involved in the CE. Irradiation with microwaves at ω_{e1} causes a large polarization difference between e_1 and e_2 driving the DNP enhancement process, however in the absence of microwaves the e- flip-flop crossings where $\omega_{1e} = \omega_{2e}$ cause an equalization in the electron spin polarization between e_1 and e_2 . The polarization of the coupled nuclei will then equilibrate to the difference in polarization between e_1 and e_2 , resulting in a decrease in nuclear polarization below thermal Boltzmann polarization. Thurber and Tycko simulated that increasing the T_{1e} of the radical species results in a greater equalization of electron spin polarization across the entire nitroxide EPR line, and therefore longer T_{1e} would lead to greater nuclear depolarization under MAS. The T_{1e} measurements vs. depolarization factor we observe are consistent with this explanation where longer T_{1e} was found to cause an increased observed nuclear depolarization.

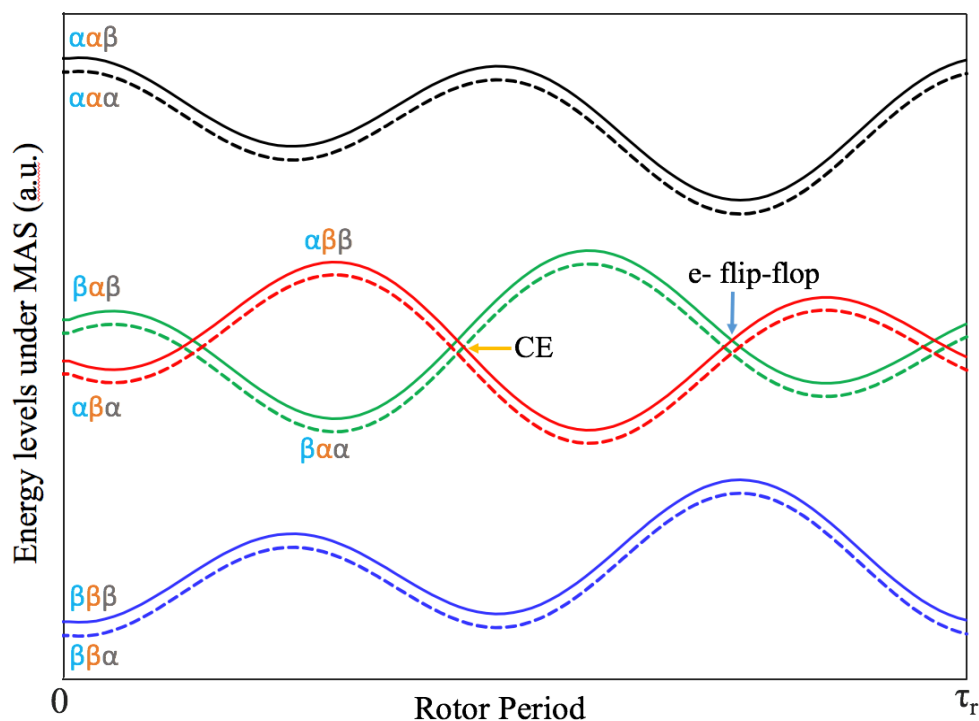


Figure 16. Energy level diagram under over a single rotation cycle of the MAS rotor. CE points are crossing points where the electron and nuclei can exchange polarization. e- flip-flop are crossing points where the electron spins can exchange polarization, and equalize the electron polarization. Simulation of energy levels under MAS done in the Spin Evolution program for simulating NMR.

Effect of Electron Spectral Diffusion Rate on Depolarization

The important parameter for determining the extent of nuclear depolarization is the equalization of the electron polarization across the EPR under MAS. One parameter that has been omitted thus far from the simulations and understanding of depolarization is electron spectral diffusion, which describes how a network of dipolar coupled electron spins

distribute polarization across the EPR line. Hovav et.al.^[89] have shown under typical DNP conditions, where nitroxide spin concentrations are in the 10s of mM, there is a network of dipolar coupled electron spins which lead to a large spectral diffusion term, such that a change in polarization of one electron spin can affect the polarization of another electron spin 100s of MHz away in frequency space. The extent to which spectral diffusion affects MAS is unknown, largely due to the specialized EPR spectrometer requirements for performing the double resonance electron measurements (ELDOR).

The ELDOR spectrum was measured using two VDI microwave sources. A saturation pulse is applied at a frequency of $F_{\text{Saturation}}$ then the electron echo is detected using a different microwave source with frequency F_{detect} . $F_{\text{Saturation}}$ is swept over the EPR line while F_{detect} is held constant, and this method was repeated for three different detection frequencies. The ELDOR pulse sequence and resulting spectra for $F_{\text{detect}}=193.52$ GHz are shown in Figure 17 for amupol and 4AT, and the ELDOR spectra of all detection frequencies and radicals are shown in Appendix Figure X. The large peak at -390 MHz offset (*1 in figure 17) is where the $F_{\text{Saturation}} = F_{\text{detect}}$. The peaks at -360 MHz are representative of the electron coupling to ^{14}N (reference), the peak at position -340 MHz is due to the electron hyperfine coupling to ^2H (*3), and the sharp peaks at -90 MHz and -690 MHz offset are due to ^1H hyperfine coupling to the electron spin (*2). The electron depolarization for *2, *3, and *4 are direct observations of the solid effect transitions for the various nuclei in the system. The broad peak at the center of the EPR line (*4) is due to spectral diffusion between the spins irradiated at $F_{\text{Saturation}}$ and the detected spins at F_{detect} . This is most noticeable at the central transition of the EPR line where the largest electron spin population lies. Microwave irradiation at the central EPR line, with $F_{\text{Saturation}} = 0$ MHz offset, depolarizes the electron

spins at the detected frequency of -90 MHz offset. This phenomenon was observed for nitroxide spin concentrations in the 10's of mM by the Vega and Goldfarb groups at temperatures of 10-4 K.^[52,89] The Vega and Goldfarb groups developed a method of simulating the electron depolarization polarization in the ELDOR spectrum.

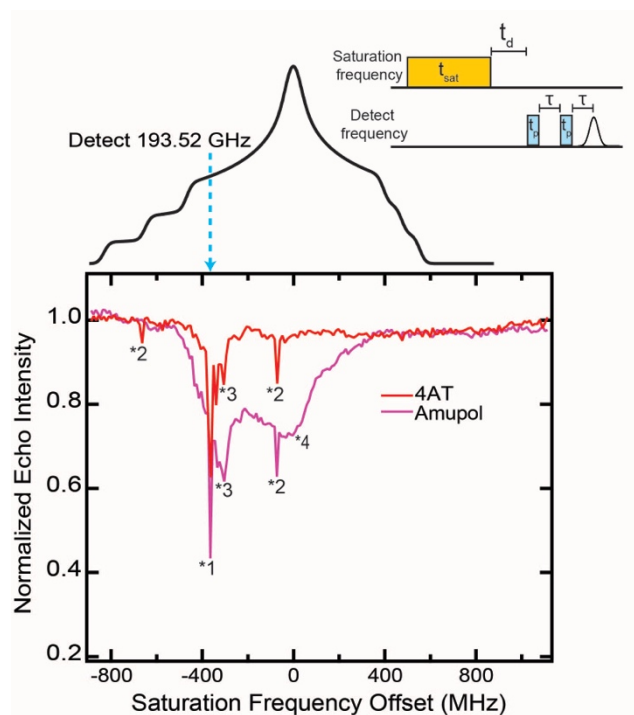


Figure 17. (Top) Simulated EPR line of 10 mM amupol in DNP juice. (Bottom) ELDOR spectrum of 4-amino TEMPO (4AT) and Amupol at a detection frequency of 193.52 GHz. Peak labels are as follows: (*1) where the detection frequency equals the saturation frequency, (*2) Hyperfine coupling to the 1H spin in system, (i.e. 1H solid effect), (*3) hyperfine coupling to 2H and 14N, and (*4) broad peak at center of the EPR line due to spectral diffusion between irradiated and detected electron spins.

The nitroxide line is inhomogenously broadened due to the anisotropy in the g-tensor free electron spin. The simulated nitroxide EPR line can be divided into packets of electrons, “bins”, with the same average frequency (ν_j), average polarization (P_e), and bin frequency

width (Δ_{bin}). Each bin contains a number of electrons f_j , given by the EPR normalized lineshape. The polarization of the bins are calculated by solving a set of coupled rate equations for all $P_e(\nu_j)$. The rate constants in these coupled rate equations are dependent on MW irradiation frequency and amplitude, T_{1e} , T_{2e} , and the polarization exchange rate between the bins $\overline{w}_{j,j'}^{\text{eSD}}$ as defined by the eSD exchange constant (Λ^{eSD}) given in equation 4,

$$\text{Equation 4.} \quad \overline{w}_{j,j'}^{\text{eSD}} = \frac{\Lambda^{\text{eSD}}}{(\nu_j - \nu_{j'})^2}$$

where $(\nu_j - \nu_{j'})$ is the frequency difference between two bins. The simulated ELDOR profiles are constructed from the experimentally determined values of f_j , T_{1e} , and electron spin concentration.

To simulate the ELDOR profile, first the nitroxide EPR lineshape was simulated using the EasySpin simulation package for matlab. The simulated EPR line was then divided into frequency bins, and using equation 4 the spectral diffusion rate $\overline{w}_{j,j'}^{\text{eSD}}$ was simulated between the different bins. Figure 18 shows a cartoon representation of the ELDOR simulations. From $\overline{w}_{j,j'}^{\text{eSD}}$ the Λ^{eSD} is determined, which is a phenomenological parameter that can be thought of like a pseudo rate constant, i.e. the larger the lambda values the greater the rate of spectral diffusion between spins across the EPR line.

Using this method the lambda values were simulated for ELDOR spectra obtained from three different detection frequencies (-390 MHz, 0, and +400 MHz offset from the central

EPR transition). Representative experimental data and simulation for amupol is shown figure 19 (top). The simulation takes into account the electron spin concentration, T_{2e} , and

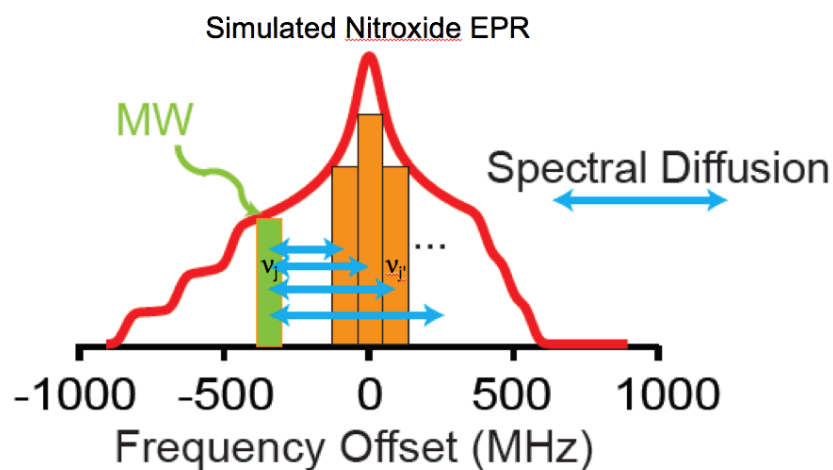


Figure 18. Cartoon representation of ELDOR simulation method, where the spectral diffusion rate is calculated between different frequency bins across the EPR line. The frequency bins in width must be less than the homogenous EPR line width.

T_{1e} of the radical species, but does not take into account the hyperfine coupling to nuclei, therefore the solid effect transitions are not simulated. The T_{1e} affects the depth of the simulated peaks- longer T_{1e} leads to a greater depth in the observed peaks, but the simulations do not take into account the varying T_{1e} across the EPR line which has been

observed in inhomogenously broadened EPR spectra at high fields.^[123] Longer T_{1e} values are observed at lower microwave frequency and shorter T_{1e} values are observed at higher microwave frequency. When the electron spin echo is detected at higher microwave frequency the simulated lambda values will be lower due to the shorter T_{1e} than at the

central EPR transition, while at lower microwave frequency the simulated λ^{eSD} value will be an overestimate due to the longer T_{1e} than at the central EPR transition as demonstrated in Figure 19. The error for these simulations was determined by calculating the % error from the residuals of the simulated ELDOR spectrum when compared to the measured spectrum.

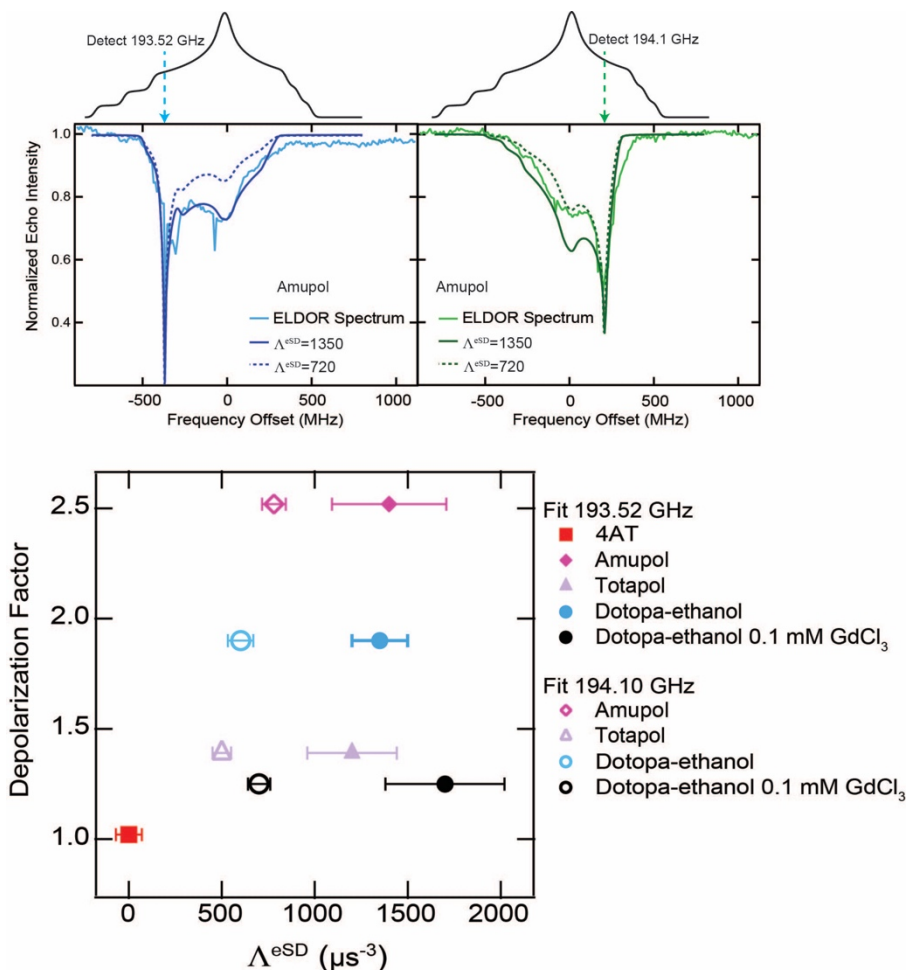


Figure 19. Top 10 mM Amupol ELDOR spectra detected at 193.52 GHz (Blue) and 194.1 GHz (green). Simulations are shown for a Λ^{eSD} of 1350 (solid line) and 720 dashed line. The Λ^{eSD} of 1350 appears to be an over estimation for the high frequency detection side due to the varying T_{1e} across the EPR line. (Bottom) The Λ^{eSD} for both the high and low detection frequencies plotted against the depolarization factor.

While this method will not provide an exact Λ^{eSD} value, a qualitative trend of the effective spectral diffusion rate of each radical solution compared to each other and how this affects depolarization can be derived. Figure 19 (bottom) shows a plot of the lambda value vs. the depolarization factor for all radicals measured. The lambda values for the bi and tri-radical

species are the same, while the mono-radical 4-amino TEMPO showed no spectral diffusion. This is interesting for two reasons: first, it shows that the spectral diffusion rate is similar for all radical species and therefore does not have an effect on the differing depolarization factor measured for each frozen radical solution. Second, the difference in the depth of the broad peak in the ELDOR spectrum is due to differing T_{1e} , i.e. the spectral diffusion rate as shown by λ , but the time in which the spins are allowed to diffuse, as determined by T_{1e} , is what determines the peak depth of the ELDOR spectrum. The lack of observable spectral diffusion on the mono radical implies that intra radical interactions between the two or three nitroxide spins in the molecule must be present for spectral diffusion at 20 mM spin concentration.

D. Conclusion

In this study, we have shown that nuclear depolarization can cause an inflated $\epsilon_{MWon/off}$ by 60 % for bi- and tri- nitroxide radicals at 20 mM spin concentration, while the mono-radical nitroxide demonstrated no significant depolarization. The nuclear depolarization effect is due to an equalization of the electron spin polarization across the EPR line under MAS and the extent of this depolarization is strongly correlated to the T_{1e} of the nitroxide radical. Furthermore, the addition of a T_{1e} relaxing agent such as Gd^{3+} to the nitroxide spin system correspondently reduces the nuclear depolarization effect. Finally, at 20 mM electron spin concentration the pseudo spectral diffusion rate constants for the bi-, and tri- nitroxide radicals measured were all within error of each other, while the mono radical showed no spectral diffusion. Therefore, the differing depolarization factor in the various mono-, bi- and tri- nitroxide radicals is due to the variance in T_{1e} , not spectral diffusion across the EPR

line. The lack of spectral diffusion observed at 20 mM spin concentration of the mono-radical nitroxide leads one to ask the question: does electron spectral diffusion need to be present in the spin system in order to observe the nuclear depolarization effect? This will be the subject of future studies where the spectral diffusion and depolarization factor of a concentration series of the mono-radical and the bi-radical amupol will be compared.

IV. Optimizing Microwave Transmission Through a Custom 20 K DNP

MAS Probe

A. Introduction

The method of solid state DNP is used to increase overall polarization of the target nuclei, typically by transferring polarization first to ^1H nuclei and then using cross-polarization to the nuclei of interest such as ^{13}C or ^{27}Al . Because of this, many cryogenic helium DNP systems have been developed that can operate at temperatures less than 30 K.^[79,95] Our desire for maximum nuclear polarization has led to a collaboration with Revolution NMR LLC and Bruker Biospin. to modify a cryo MAS DNP probe operational at a spinning rate of 8 kHz and a temperature of 20 K for DNP. This modification consists of the addition of a Thomas Keating waveguide for coupling the fundamental Gaussian mode from free space to the sample in the probe. In an ideal system, the waveguide would extent right up to the sample, but in an MAS probe the microwaves are propagated through the stator, coil, and rotor. These materials can add significant additional loss of microwaves to the sample if these components are not properly optimized for microwave transmission. The microwave loss to the sample is of specific importance with our 140 mW microwave power source, where a loss of 1 dB to the sample results in a 20 % power loss. One advantage of the Revolution NMR MAS probe is the modular design- the end of the microwave waveguide, the coil, and the rotor material can all be easily altered without taking apart the entire MAS stator. This versatility has allowed us to determine the microwave loss to the sample through each component in the standard Revolution MAS DNP probe design. Here we present an improved design to the Revolution DNP/NMR MAS probe which increases the microwave magnetic field (H) at the sample position and the DNP enhancement factor

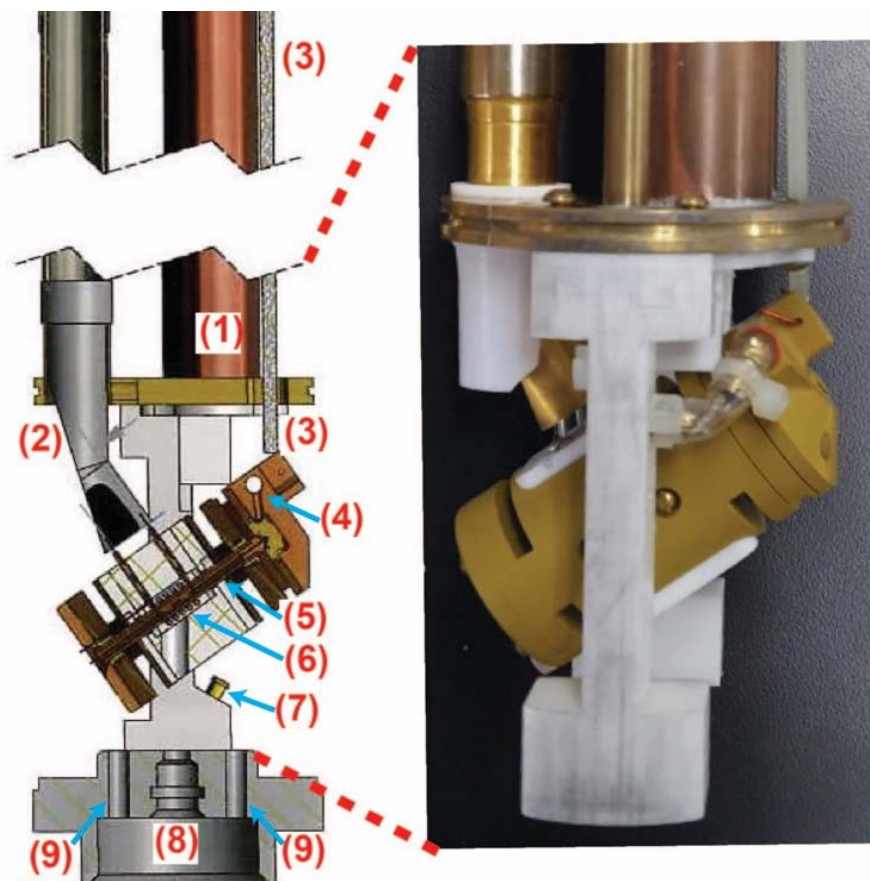


Figure 20. Schematic drawing of Revolution NMR LLC. cryo MAS DNP probe. (1) Radio frequency transmission line, (2) microwave waveguide, (3) Magic angle alignment rod, (4) drive N₂ gas inlet, (5) sample rotor, (6) NMR solenoid coil, (7) bearing N₂ gas inlet, (8) Liquid Helium inlet, and (9) gas exhaust port. The right shows a picture of the built probe.

obtained at 20 K. This improvement was achieved through a combination of simulations of the microwave field inside the probe, bench top power measurements, and DNP enhancement measurements comparing the standard Revolution NMR probe design with the improved design.

B. Details of the Revolution NMR Cryo MAS probe

The Revolution NMR cryo temperature MAS DNP/NMR probe is based off the low temperature probe design by Thurber and Tycko.^[124,125] A schematic of the probe is shown

in Figure 20. This is a double resonance transmission line probe with one channel fixed to be resonant at the ^1H Larmor frequency and the second channel tunable over 15 MHz to 290 MHz. The MAS stator is designed for a 4 mm rotor with pressurized nitrogen gas used for the bearing and drive of the rotor. Pressurized nitrogen gas is taken from a nitrogen dewar and directed through a flow controller where the pressure of the bearing and drive are manually set. The drive also passes through an electronic valve that can be controlled via a PID controller interfaced with TopSpin. The nitrogen gas is not pre-cooled before being sent to the bearing and drive of the rotor. Liquid helium is used to cool the sample in the center of the rotor, and the cold helium is directed over the sample space while the drive and bearing are at the ends of the rotor. Another purge gas line flows nitrogen gas down the length of the probe inside and out to prevent ice formation. The exhaust gas is a mixture of the room temperature nitrogen and cold helium gases. Spinning with nitrogen gas and cooling with helium at 20 K requires that a temperature gradient of at least ~ 60 K must be maintained from center of the sample to the drive tip of the rotor. This gradient is maintained by the design of the rotor, shown in Figure 21. The rotor is 45.7 mm long and the sample space is 10.2 mm long (0.044 mL volume) with Teflon spacers on either end to center the sample in the rotor. Due to the large temperature gradient, an accurate reading of the sample temperature is not trivial. This is achieved through the addition of the salt KBr to the samples in order to monitor the ^{79}Br nuclear spin-lattice relaxation time (T_{1n}) which has been shown to provide accurate temperature measurements below 90 K.^[124] The temperature calibration for our probe was empirically determined- the calibration method and temperature stability of the probe are shown in Appendix D.

The microwaves are first coupled to a Thomas Keating Ltd. waveguide which is shown in Figure 20. At the end of this waveguide is a miter bend which is designed to have the microwave H field perpendicular to the radio frequency B1 field from the solenoid coil. This

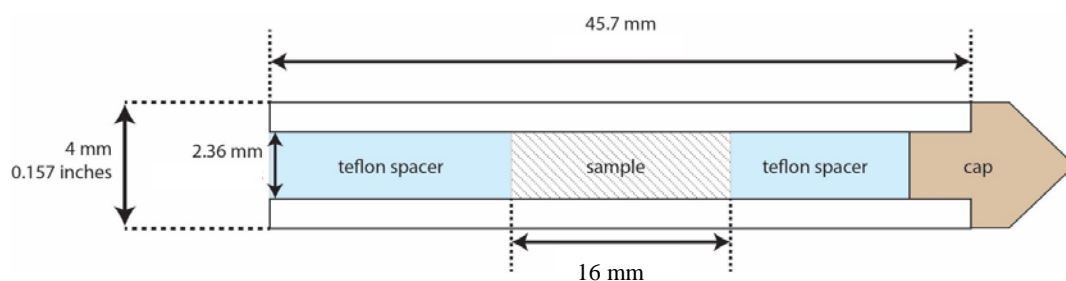


Figure 21. MAS rotor design. The rotor material is Zirconia but can be modified to sapphire. Teflon spacers are used to center the sample such that it sits inside the coil area.

method is known as the radial waveguide method. With a radial waveguide the microwaves propagate through the copper solenoid coil, and a portion of the microwave beam is reflected away from the sample. Another irradiation method that has been proposed is an axial irradiation, as shown in Figure 22. This method irradiates along the axis of the rotor, where the microwave H field is now parallel to the coil radio frequency field. This method avoids the metallic coil, preserving the Gaussian microwave beam. We seek to use our bench top testing to compare the radial and axial method of microwave irradiation.

Next in the microwave beam path is the solenoid coil. Any microwave expert would cringe at the sight of a metallic structure in the path of a Gaussian microwave beam. The microwaves are reflected by the metallic turns of the coil, distorting the Gaussian beam shape. Therefore the space from center to center of the turns of the solenoid coil, pitch, and wire diameter can be optimized for maximum microwave transmission. It is common in

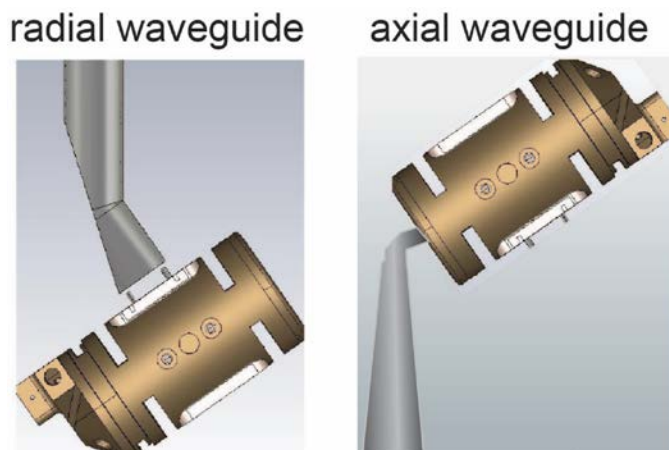


Figure 22. (Left) radial waveguide configuration, the microwaves are propagated perpendicular to the NMR coil. (Right) Axial waveguide, the microwaves are propagated parallel to the coil and are not distorted by interactions with the NMR coil

commercial systems to have a stretched pitched solenoid coil, with a wide center pitch and narrow outer pitch, but designs for a constant pitch coil have been shown to improve the field and microwave distribution over the sample space.^[126] Finally, before reaching the sample the microwaves must travel through the MAS rotor. The dielectric constant of the rotor determines the microwave absorbance by the rotor wall. Zirconia has been commonly used for MAS rotors, but has a high dielectric constant of 21, which means it strongly absorbs microwaves at ~200 GHz leading to a large loss in microwaves to the sample. Sapphire is commonly used for DNP probes because it has a relatively small dielectric constant of 9, however machining a rotor with the correct length to fit in our MAS stator is not trivial. Nevertheless, we have been able to spin at 90 K with a sapphire rotor.

C. Simulation and Experimental Methods

Computer Simulation Technology (CST) Microwave Simulations

To determine the relative microwave field and transmitted power in the various coil types and rotor materials, simulations were performed using the software Computer Simulation Technology (CST), using the FIT time domain (Finite Integration Technique). An AutoCAD drawing of the probe was used to recreate the probe structure. A Gaussian beam point source at 194 GHz was placed at the exit of the waveguide in order to approximate the microwave beam output of the waveguide. The Gaussian beam is 17.3 mm away from the center of the coil to match the distance between the waveguide end and the sample center. The beam waist of the miter bend in the waveguide is known to be 2.5 mm in width at 12.5 mm away from its point of origin. The Gaussian beam emits a square pulse and the calculation was carried out until the total energy of the system decayed to -30 dB relative to its maximum value. The boundary conditions were set so that the boundaries acted as perfect absorbers and all energy passing the boundaries was lost. The coil was made of copper and other materials in the stator, such as the Teflon coil platform and the rotor, were not included in this set of simulations. The average microwave magnetic field was calculated as the magnitude of the average B_1 field over the sample position within the coil, shown in Figure 23. In the next stage of simulations, the rotor material was taken into account through the dielectric constant of the rotor material, $\epsilon_R = 21$ for Zirconia and $\epsilon_R = 9$ for Sapphire. The sample dielectric constant was set to $\epsilon_R = 1$, and the average B_1 field was measured in the same positions as in the coil simulations. These simulations were carried out by a combination of both the Han lab and Bruker Biospin.

Bench-Top Power Measurements

The modular Revolution NMR probe affords for the measurement of the microwave transmission loss through every component along the microwave beam path, i.e. the quasi-optics, waveguide, coil, and rotor. A bench-top method was developed which employed a Thomas-Keating power meter to directly measure the mW of microwave power through each component of the MAS DNP system. In order to set up an accurate microwave bench top station, we first copy the design of the QO MAS DNP circuit as shown in Figure 23a. This design uses a pair of elliptical focusing mirrors to couple the Gaussian microwave beam to the waveguide. An isolator is used to protect the microwave source from damage caused by reflections back to the multiplier chain, as described in Chapter 2.A. A picture of the actual MAS DNP QO structure coupled to the probe is shown in Figure 23c. The benchtop testing station is setup such that the waveguide, coil, and rotor can be mounted at the same position from the last elliptical mirror as when mounted in the probe. From here the microwave power before and after each component was measured and the power loss in dB was determined.

NMR/DNP Measurement

10 mM of the nitroxide bi-radical AMuPol (electron spin concentration = 20 mM) dissolved in 60:30:10 d_8 -glycerol:D₂O:H₂O solvent was mixed with 65 mg of KBr (company, grain size) and was placed in the rotor and 20 mg of the radical solution was added. The KBr and amupol solution were gently mixed inside the rotor so the KBr was wet with the radical solution but the grains did not dissolve completely. The 4 mm rotor was then placed inside the MAS stator and the sample was cooled to 24 K while spinning at 4 kHz. The probe was placed in the bore of a Bruker 300 MHz wide bore magnet and connected to a Bruker Avance solid state NMR spectrometer. During the sample cooling the

temperature was monitored by the recording the $T_{1\rho}$ of ^{79}Br . Once the sample was at the desired temperature the ^{79}Br was monitored before and after the experiment and the average temperature calculated. The ^1H NMR signal was measured with a saturation recovery solid echo pulse sequence, and the DNP enhancement determined as the ratio of the NMR signal with microwave irradiation at the maximum DNP enhancement frequency (193.65 GHz) divided by the NMR signal without microwave irradiation.

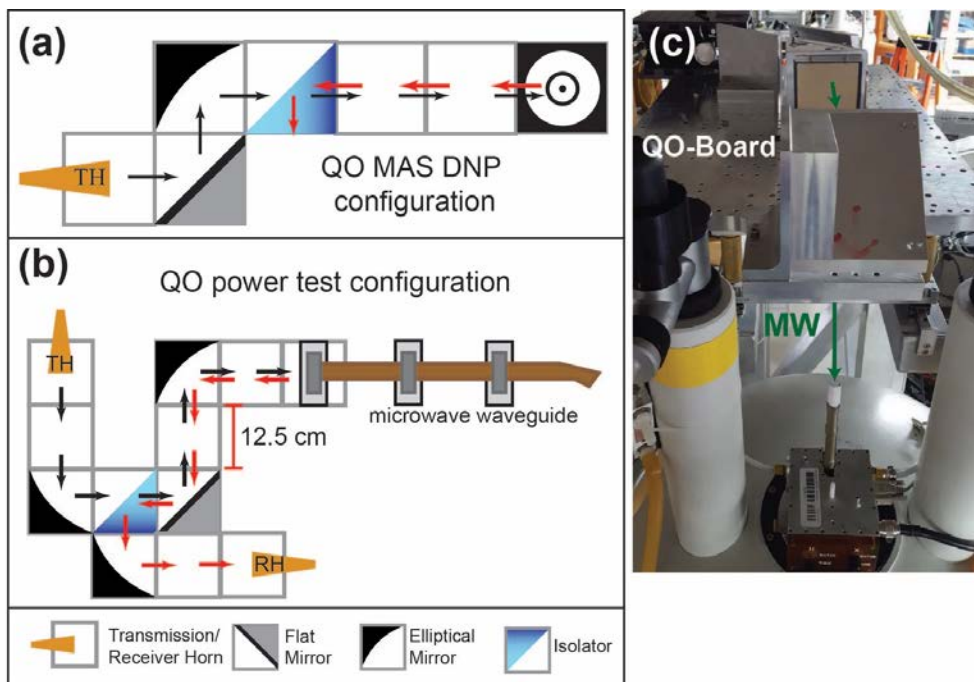


Figure 23. (a) Quasi-Optical configuration. Two parabolic focusing mirrors couple the microwaves to the MAS probe waveguide (black arrows), and the reflected microwaves are directed to an absorber to protect the microwave source from damage (red arrows). Each square is 12.5 cm. (b) The microwave benchtop testing station mounts the waveguide the same distance as in (a), the microwave power is measured with a Thomas Keating Power meter. (c) Picture of the QO MAS DNP microwave bridge and probe in the 300 MHz Bruker magnet. The microwaves (green arrow) are coupled to the waveguide extending from the probe.

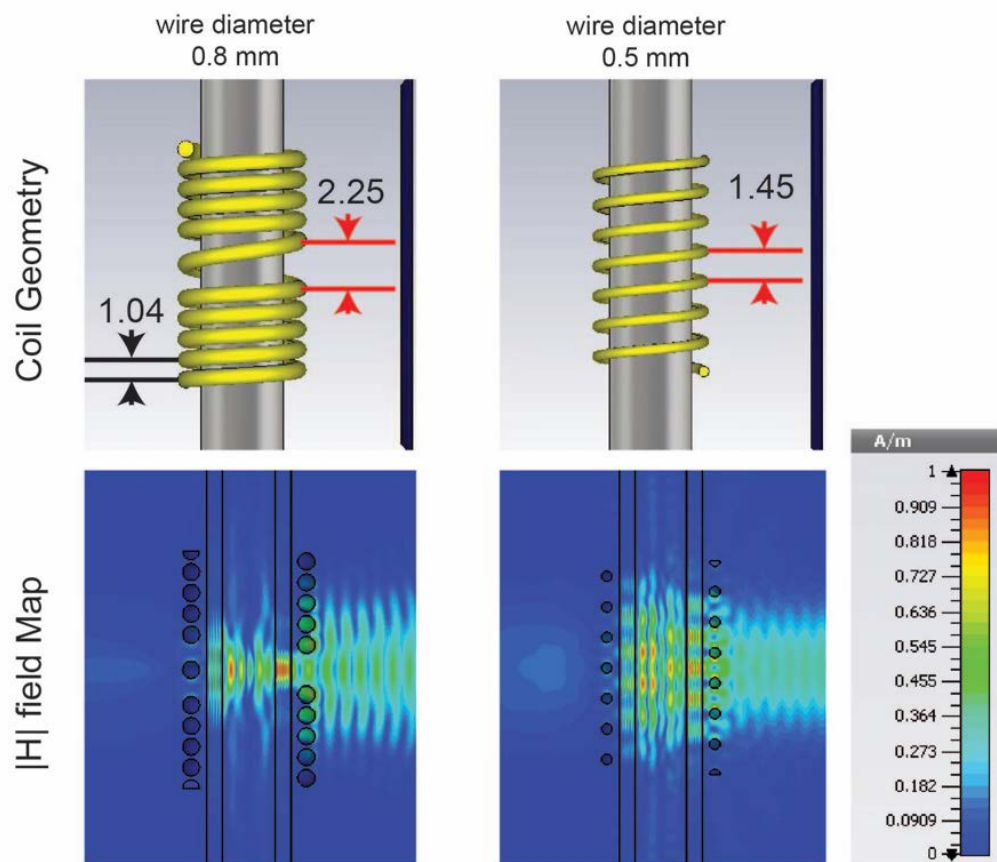


Figure 24. (Left) The coil geometry and H-field map of the standard revolution NMR split pitch coil. The microwaves only penetrate the center gap of the coil, leaving a large portion of the sample unirradiated with microwaves. (Right) The constant pitch coil with 0.5 mm wire allows the microwaves to more evenly irradiate the sample. The simulations presented here were performed by Armin Porea at Bruker Biospin.

D. Results and Discussion

Microwave Power loss trough typical MAS DNP probe architecture

The most common DNP probe architecture that can be found in commercial probes involves coupling the output of the microwave source into a corrugated waveguide with a miter bend directing the microwaves along the axis perpendicular to the NMR coil. A stretched NMR solenoid coil is employed in most DNP NMR probes, where the center pitch of the solenoid is larger than the outer pitch. This commercial MAS DNP setup is shown in

figure 22 with the specific dimensions for the commercial configuration of the Revolution NMR MAS DNP probe. Before we begin to optimize the structure of each component we first need to characterize the microwave power through the commercial Revolution NMR system. This will be done with a three-prong approach of bench top power loss, CST simulations, and DNP enhancement measurements.

The first part of our three prong approach is to use CST calculation to determine the optimal coil geometry to achieve the largest microwave H field at the sample position. The stretched pitch coil is a 10 turn coil with a center pitch of 2.25 mm and sounding pitch of 1.04 mm and a wire diameter of 0.8 mm. To optimize the coil it has been proposed that a constant pitch coil can more homogeneously distribute the microwave field over the whole sample.^[127] Therefore a simulation was performed in order to find the optimum wire diameter and coil pitch in order to optimize microwave transmission through the coil. The results from these simulations are shown in Figure 24, where optimal wire diameter was found to be 0.5 mm and the optimal pitch was found to be 1.45 mm. The H field distribution in the two coils was compared, in these simulations the H field was normalized to the same maximum H field. From this we can see while the maximum field amplitude is similar in both coils, the constant pitch coil has a more uniform distribution. In this initial simulation the rotor material dielectric constant was set to an $\epsilon_r=1$.

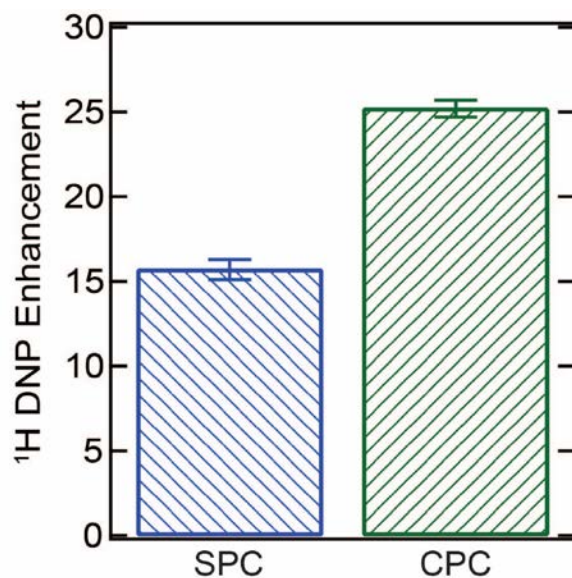


Figure 25. ^1H DNP enhancement of using the split pitch NMR coil (SPC) and the constant pitch NMR coil (CPC). These measurements were done at an average temperature of 24 K and spin rate of 4 kHz, using a solid echo recovery pulse sequence with a 30 s DNP build up time.

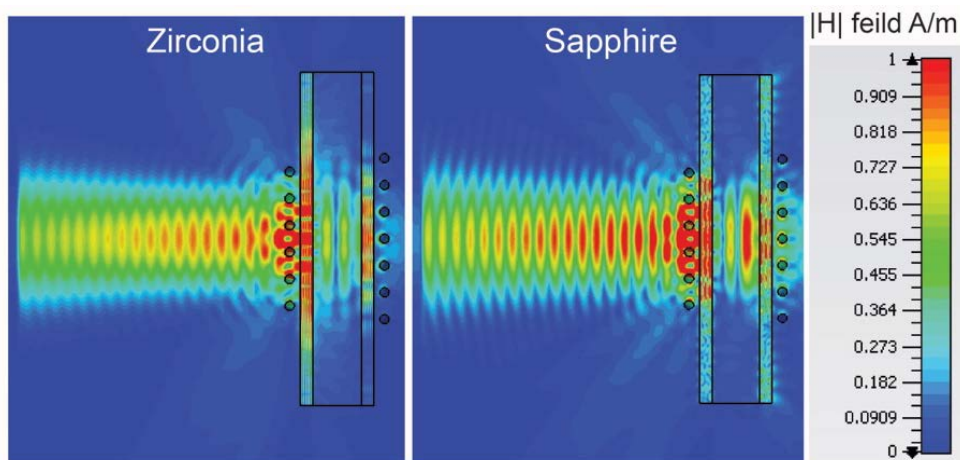


Figure 26. H field simulations of Gaussian beam propagation through a zirconia and sapphire rotor with the constant pitch coil. The maximum H field intensity is greater with the sapphire rotor.

This was also confirmed with measurements of transmitted loss using the microwave testing station. We found that a constant pitch coil gave 1.5 dB loss while the stretched pitch coil yielded 1.9 dB microwave loss. This is not such a drastic difference in overall

field intensity but the microwaves can penetrate the sample evenly in the split pitch coil leading to a greater DNP enhancement. The DNP enhancement with stretched pitch and constant pitch coils were measured at 24 K and 4 kHz spin rate, as shown in Figure 25. When a sample of 10 mM amupol in 60%:30%:10% D₈-glycerol:D₂O:H₂O was placed in the rotor with the split pitch coil a 1H enhancement of 16 was recorded, while the constant pitch coil increased the measured DNP enhancement to ~25.

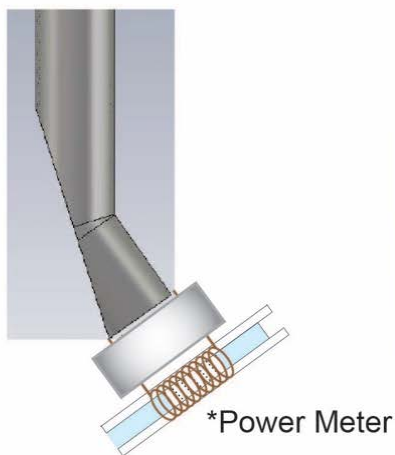
With the coil now optimized as a constant pitch coil we turn now to the rotor material. Zirconia has a high dielectric constant causing large microwave loss due to rotor adsorption. Sapphire has a much lower dielectric constant and it is common practice to use this type of rotor in commercial MAS DNP systems. Figure 26 shows simulations of the microwave field for Zirconia and Sapphire rotors. The sapphire rotor shows a 33% greater microwave

Table 2. Transmission power loss through each component of the probe from the quasi-optics to the sample space. In the axial position the loss through the coil is negligible because the coil does not interfere with microwave beam path.

	Radial Waveguide Configuration	Axial Waveguide Configuration
Quasi-Optics	1.8 dB	1.8 dB
Waveguide	1.2 dB	2.4 dB
Zirconia Rotor	1.8 dB	5.4 dB
Sapphire Rotor	1.5 dB	--
Split Pitch Coil (SPC)	1.9 dB	--
Constant Pitch Coil (CPC)	1.9 dB	--

field in the sample space than the Zirconia rotor. From the simulations it seems that the sapphire rotor would be the better material for microwave transmission through the walls of

Radial Configuration



Axial Configuration

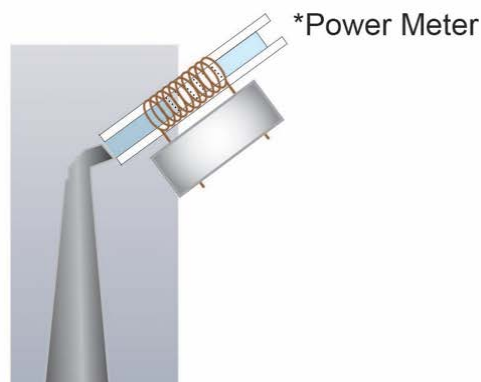


Figure 27. Power testing setup for radial and axial configuration. The Thomas Keating power meter was used to measure the mW of microwave power.

the rotor, but sapphire has much lower thermal conductivity than Zirconia and making the temperature gradient that must be maintained between the sample space and the bearing and drive gas difficult to maintain below 90 K.

From our starting 140 mW of microwave power, the loss through the MAS QO bridge was 1.8 dB due to the Faraday rotor in the isolator system. When the power meter was placed 17 mm away from the waveguide, which is the distance from the waveguide to the center of the sample, there was an additional 1.2 dB power loss. When the Teflon coil platform and copper coil were added to the system the loss behind the coil was 2.4 dB. Finally, when the zirconia rotor was added the additional loss at the power meter position is 1.9 dB. This brings the total microwave loss behind the coil to 6.7 dB for the standard Revolution NMR setup, which means we start out with 140 mW and drop to 42 mW at the

sample position. The microwave loss was measured behind the coil and rotor due to the space constraints of the Thomas Keating power meter we cannot measure the microwaves inside the coil and rotor at the sample position. The microwave power inside the rotor can be approximated from assuming the loss through the rotor and coil at the sample position is half of that measured behind the rotor and coil. This gives a microwave power of 42 mW at the sample position, corresponding to a 70% loss in microwave power, with the largest loss coming from the coil and rotor. The microwave loss from the coil is due to reflections of the microwaves off the copper coil, as the coil platform itself is Teflon which is transparent to microwaves at 200 GHz. The loss from the rotor stems from the high real part of the dielectric constant of Zirconia $\epsilon_R=21$, so the loss in microwaves is due to absorption of the rotor material itself.

With this microwave testing station we also examined another method of irradiating the sample with microwaves, axial waveguide irradiation, as shown in Figure 26, where the microwaves are propagated along the axis of the rotor, avoiding the NMR coil. This method of irradiation has yet to be tested in a real system. Our modular system allows us to swap out the end of the waveguide for axial or radial irradiation and compare the measured microwave loss through each waveguide. Table 1 summarizes the measured loss for the axial and radial configuration. Here the axial waveguide yielded a high loss of 2.4 dB. Including the microwave loss in the QO bridge and along the long axis of the zirconia rotor, the total loss is 9.6 dB, and again the power was measured at the end of the rotor so if one assumes the loss at the sample position will be half of that measured, the microwave power at the sample position is ~ 5 mW (96 % loss in power). The loss in this system is much larger than the commercial configuration due to the path length the microwaves must travel

after exiting the waveguide. The output diameter of the horn is 4 mm and the beam is rapidly divergent coming out of the waveguide which causes a significantly lower microwave power at the sample position. Further developments are required to focus the axial microwave beam such as optimizing the size of the waveguide exit to keep the beam waist smaller than the rotor or using a lens to refocus the microwaves, these optimizations will be the subject of future studies. For now, we have decided to keep the current commercial configuration for the waveguide (radial waveguide).

E. Conclusion

With DNP measurements and simulations we were able to confirm that for our configuration, radial microwave irradiation with a constant pitch coil and sapphire rotor give the lowest microwave loss of microwaves to the sample. This can be further optimized by designing a mirror to place after the coil to reflect the transmitted microwaves back into the sample which will increase the B_1 field by a factor of 2. However the temperature gradient across the sapphire rotor is difficult to maintain and therefore measurement of temperature below 90 K is not possible. This reflection of the microwaves will also make EPR detection possible, additionally a lens could be added to the waveguide in order to

V. Resolving TEMPO and ^{27}Al interaction with Direct DNP and EPR in Al-SBA-15

A. Introduction

Mesoporous alumina-silica materials have great industrial potential to facilitate acid catalyzed reactions such as dehydration–condensation, alkylation, and isomerization processes.^[6,128,129] These mesostructured materials have attracted interest due to their high surface area and large pore sizes (10-100 nm) to host polymers and other bulky reactants.^[130,131] Solid-state NMR (ssNMR) spectroscopy in combination with magic angle spinning (MAS) is already an important tool for elucidating the atomic-level structure of heterogeneous porous material, including alumina-silicates such as Al-SBA-15.^[132,133] However, the inherently low signal sensitivity of NMR makes it exceptionally difficult to selectively examine surface species, especially the catalytically active aluminum centers that are even more dilute than the surface matrix species. This is all complicated by the spectral broadening of the aluminum spins that arise from the quadrupolar interaction, $S=5/2$ for ^{27}Al , that can reduce the NMR signal of surface aluminum species to an undetectable limit.^[134] Griffin and co-workers' development of dynamic nuclear polarization (DNP) at high magnetic fields under MAS and liquid nitrogen temperatures achieved up to two orders of magnitude of signal enhancement, i.e. shortening the acquisition time of ssNMR spectra by up to four orders of magnitude.^[7] This method of enhancing NMR signal has been shown to be one of the most effective NMR methods for obtaining surface enhanced NMR spectra.^[11]

Recently, DNP methods have been applied in order to obtain surface enhanced NMR spectra of aluminum containing catalytic material, such as γ -alumina,^[12,20] as well as mesoporous alumina and aluminum containing metal organic frameworks (MOFs).^[115,116] The majority of this work utilizes cross polarization (CP) from ^1H to ^{27}Al in conjunction with MAS. This “indirect” method of hyperpolarizing ^{27}Al via the frozen solvent with designer bi-radicals, e.g. TOTAPOL and bTbk, has been shown to yield ^{27}Al signal enhancement factors of 15-20. However, if the objective is to account for surface ^{27}Al species with specific affinity for a paramagnetic labeled reactant, the detection of solvent ^1H accessible ^{27}Al species, as captured with CP-DNP, may be of limited interest. This study

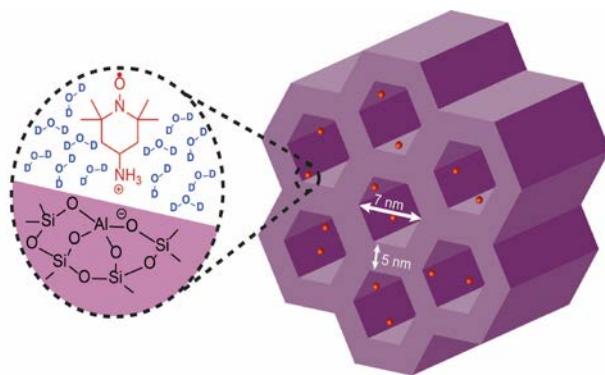


Figure 27. Schematic representation of Al-SBA-15 (Si/Al~20) with 4-amino TEMPO imbibed into the pores. The positive charge on the amine group is electrostatically attracted to the negatively charged Al(IV) acid site on the surface of the material.

tests an alternative approach of direct DNP polarization of ^{27}Al via dipolar coupled electron spin probes that are mono-nitroxide-based radical spin probes. By relying on the electron spin of these probes dipolar coupled to the ^{27}Al nuclei, the direct DNP signal enhancement will be weighted towards the aluminum sites in spatial proximity of the mono-radical spin probes. The information gained from direct DNP is expected to be complementary to ^1H -

^{27}Al CP DNP. CP DNP will reflect an enhancement contrast of the solvent ^1H as induced by the different radical species. Thus, even with spatially distinctly located spin probes, efficient ^1H nuclear spin diffusion likely will dilute any difference in radical localization, in contrast to direct DNP of isolated nuclei. Differences in surface enhanced NMR of ^{29}Si species via direct vs indirect (CP) DNP have been observed by Lafon, *et. al.* in synthetic clay nanoparticle and porous silica samples using the bi-radical probe TOTAPOL.^[135,136]

Crucially, one can exploit differences in mono-radical probes employed for DNP in their selective partitioning or adsorption to the surface sites of interest directed by the side group's size, charge, shape or chemical property. By exploiting instrumental and methodological advances, as described in previous studies^[35,97,137] of our home-built DNP NMR probe, this study reports on the observation of direct ^{27}Al DNP signal amplification of dilute Al sites, namely of Al-SBA-15. This material with a Si/Al=20 was chosen to demonstrate the feasibility of direct DNP to target ^{27}Al nuclei of interest using mono nitroxide radical probes. The sample is an excellent model system given the presence of two distinct aluminum sites, namely a tetrahedral coordinated (IV)Al and octahedral coordinated (VI)Al that can be resolved by ^{27}Al MAS NMR (no DNP) as shown in S.I Figure 2.

The target of this study is the direct DNP enhancement of surface exposed acid sites, associated with tetrahedral coordinated aluminum, Al(IV) in Al-SBA-15, that carry a negative charge (Figure 27). Here, we present a systematic study of direct ^{27}Al DNP enhancement of Al-SBA-15 by employing three different mono-radical probes of varying charge states. Under the sample impregnation condition used here with solution at neutral pH, 4-amino TEMPO (4-AT) is expected to be positively charged, and therefore electrostatically attracted to the Al(IV) site. The negatively charged 4-carboxy TEMPO (4-

CT) should be electrostatically repelled from the negatively charged Al(IV) site and silica surface, while the neutral and hydrophilic 4-hydroxy TEMPO (4-HT) would likely be inside the pores but not adsorbed to the Al(IV) site. This is a simplistic representation of the interactions between the spin probes and the surface of the Al-SBA-15 material as it neglects any interaction between the spin probes and the Si-OH surface groups that may have an effect on the local surface concentration of the spin probes. Testing the validity of the simple model of whether selective partitioning of differentially charged nitroxide radical probes to ^{27}Al surface sites can be achieved, and if so, elucidating the consequences for direct ^{27}Al DNP is the goal of this study. The hypothesis is that direct ^{27}Al DNP will be largely determined by the interaction of the spin probes with the surface aluminum sites and the local concentration around the aluminum sites. Besides static ^{27}Al DNP, 3-pulse ESEEM^[138] and X-band cw EPR analyses were performed on the various spin probes imbibed in Al-SBA-15 to determine the extent of adsorption, interaction strength and local concentration of the nitroxide probes to ^{27}Al surface sites.

B. Experimental Methods

Sample Preparation for DNP/NMR and EPR measurements. The synthesis of the Al-SBA-15 mesoporous material followed the direct synthesis reported by Li *et al.*^[139] The synthesis and characterization of the Al-SBA-15 are detailed in the supporting information, including a 1-D ^{27}Al MAS NMR spectrum acquired at 7 T to demonstrate the presence of both the (IV)Al and the (VI)Al sites in the material (S.I. Figure 2). Samples for DNP/NMR and EPR measurements were prepared with various nitroxide radicals; 4-amino TEMPO (4-AT), 4-carboxy TEMPO (4-CT), and 4-hydroxy TEMPO (4-HT), are imbibed via the incipient wetness method, as described by Emsley and co-workers.^[13] The imbibed radical

solution was prepared by making a 10 mM solution of the nitroxide radical in either H₂O or D₂O as the solvent. For the incipient wetness method, 60 μ L of radical solution was pipetted onto 20 mg of Al-SBA-15. The radical solution and Al-SBA-15 material were stirred until a wet powder was formed.

Static DNP/NMR Instrument and Measurements. For DNP/NMR measurements the wet Al-SBA-15 powder was transferred to a Teflon sample cup and placed in a home-built NMR probe with a 1-loop saddle coil to resonate at 78.2 MHz. The probe was placed inside a custom Janis STVP-NMR cryostat, operating in continuous flow mode. The necessary components for 200 GHz DNP have been described in a previous publication.^[97] Most importantly a tunable 200 GHz solid state microwave source (VDI) with a frequency range of 193-201 GHz and a power output of 70 mW was used in conjunction with a low loss quasi-optic bridge (\sim 1dB) to couple the microwave to the corrugated waveguide of the NMR/DNP probe. The NMR/DNP signal is measured in the bore of a Bruker Biospin 7 T superconducting magnet with a 300 Avance solution state spectrometer. All DNP/NMR measurements were performed at a temperature of 4 K. The temperature was monitored to be stable within \pm 0.1 K for all ²⁷Al DNP NMR measurements. DNP measurements were performed with the use of a saturation recovery solid echo pulse sequence (S.I. Figure 3) while continuously irradiating with microwaves to obtain the DNP enhanced ²⁷Al signal, or without microwaves to obtain the unenhanced ²⁷Al NMR signal. The ²⁷Al signal enhancement factor (ϵ) was calculated by the ratio of $\epsilon = S_{\text{DNP}}/S_{\text{NMR}}$, where S_{DNP} is the ²⁷Al signal area while continuously irradiating with microwaves and S_{NMR} is the signal area in the absence of microwaves. All DNP/NMR measurements were taken with a recovery delay time of 60 s. A 60 s recovery time is dramatically shorter than the full build up time of ²⁷Al

NMR signal, which can be on the order of hundreds of seconds at 4 K, but detectable signal enhancement is observed already at 60 s recovery time. The DNP enhancement profiles were recorded by measuring the ^{27}Al enhancement as the microwave frequency was stepped from 197 to 199 GHz.

ESEEM Instrument and Measurements. The Al-SBA-15 samples were prepared for ESEEM measurements in the same manner as described above; a 1 mM radical concentration was used in the imbibed solution with H_2O as a solvent. A lower spin probe concentration was used for the ESEEM measurements to ensure that the decay of the electron echo, which decays with T_1 of the electron, was long enough to observe modulations of the echo decay. In contrast to DNP measurements, a protonated instead of deuterated solvent must be used for the ESEEM measurements as the modulation frequency of the electron echo decay from deuterium has a similar frequency (2.3 MHz) as Si (2.8 MHz) and Al (3.6 MHz), so that D_2O would obscure the modulations due to the Si and Al in the Al-SBA-15 matrix. All ESEEM experiments were measured at 50 K at 0.35 T with a MS3 resonator on an Eleksys E580 pulsed EPR spectrometer at 9.2 GHz. A 3-pulse ESEEM experiment was used (S.I. Figure 6) with a ($\tau = 140$ ns) time selected to optimize the ^{27}Al modulation, and the $\pi/2$ pulse was optimized at 16 ns. The peak echo intensity was measured as the variable delay was increased starting at 40 ns and increased in steps of 32 ns. Plotting the echo intensity as a function of variable delay yields a decay that is modulated by the Larmor frequencies of the nuclei coupled to the electron. A representative ESEEM trace is shown in S.I. Figure 6. All ESEEM traces were processed in the same manner; the background decay was fit to a 9th order polynomial and subtracted out and normalized by the

polynomial decay. A sin bell window was applied and the real FFT was taken to yield the ESEEM spectrum.

cw EPR Instrument and Measurements. All 9.5 GHz cw EPR measurements were performed at room temperature. The Al-SBA-15 sample with imbibed radical was prepared in the same method as described above. The sample was then placed in a quartz tube and in the center of a dielectric microwave resonator (Bruker ER-4123D). The cw spectra were measured with a Bruker EMX spectrometer at 0.35 T and 9.5 GHz EPR.

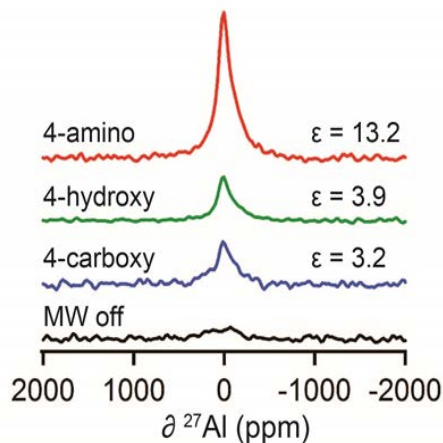


Figure 28. ^{27}Al Direct DNP spectra of Al-SBA-15 imbibed with various 10 mM mono nitroxides spin probe solutions using D_2O as the solvent. The DNP enhanced spectra were measured with irradiation at a microwave frequency where the maximum positive enhancement occurs for each spin probe (197.7 GHz for 4-AT, 197.75 GHz for 4-HT and 4-CT).

C. Results and Discussion

For direct DNP measurements, pure D_2O was chosen as a solvent to suppress polarization transfer and leakage via ^1H nuclear spin diffusion in H_2O . The use of D_2O as a solvent was found to nearly double the ^{27}Al enhancement factors compared to in H_2O solvent (see Appendix D) This is consistent with observations in the literature, where deuteration of solvent and ^1H on protein samples were found to increase the direct ^{13}C DNP

enhancement when using a mono- and bi-tempo radical derivatives.^[140,141] Figure 28 compares the direct ^{27}Al DNP spectra obtained from a single scan with 4-AT, 4-CT, and 4-HT, which were found to be $\epsilon = 13.2$, $\epsilon = 3.2$, and $\epsilon = 3.9$ respectively. 4-AT was chosen as a spin probe that would likely target the active aluminum sites in Al-SBA-15 mediated by electrostatic attraction to the negatively charged Al(IV). Thus, the question to be addressed is whether the highest enhancements seen with 4-AT is due to the proximity, and by extension stronger dipolar coupling, between surface ^{27}Al species and adsorbed 4-AT. For this, experimental evidence for surface adsorption and ^{27}Al -electron proximity is needed and will be addressed in the following sections.

When employing nitroxide radicals as DNP polarizing agents, it has been shown that the width and detailed shape of the microwave frequency-dependent DNP enhancement profile contains key information about the DNP mechanism.^[63,142,143] When combined with quantum mechanically derived spin dynamics calculations, the % contribution of cross effect (CE) or solid effect (SE) DNP mechanism can be extracted, as well as the effect of EPR spectral diffusion simulated.^[94] However, even when measuring simply the frequency difference between the DNP maxima, Δ_{DNP} , one can extract whether a dominant CE, SE or mixed effect is at play. If the Δ_{DNP} equals twice the nuclear Larmor frequency, ω_n , likely the SE is dominant, although this is only unambiguous if ω_n exceeds the EPR spectral width.^[144] If Δ_{DNP} does not equal $2\omega_n$ and the DNP maxima lie within the EPR line, then the CE is likely the dominant mechanism. Here we do not discuss the thermal mixing (TM) mechanism based on the results of Hovav et. al.^[89] where it was observed that in mono-nitroxide frozen solutions under static conditions at similar concentrations and liquid helium

temperatures, the electron spin polarization distribution is not described with a cooled Zeeman spin temperature.

Figure 29 shows representative frequency profiles for the direct DNP enhancement of ^{27}Al when employing 4-AT and 4-CT. The shape of the DNP frequency profile, with

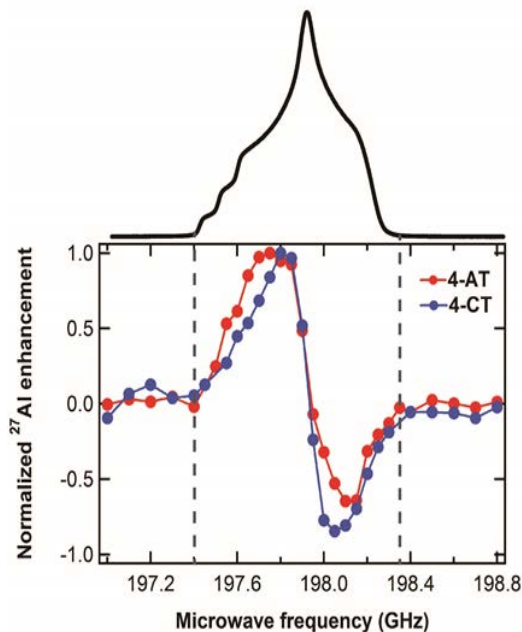


Figure 29. Shown are ^{27}Al DNP frequency profile of 4-AT and 4-CT imbibed in Al-SBA-15. 4-HT yielded a comparable frequency profile and peak to peak width as 4-CT. A representative nitroxide EPR spectrum is shown above, measured at 8.56 T as described in the supporting information. The dashed lines represent the edge of the EPR line, demonstrating that the DNP frequency profiles of 4-AT and 4-CT fall within the nitroxides EPR line.

positive signal enhancement at microwave frequencies below the central EPR transition, zero enhancement when the microwave frequency is at the central EPR transition, and negative signal enhancement at microwave frequencies larger than the EPR central transition, firmly establishes that the observed enhancements are caused by a DNP process and not by a decrease in relaxation time due to heating effects when the sample is irradiated with microwaves. The Δ_{DNP} of 4-AT is $350 \text{ MHz} \pm 50$, while the Δ_{DNP} of 4-CT and 4-HT is

$\sim 250 \pm 50$ MHz. The bumps visible in the baseline of 4-CT enhanced ^{27}Al spectrum at 197.2 GHz and 198.7 GHz are likely artifacts due to the low signal to noise ratio. Thus, all Δ_{DNP} values are much larger than 2 times ω_n of the ^{27}Al NMR Larmor frequency ($\omega_n = 78.2$ MHz at 7 T), while also falling within the nitroxide EPR spectral width, as explicitly measured and displayed above the DNP frequency profiles. The EPR absorption line was measured directly using a rapid passage method detailed in the supporting information. From this we conclude the DNP with all three mono-nitroxide probes dominantly proceeds via the CE mechanism. When comparing the DNP frequency profiles, it is clear that Δ_{DNP} is largest for 4-AT. Within the CE DNP mechanism, it has been shown recently that increasing the radical concentration broadens the DNP profile as measured by an increase in Δ_{DNP} due to stronger electron-electron dipolar coupling between proximal electron spins.^[143] The increased Δ_{DNP} of 4-AT can thus be attributed to an increased local spin concentration at the surface of the Al-SBA-15 relative to that of 4-CT or 4-HT, despite the same overall spin concentration of the 10 mM solution imbibed in each sample; suggesting that 4-AT does show an increased attraction to the surface of the Al-SBA-15 material as proposed.

In order to independently and directly test whether the 4-AT species is indeed closer specifically to surface ^{27}Al species than the other spin probes, 3-pulse ESEEM was used to directly measure the strength of the coupling of each spin probe to the ^{27}Al and ^{29}Si in the material (SI Figure 30 shows a three pulse ESEEM sequence). This pulsed EPR technique monitors the electron spin echo decay, whereby for 3-pulse ESEEM the echo decay is influenced by the T_1 of the electrons, as well as the spectral and spin diffusion of the electron spins. If (weak) anisotropic coupling between the electron spin and nearby nuclei is present, this echo decay is further modulated by the nuclear Larmor frequencies of the

proximal nuclei. A representative ESEEM echo decay for nitroxide spin probes imbibed in Al-SBA-15 is shown in SI Figure 4. In the case of weak hyperfine coupling, the modulation depth is dependent on the electron nuclear distance, the number of nuclei around the spin probe, and the nuclear spin type.^[145,146] When the modulation depth is large, it can be directly extracted from the ESEEM time trace.^[147,148] However in our case, when many nuclei are weakly interacting with the spin probes, the modulation depths of the ^{27}Al and ^{29}Si are shallow and cannot be directly extracted from the ESEEM time trace. Rather, we can compare the intensity of the ^{27}Al (I_{Al}) and ^{29}Si (I_{Si}) in the Fast Fourier Transform (FFT) of the ESEEM trace for each spin probe as a comparative measure of the modulation depth that will reflect on the strength of the electron nuclear interaction.^[149] Even though it is known that ^{27}Al can have a large quadrupolar interaction that affects the intensity of the ESEEM spectrum, it has been shown when comparing different spin probes in the same aluminum material system for weakly coupled aluminum nuclear spins that the quadrupolar interaction does not change when varying the spin probe type.^[145]

The ESEEM time traces were processed in a similar manner as described by Carmieli et al.,^[147] which is detailed in the S.I. Figure 4a and shows the ESEEM spectra for the different spin probes when imbedded in Al-SBA-15. The interactions of the spin probes with ^{29}Si and ^{27}Al in the Al-SBA-15 framework are shown by the peaks at 2.88 MHz and 3.66 MHz respectively. The peak at 14.04 MHz results from the spin probe's interaction with ^1H from largely the solvent. Figure 4b shows a plot of the I_{Al} and I_{Si} for each spin probe imbibed in Al-SBA-15. Information about the spin probes location on the overall surface of Al-SBA-15 can be inferred from the I_{Si} . We find I_{Si} is the largest for 4-AT out of all the spin probes, smaller for 4-HT, and yet smaller for 4-CT. This indicates that 4-AT yields a larger ^{29}Si

modulation depth and shows a stronger interaction with the surface silica than both 4-HT and 4-CT, where the strength of the interaction between the spin probes and the ^{29}Si species can be ranked 4-AT>4-HT>4-CT. Looking to figure out whether 4-AT is not only enriched at the silica surface, but also targets surface ^{27}Al sites, we turn to I_{Al} . Indeed, the I_{Al} is the largest for 4-AT out of all the spin probes while the I_{Al} of 4-HT and 4-CT is very similar with 4-HT. Thus from the ESEEM spectrum we can rank the interaction of the spin probes with surface ^{27}Al species as 4-AT>4-HT \approx 4-CT. This suggests that 4-AT does have the largest population localized on the surface of the material yielding a larger I_{Al} and I_{Si} than either of the other two radicals. Conversely, 4-CT has the smallest localized population on the surface of the material, suggested by the smallest I_{Al} and I_{Si} . This matches the ^{27}Al DNP enhancement trend, suggesting that the larger enhancement from 4-AT comes from a higher local surface concentration and accordingly a closer average proximity to ^{27}Al . Delineating between these two factors is nontrivial, however, clearly 4-AT show a significantly stronger interaction with the surface aluminum sites of Al-SBA-15 than the other two radicals. The latter is key because this implies that characterization of the surface aluminum sites accessible to a radical-labeled reactant molecule may be feasible in future work.

To directly demonstrate the physical adsorption of 4-AT to the surface of Al-SBA-15,

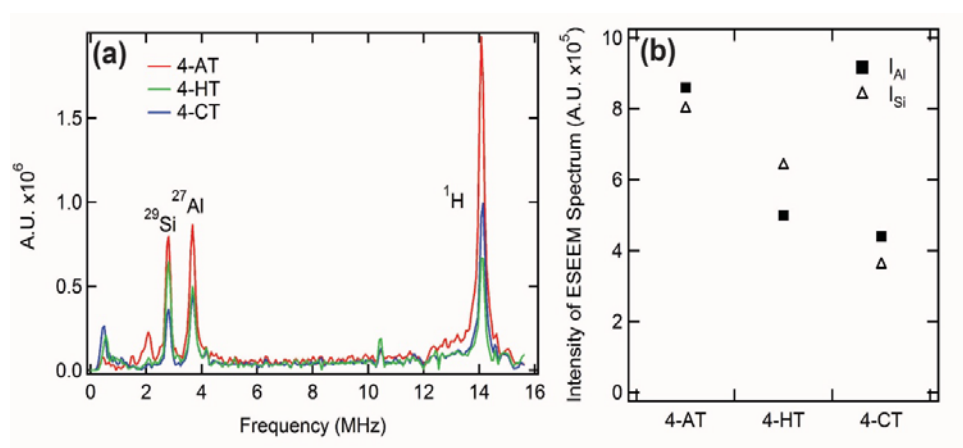


Figure 30. (a) The ESEEM spectrum for the various mono nitroxides radicals. The peak at close to zero frequency is an artefact that comes from the baseline correction process of the time domain ESEEM trace. (b) I_{Al} and I_{Si} for each nitroxide radical, due to similar linewidth between each radical, the peak height was taken as the measurement of intensity rather than the integral of the peak.

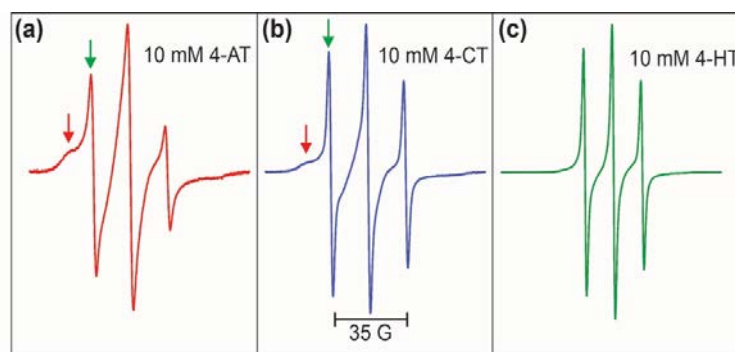


Figure 31. X-band CW EPR spectra of 10 mM (a) 4-AT, (b) 4-CT, and (c) 4-HT imbedded in Al-SBA-15. Two spin probe populations can be seen in 4-AT and 4-CT; immobile (red arrow) and mobile (green arrow) component.

cw EPR lineshape analysis was performed at 9.5 GHz and room temperature for all three radicals. Figure 4 shows a representative cw EPR spectrum of each spin probe imbedded in Al-SBA-15. In the EPR spectrum of 4-AT and 4-CT (Figure 31a, 31b) two populations are present: an immobile and mobile spectral component, represented by the intensities I_{imm} (red arrow) and I_{mob} (green arrow). The broad immobile component of the cw EPR spectra is attributed to spin probe adsorbed to the surface of Al-SBA-15, while the mobile component is attributed to spin probe tumbling freely in the pores of the material. When comparing the ratio of the $I_{\text{imm}}/I_{\text{mob}}$ it is clear that 4-AT has the largest proportion of its population adsorbed to the surface of the Al-SBA-15, with an $I_{\text{imm}}/I_{\text{mob}}=0.2$, compared to 4-CT ($I_{\text{imm}}/I_{\text{mob}}=0.08$) and 4-HT (Figure 31c) which showed no immobile population (see detailed discussion on $I_{\text{imm}}/I_{\text{mob}}$ as a function of loaded spin probe concentration in Appendix D).

D. Conclusion

By concurrently analyzing the DNP frequency profile and the cw EPR lineshape of imbibed spin probes, we find that 4-AT has the largest surface-adsorbed population, indicating a higher local surface concentration when compared to 4-CT and 4-HT, which likely plays a role in determining its favorable DNP enhancement factor. More importantly, the ESEEM spectrum of 4-AT when compared with the other spin probes showed the strongest interaction specifically with the surface ^{27}Al species compared to 4-CT and 4-HT. This is the first study demonstrating the viability of targeted DNP characterization by varying the functional side groups of mono-radical spin probes. As such, it represents an important stepping-stone towards the characterization of materials surfaces “as seen by probes”. In the future, reactants and other potent chemical moieties can be spin labeled for targeted surface characterization of active sites or surfaces of interest. In order to definitively address the ultimate question of whether 4-AT selectively enhances the Al(IV) acid site over other present aluminum species in Al-SBA-15, MAS DNP must be implemented to obtain chemical shift resolution. MAS-DNP at temperatures less than 20-30 K might be desirable in order to work with dilute ^{27}Al concentrations as typical for samples relevant to catalysis. Such studies of direct surface aluminum site-specific enhancement by MAS-DNP are underway and will be the topic of future publications.

VI. Conclusion and Outlook

The work presented in this thesis has shown the potential for pulsed EPR measurements to aid in the understanding of the MAS DNP polarization process. EPR measurements have become a valuable tool for analyzing new designer DNP radicals and can aid in the direction of future DNP polarizing agents for magnetic fields of greater than 9.4 T. These EPR measurements were made possible through the development of a pulsed EPR spectrometer in Songi Han's lab operating at a B_0 field of 7 T and powered by a solid-state MW source, whose MW transmission and detection is controlled by a QO MW bridge. The versatility of the solid-state MW source and modularity of the QO transmission system enables the manipulation of the system to perform different types of measurements, such as carry out continuous wave and pulsed EPR measurements, including double resonance measurements (ELDOR). The dual EPR/DNP capabilities will greatly increase the ability to explore the DNP parameter space. The use of the VDI source that has an excitation bandwidth of 0.4 MHz when the nitroxide frequency is ~2 GHz wide at 7 T, means we are only measuring a small fraction of the electron spins in the system. The next stage in this instrument development will be to incorporate an arbitrary wave form generator at the 12 GHz stage in order to achieve chirped microwave pulses with a large excitation bandwidth. In summary, we have demonstrated that the reliability, versatility, and modularity of our dual DNP/EPR instrument creates an excellent configuration to explore the DNP performance of different samples and experimental conditions in order to study the spin physics of DNP.

The development of this EPR spectrometer allowed for the measurements of the electron spin-lattice relaxation time and spectral diffusion parameter between neighboring

electron spins. These types of EPR measurements aid in developing rationale models for describing CE DNP processes under MAS, as well as to design optimal DNP agents and choose favorable DNP experimental conditions. Literature has purposed through simulations that electron spin dynamics such as T_{1e} and spectral diffusion effect the extent to which the nuclear polarization is decreased below Boltzmann polarization when nitroxide radicals are present in the sample, but key assumptions must be validated with experiments. The work present here has shown that nuclear depolarization can cause an inflated $\epsilon_{\text{MWon/off}}$ by 60 % for bi- and tri- nitroxide radicals at 20 mM spin concentration, while the mono-radical nitroxide demonstrated no significant depolarization. We have empirically demonstrated the interplay of T_{1e} and the strength of the nuclear spin depolarization effect under MAS. The nuclear depolarization effect is due to an equalization of the electron spin polarization across the EPR line under MAS and the extent of this depolarization is strongly correlated to the T_{1e} of the nitroxide radical. Furthermore, the addition of a T_{1e} relaxing agent such as Gd^{3+} to the nitroxide spin system correspondently reduces the nuclear depolarization effect. Finally, at 20 mM electron spin concentration the pseudo spectral diffusion rate constants for the bi-, and tri- nitroxide radicals measured were all within error of each other, while the mono radical showed no spectral diffusion. Therefore, the differing depolarization factor in the various mono-, bi- and tri- nitroxide radicals is due to the variance in T_{1e} , not spectral diffusion across the EPR line. The lack of spectral diffusion observed at 20 mM spin concentration of the mono-radical nitroxide leads one to ask the question: does electron spectral diffusion need to be present in the spin system in order to observe the nuclear depolarization effect? This will be the subject of future studies where the spectral diffusion

and depolarization factor of a concentration series of the mono-radical and the bi-radical amupol will be compared.

While the With DNP measurements and simulations we were able to confirm that for our configuration, radial microwave irradiation with a constant pitch coil and sapphire rotor give the lowest microwave loss of microwaves to the sample. However the temperature gradient across the sapphire rotor is difficult to maintain and therefore measurement of temperature below 90 K we not possible. The microwave transmission can be further optimized by designing a mirror to place after the coil to reflect the transmitted microwaves back into the sample which will increase the B_1 field by a factor of 2. This reflection of the microwaves will also make EPR detection possible under MAS, further enabling DNP mechanistic studies. In order to further improve the enhancement we can take advantage of the ability to frequency modulate our microwave in order target the electron spins effect by the microwaves over the rotor period.

Finally this work has shown how direct DNP and pulsed EPR measurements can be used to determine how nitroxide spin probes are distributed in the porous of a material. By concurrently analyzing the DNP frequency profile and the cw EPR lineshape of imbibed spin probes, we find that 4-AT has the largest surface-adsorbed population, indicating a higher local surface concentration when compared to 4-CT and 4-HT, which likely plays a role in determining its favorable DNP enhancement factor. More importantly, the ESEEM spectrum of 4-AT when compared with the other spin probes showed the strongest interaction specifically with the surface ^{27}Al species compared to 4-CT and 4-HT. This is the first study demonstrating the viability of targeted DNP characterization by varying the functional side groups of mono-radical spin probes. As such, it represents an important

stepping-stone towards the characterization of materials surfaces “as seen by probes”. In the future, reactants and other potent chemical moieties can be spin labeled for targeted surface characterization of active sites or surfaces of interest. In order to definitively address the ultimate question of whether 4-AT selectively enhances the Al(IV) acid site over other present aluminum species in Al-SBA-15, MAS DNP must be implemented to obtain chemical shift resolution. MAS-DNP at temperatures less than 20-30 K might be desirable in order to work with dilute ^{27}Al concentrations as typical for samples relevant to catalysis.

References

- [1] E. K. Zavoisky, *J. Phys. USSR* **1944**, 8, 377–380.
- [2] E. K. Zavoisky, Paramagnetic Absorption in Orthogonal and Parallel Fields, **1944**.
- [3] F. Bloch, W. W. Hansen, M. Packard, *Phys. Rev.* **1946**, DOI 10.1103/PhysRev.70.474.
- [4] E. M. Purcell, H. C. Torrey, R. V. Pound, *Phys. Rev.* **1946**, DOI 10.1103/PhysRev.69.37.
- [5] R. C. deCharms, *Nat. Rev. Neurosci.* **2008**, DOI 10.1038/nrn2414.
- [6] G. Engelhardt, D. Michel, *High-Resolution Solid-State NMR of Silicates and Zeolites*, John Wiley & Sons, Norwich, **1987**.
- [7] D. A. Hall, D. C. Maus, G. J. Gerfen, S. J. Inati, L. R. Becerra, F. W. Dahlquist, R. G. Griffin, *Science* **1997**, 276, 930–932.
- [8] A. B. Barnes, G. De Paëpe, P. C. A. van der Wel, K. N. Hu, C. G. Joo, V. S. Bajaj, M. L. Mak-Jurkauskas, J. R. Sirigiri, J. Herzfeld, R. J. Temkin, et al., *Appl. Magn. Reson.* **2008**, 34, 237–263.
- [9] S. L. Veinberg, K. E. Johnston, M. J. Jaroszewicz, B. M. Kispal, C. R. Mireault, T. Kobayashi, M. Pruski, R. W. Schurko, *Phys. Chem. Chem. Phys.* **2016**, 18, 17713–17730.
- [10] F. a. Perras, T. Kobayashi, M. Pruski, *J. Am. Chem. Soc.* **2015**, 137, 8336–8339.
- [11] A. J. Rossini, A. Zagdoun, M. Lelli, A. Lesage, C. Copéret, L. Emsley, *Acc. Chem. Res.* **2013**, 46, 1942–1951.
- [12] V. Vitzthum, P. Mieville, D. Carnevale, M. A. Caporini, D. Gajan, C. Coperet, M. Lelli, A. Zagdoun, A. J. Rossini, A. Lesage, et al., *Chem. Commun.* **2012**, 48, 1988–1990.
- [13] A. J. Rossini, A. Zagdoun, M. Lelli, D. Gajan, F. Rascon, M. Rosay, W. E. Maas, C. Coperet, A. Lesage, L. Emsley, *Chem. Sci.* **2012**, 3, 108–115.
- [14] Z. Guo, T. Kobayashi, L.-L. Wang, T. W. Goh, C. Xiao, M. a Caporini, M. Rosay, D. D. Johnson, M. Pruski, W. Huang, *Chemistry* **2014**, 20, 16308–13.
- [15] A. Lund, M.-F. Hsieh, T.-A. Siaw, S.-I. Han, *Phys. Chem. Chem. Phys.* **2015**, 17, 25449–25454.
- [16] F. Blanc, L. Sperrin, D. a. Jefferson, S. Pawsey, M. Rosay, C. P. Grey, *J. Am. Chem. Soc.* **2013**, 135, 2975–2978.
- [17] O. Lafon, A. S. L. Thankamony, M. Rosay, F. Aussenac, X. Lu, J. Trébosc, V. Bout-Roumazeilles, H. Vezin, J.-P. Amoureux, *Chem. Commun.* **2013**, 49, 2864–2866.
- [18] F. Pourpoint, A. S. L. Thankamony, C. Volkringer, T. Loiseau, J. Trébosc, F. Aussenac, D. Carnevale, G. Bodenhausen, H. Vezin, O. Lafon, et al., *Chem. Commun.* **2014**, 50, 933–935.
- [19] V. Vitzthum, P. Miéville, D. Carnevale, M. a Caporini, D. Gajan, C. Copéret, M. Lelli, A. Zagdoun, A. J. Rossini, A. Lesage, et al., *Chem. Commun.* **2012**, 48, 1988.
- [20] D. Lee, N. T. Duong, O. Lafon, G. De Paëpe, *J. Phys. Chem. C* **2014**, 118, 25065–25076.
- [21] R. G. Griffin, *Nature* **2010**, 468, 381–382.
- [22] A. Lesage, M. Lelli, D. Gajan, M. A. Caporini, V. Vitzthum, P. Miéville, J. Alauzun, A. Roussey, C. Thieuleux, A. Mehdi, et al., *J. Am. Chem. Soc.* **2010**, 132, 15459–15461.

- [23] P. Wenk, M. Kaushik, D. Richter, M. Vogel, B. Suess, B. Corzilius, *J. Biomol. NMR* **2015**, *63*, 97–109.
- [24] A. Potapov, W.-M. Yau, R. Ghirlando, K. R. Thurber, R. Tycko, *J. Am. Chem. Soc.* **2015**, *137*, 8294–8307.
- [25] Q. Z. Ni, E. Daviso, T. V Can, E. Markhasin, S. K. Jawla, T. M. Swager, R. J. Temkin, J. Herzfeld, R. G. Griffin, *Acc Chem Res* **2013**, 130425010025008.
- [26] M. Renault, S. Pawsey, M. P. Bos, E. J. Koers, D. Nand, R. Tommassen-van Boxtel, M. Rosay, J. Tommassen, W. E. Maas, M. Baldus, *Angew. Chemie Int. Ed.* **2012**, *51*, 2998–3001.
- [27] A. Potapov, K. R. Thurber, W.-M. Yau, R. Tycko, *J. Magn. Reson.* **2012**, *221*, 32–40.
- [28] K. J. Pike, T. F. Kemp, H. Takahashi, R. Day, A. P. Howes, E. V Kryukov, J. F. MacDonald, A. E. C. Collis, D. R. Bolton, R. J. Wylde, et al., *J. Magn. Reson.* **2012**, *215*, 1–9.
- [29] T. Jacso, W. T. Franks, H. Rose, U. Fink, J. Broecker, S. Keller, H. Oschkinat, B. Reif, *Angew. Chemie Int. Ed.* **2012**, *51*, 432–435.
- [30] E. Salnikov, O. Ouari, E. Koers, H. Sarrouj, T. Franks, M. Rosay, S. Pawsey, C. Reiter, P. Bandara, H. Oschkinat, et al., *Appl. Magn. Reson.* **2012**, *43*, 91–106.
- [31] I. V. Sergeyev, L. a. Day, A. Goldbourn, A. E. McDermott, *J. Am. Chem. Soc.* **2011**, *133*, 20208–20217.
- [32] M. J. Bayro, G. T. Debelouchina, M. T. Eddy, N. R. Birkett, C. E. MacPhee, M. Rosay, W. E. Maas, C. M. Dobson, R. G. Griffin, *J. Am. Chem. Soc.* **2011**, *133*, 13967–74.
- [33] D. a. Hall, *Science (80-)*. **1997**, *276*, 930–932.
- [34] J. H. Ardenkjaer-Larsen, B. Fridlund, A. Gram, G. Hansson, L. Hansson, M. H. Lerche, R. Servin, M. Thaning, K. Golman, *Proc. Natl. Acad. Sci. U. S. A.* **2003**, *100*, 10158–63.
- [35] T. A. Siaw, S. A. Walker, B. D. Armstrong, S.-I. Han, *J. Magn. Reson.* **2012**, *221*, 5–10.
- [36] M. Lelli, D. Gajan, A. Lesage, M. A. Caporini, V. Vitzthum, P. Miéville, F. Héroguel, F. Rascón, A. Roussey, C. Thieuleux, et al., *J. Am. Chem. Soc.* **2011**, *133*, 2104–7.
- [37] A. Zagdoun, G. Casano, O. Ouari, M. Schwarzwälder, A. J. Rossini, F. Aussenac, M. Yulikov, G. Jeschke, C. Copéret, A. Lesage, et al., *J. Am. Chem. Soc.* **2013**, *135*, 12790–12797.
- [38] C. Song, K. N. Hu, C. G. Joo, T. M. Swager, R. G. Griffin, *J. Am. Chem. Soc.* **2006**, *128*, 11385–11390.
- [39] C. Sauvé, M. Rosay, G. Casano, F. Aussenac, R. T. Weber, O. Ouari, P. Tordo, *Angew. Chemie - Int. Ed.* **2013**, *52*, 10858–10861.
- [40] D. J. Kubicki, G. Casano, M. Schwarzwälder, S. Abel, C. Sauvee, K. Ganesan, M. Yulikov, A. J. Rossini, G. Jeschke, C. Coperet, et al., *Chem. Sci.* **2016**, *7*, 550–558.
- [41] W.-M. Yau, K. R. Thurber, R. Tycko, *J. Magn. Reson.* **2014**, *244*, 98–106.
- [42] V. K. Michaelis, A. A. Smith, B. Corzilius, O. Haze, T. M. Swager, R. G. Griffin, *J. Am. Chem. Soc.* **2013**, DOI 10.1021/ja312265x.
- [43] K. N. Hu, V. S. Bajaj, M. Rosay, R. G. Griffin, *J. Chem. Phys.* **2007**, DOI 10.1063/1.2429658.
- [44] G. Mathies, M. A. Caporini, V. K. Michaelis, Y. Liu, K. Hu, D. Mance, J. L. Zweier, M. Rosay, M. Baldus, R. G. Griffin, *Angew. Chemie - Int. Ed.* **2015**, DOI

- 10.1002/anie.201504292.
- [45] K. R. Thurber, R. Tycko, *J. Chem. Phys.* **2012**, *137*, 84508.
 - [46] F. Mentink-Vigier, U. Akbey, Y. Hovav, S. Vega, H. Oschkinat, A. Feintuch, *J. Magn. Reson.* **2012**, *224*, 13–21.
 - [47] W. L. Hubbell, A. Gross, R. Langen, M. A. Lietzow, *Curr. Opin. Struct. Biol.* **1998**, *8*, 649–656.
 - [48] A. Schweiger, G. Jeschke, *Principles of Pulse Electron Paramagnetic Resonance*, **2001**.
 - [49] S. Jawla, E. Nanni, ... *Waves (IRMMW-THz ...* **2011**, 2–3.
 - [50] V. S. Bajaj, M. K. Hornstein, K. E. Kreischer, J. R. Sirigiri, P. P. Woskov, M. L. Mak-Jurkauskas, J. Herzfeld, R. J. Temkin, R. G. Griffin, *J. Magn. Reson.* **2007**, *189*, 251–279.
 - [51] C. G. Whyte, K. Ronald, A. R. Young, W. He, C. W. Robertson, D. H. Rowlands, A. W. Cross, *IEEE Trans. Plasma Sci.* **2012**, DOI 10.1109/TPS.2012.2190271.
 - [52] Y. Hovav, D. Shimon, I. Kaminker, A. Feintuch, D. Goldfarb, S. Vega, *Phys. Chem. Chem. Phys.* **2015**, *17*, 6053–6065.
 - [53] J. Granwehr, J. Leggett, W. Köckenberger, *J. Magn. Reson.* **2007**, *187*, 266–276.
 - [54] K.-N. Hu, C. Song, H. Yu, T. M. Swager, R. G. Griffin, *J. Chem. Phys.* **2008**, *128*, 52302–52317.
 - [55] T. a. Siaw, M. Fehr, A. Lund, A. Latimer, S. a. Walker, D. T. Edwards, S. Han, *Phys. chem. chem. phys.* **2014**, *16*, 18694–18706.
 - [56] A. W. Overhauser, *Phys. Rev.* **1953**, DOI 10.1103/PhysRev.92.411.
 - [57] T. R. Carver, C. P. Slichter, *Phys. Rev.* **1956**, DOI 10.1103/PhysRev.102.975.
 - [58] T. V. Can, M. A. Caporini, F. Mentink-Vigier, B. Corzilius, J. J. Walish, M. Rosay, W. E. Maas, M. Baldus, S. Vega, T. M. Swager, et al., *J. Chem. Phys.* **2014**, *141*.
 - [59] D. Banerjee, D. Shimon, A. Feintuch, S. Vega, D. Goldfarb, *J. Magn. Reson.* **2013**, *230*, 212–219.
 - [60] a Abragam, M. Goldman, *Reports Prog. Phys.* **1978**, *41*, 395–467.
 - [61] Y. Hovav, A. Feintuch, S. Vega, *J. Magn. Reson.* **2010**, *207*, 176–189.
 - [62] C. T. Farrar, D. A. Hall, G. J. Gerfen, S. J. Inati, R. G. Griffin, *J. Chem. Phys.* **2001**, *114*, 4922–4933.
 - [63] Y. Hovav, A. Feintuch, S. Vega, *Phys. Chem. Chem. Phys.* **2013**, *15*, 188–203.
 - [64] C. F. Hwang, D. A. Hill, *Phys. Rev. Lett.* **1967**, *19*, 1011–1014.
 - [65] C. F. Hwang, D. A. Hill, *Phys. Rev. Lett.* **1967**, DOI 10.1103/PhysRevLett.18.110.
 - [66] S. (2011). D. nuclear polarization assisted spin diffusion for the solid effect case. J. of C. P. <http://doi.org/10.1063/1.352648>. Hovav, Y., Feintuch, A., & Vega, A. (2012). F. passage dynamic nuclear polarization on rotating solids. J. of M. R. <http://doi.org/10.1063/1.352648>.
 - [67] M. J. Bayro, G. T. Debelouchina, M. T. Eddy, N. R. Birkett, C. E. MacPhee, M. Rosay, W. E. Maas, C. M. Dobson, R. G. Griffin, *J. Am. Chem. Soc.* **2011**, *133*, 13967–13974.
 - [68] F. Mentink-Vigier, Ü. Akbey, H. Oschkinat, S. Vega, A. Feintuch, *J. Magn. Reson.* **2015**, *258*, 102–120.
 - [69] K. R. Thurber, R. Tycko, *J. Chem. Phys.* **2014**, *140*, 184201.
 - [70] F. Mentink-Vigier, S. Paul, D. Lee, A. Feintuch, S. Hediger, S. Vega, G. De Paepe, *Phys. Chem. Chem. Phys.* **2015**, *17*, 21824–21836.
 - [71] V. S. Bajaj, C. T. Farrar, M. K. Hornstein, I. Mastovsky, J. Vieregg, J. Bryant, B.

- Eléna, K. E. Kreischer, R. J. Temkin, R. G. Griffin, *J. Magn. Reson.* **2003**, *160*, 85–90.
- [72] A. B. Barnes, M. L. Mak-Jurkauskas, Y. Matsuki, V. S. Bajaj, P. C. a van der Wel, R. Derocher, J. Bryant, J. R. Sirigiri, R. J. Temkin, J. Lugtenburg, et al., *J. Magn. Reson.* **2009**, *198*, 261–70.
- [73] T. Idehara, K. Kosuga, L. Agusu, I. Ogawa, H. Takahashi, M. E. Smith, R. Dupree, *J. Infrared, Millimeter, Terahertz Waves* **2010**, *31*, 763–774.
- [74] A. B. Barnes, E. a. Nanni, J. Herzfeld, R. G. Griffin, R. J. Temkin, *J. Magn. Reson.* **2012**, *221*, 147–153.
- [75] N. Kumar, U. Singh, A. K. Sinha, *Infrared Phys. Technol.* **2015**, *68*, 44–51.
- [76] L. R. R. Becerra, G. J. J. Gerfen, B. F. F. Bellew, J. A. A. Bryant, D. A. A. Hall, S. J. J. Inati, R. T. T. Weber, S. Un, T. F. F. Prisner, A. E. E. McDermott, et al., *J. Magn. Reson. Ser. A* **1995**, *117*, 28–40.
- [77] L. Becerra, G. Gerfen, R. Temkin, D. Singel, R. Griffin, *Phys. Rev. Lett.* **1993**, *71*, 3561–3564.
- [78] Y. Matsuki, K. Ueda, T. Idehara, R. Ikeda, I. Ogawa, S. Nakamura, M. Toda, T. Anai, T. Fujiwara, *J. Magn. Reson.* **2012**, *225*, 1–9.
- [79] E. Bouleau, P. Saint-Bonnet, F. Mentink-Vigier, H. Takahashi, J.-F. Jacquot, M. Bardet, F. Aussenac, A. Pureau, F. Engelke, S. Hediger, et al., *Chem. Sci.* **2015**, DOI 10.1039/C5SC02819A.
- [80] T. Idehara, Y. Tatematsu, Y. Yamaguchi, E. M. Khutoryan, a. N. Kuleshov, K. Ueda, Y. Matsuki, T. Fujiwara, *J. Infrared, Millimeter, Terahertz Waves* **2015**, *36*, 613–627.
- [81] M. Lelli, A. J. Rossini, G. Casano, O. Ouari, P. Tordo, A. Lesage, L. Emsley, *Chem. Commun. (Camb)*. **2014**, *50*, 10198–201.
- [82] M. K. Kiesewetter, B. Corzilius, A. A. Smith, R. G. Griffin, T. M. Swager, *J. Am. Chem. Soc.* **2012**, *134*, 4537–40.
- [83] Y. Matsuki, T. Maly, O. Ouari, H. Karoui, F. Le Moigne, E. Rizzato, S. Lyubenova, J. Herzfeld, T. Prisner, P. Tordo, et al., *Angew. Chemie* **2009**, *121*, 5096–5100.
- [84] E. L. Dane, B. Corzilius, E. Rizzato, P. Stocker, T. Maly, A. A. Smith, R. G. Griffin, O. Ouari, P. Tordo, T. M. Swager, *J. Org. Chem.* **2012**, *77*, 1789–97.
- [85] J. Leggett, R. Hunter, J. Granwehr, R. Panek, A. J. Perez-Linde, A. J. Horsewill, J. McMaster, G. Smith, W. Köckenberger, *Phys. Chem. Chem. Phys.* **2010**, *12*, 5883.
- [86] A. A. Smith, B. Corzilius, J. A. Bryant, R. DeRocher, P. P. Woskov, R. J. Temkin, R. G. Griffin, *J. Magn. Reson.* **2012**, *223*, 170–179.
- [87] A. Feintuch, D. Shimon, Y. Hovav, D. Banerjee, I. Kaminker, Y. Lipkin, K. Zibzener, B. Epel, S. Vega, D. Goldfarb, *J. Magn. Reson.* **2011**, *209*, 136–141.
- [88] D. Goldfarb, Y. Lipkin, A. Potapov, Y. Gorodetsky, B. Epel, A. M. Raitsimring, M. Radoul, I. Kaminker, *J. Magn. Reson.* **2008**, *194*, 8–15.
- [89] Y. Hovav, I. Kaminker, D. Shimon, A. Feintuch, D. Goldfarb, S. Vega, *Phys. Chem. Chem. Phys.* **2015**, *17*, 226–244.
- [90] Y. Hovav, O. Levinkron, A. Feintuch, S. Vega, *Appl. Magn. Reson.* **2012**, *43*, 21–41.
- [91] Y. Hovav, A. Feintuch, S. Vega, *J. Chem. Phys.* **2011**, *134*, 74509–74520.
- [92] Y. Hovav, A. Feintuch, S. Vega, *J. Magn. Reson.* **2012**, *214*, 29–41.
- [93] D. Shimon, A. Feintuch, D. Goldfarb, S. Vega, *Phys. Chem. Chem. Phys.* **2014**, *16*, 6687–99.
- [94] D. Shimon, Y. Hovav, A. Feintuch, D. Goldfarb, S. Vega, *Phys. Chem. Chem. Phys.*

- 2012**, *14*, 5729–5743.
- [95] K. R. Thurber, W.-M. Yau, R. Tycko, *J. Magn. Reson.* **2010**, *204*, 303–313.
 - [96] K. R. Thurber, A. Potapov, W.-M. Yau, R. Tycko, *J. Magn. Reson.* **2013**, *226*, 100–106.
 - [97] B. D. Armstrong, D. T. Edwards, R. J. Wylde, S. A. Walker, S. Han, *Phys. Chem. Chem. Phys.* **2010**, *12*, 5920–5926.
 - [98] G. M. Smith, J. C. G. Lesurf, R. H. Mitchell, P. C. Riedi, *Rev. Sci. Instrum.* **1998**, *69*, 3924–3937.
 - [99] W. B. Lynch, K. A. Earle, J. H. Freed, *Rev. Sci. Instrum.* **1988**, *59*.
 - [100] K. a. Earle, D. S. Tipikin, J. H. Freed, *Rev. Sci. Instrum.* **1996**, *67*, 2502.
 - [101] S. Takahashi, L.-C. Brunel, D. T. Edwards, J. van Tol, G. Ramian, S. Han, M. S. Sherwin, *Nature* **2012**, *489*, 409–413.
 - [102] J. Van Tol, L. C. Brunel, R. J. Wylde, *Rev. Sci. Instrum.* **2005**, *76*, 1–8.
 - [103] F. Muller, M. A. Hopkins, N. Coron, M. Grynberg, L. C. Brunel, G. Martinez, *Rev. Sci. Instrum.* **1989**, *60*.
 - [104] M. Rohrer, O. Brüggemann, B. Kinzer, T. F. Prisner, *Appl. Magn. Reson.* **2001**, *21*, 257–274.
 - [105] P. F. Goldsmith, in *Quasioptical Syst.*, IEEE Press, **1998**, pp. 168–170.
 - [106] R. Abrams, *IEEE J. Quantum Electron.* **1972**, *8*, 838–843.
 - [107] J. L. Doane, in *Infrared Millim. Waves* (Ed.: K.J. Button), Academic Press Inc., New York, **1985**, pp. 123–170.
 - [108] J. S. Hyde, R. A. Strangeway, T. G. Camenisch, J. J. Ratke, W. Froncisz, *J. Magn. Reson.* **2010**, *205*, 93–101.
 - [109] J. van Slageren, S. Vongtragool, B. Gorshunov, a. a. Mukhin, N. Karl, J. Krzystek, J. Telser, A. Muller, C. Sangregorio, D. Gatteschi, et al., *Phys. Chem. Chem. Phys.* **2003**, *5*, 3837.
 - [110] S. Takahashi, D. G. Allen, J. Seifert, G. Ramian, M. S. Sherwin, L.-C. Brunel, J. van Tol, *Infrared Phys. Technol.* **2008**, *51*, 426–428.
 - [111] W. Low, *Phys. Rev.* **1957**, *105*, 793–800.
 - [112] F. H. Cho, V. Stepanov, S. Takahashi, *Rev. Sci. Instrum.* **2014**, *85*, 75110.
 - [113] G. W. Morley, L.-C. Brunel, J. van Tol, *Rev. Sci. Instrum.* **2008**, *79*, 64703.
 - [114] D. E. M. Hoff, B. J. Albert, E. P. Saliba, F. J. Scott, E. J. Choi, M. Mardini, A. B. Barnes, *Solid State Nucl. Magn. Reson.* **2015**, *72*, 79–89.
 - [115] F. Pourpoint, A. S. L. Thankamony, C. Volkringer, T. Loiseau, J. Trebosc, F. Aussenac, D. Carnevale, G. Bodenhausen, H. Vezin, O. Lafon, et al., *Chem. Commun.* **2014**, *50*, 933–935.
 - [116] D. Lee, H. Takahashi, A. S. L. Thankamony, J.-P. Dacquin, M. Bardet, O. Lafon, G. De Paëpe, *J. Am. Chem. Soc.* **2012**, *134*, 18491–18494.
 - [117] B. Corzilius, L. B. Andreas, A. A. Smith, Q. Z. Ni, R. G. Griffin, *J. Magn. Reson.* **2014**, *240*, 113–123.
 - [118] D. Mance, P. Gast, M. Huber, M. Baldus, K. L. Ivanov, *J. Chem. Phys.* **2015**, DOI 10.1063/1.4922219.
 - [119] T. A. Siaw, A. Leavesley, A. Lund, I. Kaminker, S. Han, *J. Magn. Reson.* **2016**, *264*, 131–53.
 - [120] H. Takahashi, C. Fernandez-De-Alba, D. Lee, V. Maurel, S. Gambarelli, M. Bardet, S. Hediger, A. L. Barra, G. De Paëpe, *J. Magn. Reson.* **2014**, DOI

- 10.1016/j.jmr.2013.12.005.
- [121] D. T. Edwards, S. Takahashi, M. S. Sherwin, S. Han, *J. Magn. Reson.* **2012**, 223, 198–206.
 - [122] S. (2011). D. nuclear polarization assisted spin diffusion for the solid effect case. J. of C. P. <http://doi.org/10.1063/1.352648>. Hovav, Y., Feintuch, A., & Vega, A.
 - [123] E. M. M. Weber, H. Vezin, J. G. Kempf, G. Bodenhausen, D. Abergel, D. Kurzbach, *Phys. Chem. Chem. Phys.* **2017**, 19, 16087–16094.
 - [124] K. R. Thurber, R. Tycko, *J. Magn. Reson.* **2009**, 196, 84–7.
 - [125] K. R. Thurber, R. Tycko, *J. Magn. Reson.* **2008**, 195, 179–86.
 - [126] E. A. Nanni, A. B. Barnes, Y. Matsuki, P. P. Woskov, B. Corzilius, R. G. Griffin, R. J. Temkin, *J. Magn. Reson.* **2011**, 210, 16–23.
 - [127] E. a Nanni, A. B. Barnes, Y. Matsuki, P. P. Woskov, B. Corzilius, R. G. Griffin, R. J. Temkin, *J. Magn. Reson.* **2011**, DOI 10.1016/j.jmr.2011.02.001.
 - [128] C. Perego, R. Millini, *Chem. Soc. Rev.* **2013**, 42, 3956–76.
 - [129] J. J. Chiu, D. J. Pine, S. T. Bishop, B. F. Chmelka, *J. Catal.* **2004**, 221, 400–412.
 - [130] W. Hu, Q. Luo, Y. Su, L. Chen, Y. Yue, C. Ye, F. Deng, *Microporous Mesoporous Mater.* **2006**, 92, 22–30.
 - [131] D. P. Serrano, J. Aguado, J. M. Escola, *ACS Catal.* **2012**, 2, 1924–1941.
 - [132] M. Werner, N. Rothermel, H. Breitzke, T. Gutmann, G. Buntkowsky, *Isr. J. Chem.* **2014**, 54, 60–73.
 - [133] Y. Jiang, J. Huang, W. Dai, M. Hunger, *Solid State Nucl. Magn. Reson.* **2011**, 39, 116–41.
 - [134] R. Wischert, P. Florian, C. Copéret, D. Massiot, P. Sautet, *J. Phys. Chem. C* **2014**, 118, 15292–15299.
 - [135] O. Lafon, A. S. L. Thankamony, M. Rosay, F. Aussenac, X. Lu, J. Trebosc, V. Bout-Roumazeilles, H. Vezin, J.-P. Amoureux, *Chem. Commun.* **2013**, 49, 2864–2866.
 - [136] O. Lafon, M. Rosay, F. Aussenac, X. Lu, J. Trébosc, O. Cristini, C. Kinowski, N. Touati, H. Vezin, J.-P. Amoureux, *Angew. Chemie Int. Ed.* **2011**, 50, 8367–8370.
 - [137] S. A. Walker, D. T. Edwards, T. A. Siaw, B. D. Armstrong, S. Han, *Phys. Chem. Chem. Phys.* **2013**, 15, 15106–15120.
 - [138] A. Schweiger, G. Jeschke, *Principles of Pulsed Electron Paramagnetic Resonance*, Oxford University Press, New York, **2001**.
 - [139] Y. Li, W. Zhang, L. Zhang, Q. Yang, Z. Wei, Z. Feng, C. Li, *J. Phys. Chem. B* **2004**, 108, 9739–9744.
 - [140] L. Lumata, M. E. Merritt, Z. Kovacs, *Phys. Chem. Chem. Phys.* **2013**, 15, 7032–7035.
 - [141] Ü. Akbey, W. T. Franks, A. Linden, S. Lange, R. G. Griffin, B.-J. van Rossum, H. Oschkinat, *Angew. Chemie Int. Ed.* **2010**, 49, 7803–7806.
 - [142] M. L. Mak-Jurkauskas, R. G. Griffin, in *eMagRes*, John Wiley & Sons, Ltd, **2007**.
 - [143] T. A. Siaw, M. Fehr, A. Lund, A. Latimer, S. A. Walker, D. T. Edwards, S.-I. Han, *Phys. Chem. Chem. Phys.* **2014**, 16, 18694–18706.
 - [144] R. a Wind, N. Zumbulyadis, R. H. Young, Y. Hung, L. Li, R. H. Nuttall, G. Maciel, *Solid State Nucl. Magn. Reson.* **1992**, 1, 55–65.
 - [145] A. Caragheorgheopol, A. Rogozea, R. Ganea, M. Florent, D. Goldfarb, *J. Phys. Chem. C* **2009**, 114, 28–35.
 - [146] L. Kevan, in *Time Domain Electron Spin Reson.*, John Wiley & Sons, **1979**, pp. 280–311.

- [147] R. Carmieli, N. Papo, H. Zimmermann, A. Potapov, Y. Shai, D. Goldfarb, *Biophys. J.* **2006**, *90*, 492–505.
- [148] G. Ionita, M. Florent, D. Goldfarb, V. Chechik, *J. Phys. Chem. B* **2009**, *113*, 5781–5787.
- [149] D. Baute, D. Goldfarb, *J. Phys. Chem. C* **2007**, *111*, 10931–10940.
- [150] S. a Walker, D. T. Edwards, T. A. Siaw, B. D. Armstrong, S. Han, *Phys. Chem. Chem. Phys.* **2013**, *15*, 15106–20.
- [151] M. Weger, *Bell Syst. Tech. J.* **1960**, *39*, 1013–1112.

Appendix

A. *The solid effect*

In 1958 the well resolved solid effect was introduced as a mechanism for the DNP polarization transfer process. The well resolved solid effect involves a dipolar coupled electron nuclear spin pair can be described using the following Hamiltonian.

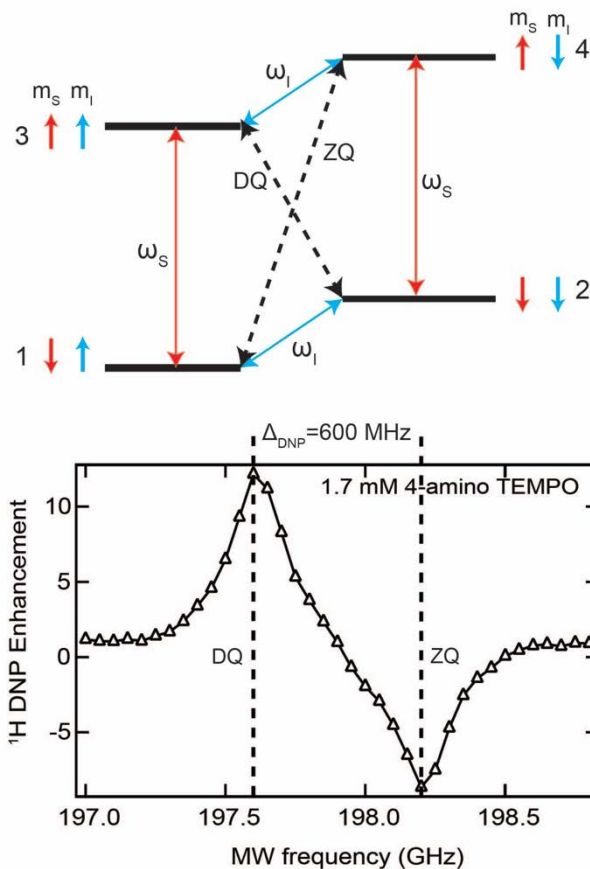
$$H = H_s + H_i + H_{is} = w_0 s S_z + w_0 i S_z + A(S_x I_x + S_y I_y + S_z I_z) + B S_x I_z$$

Where the H_{is} is the fermie contact term and H_d is the dipolar term between the electron and nuclear spin.

The energy level diagram for a spin $s=1/2$ electron spin and $I=1/2$ nuclear spin is shown in Figure A.1

The nonpseudo secular part of the hyperfine interaction has the terms $S_z I_+$ and $S_z I_-$ which leads to a mixing of states between 1 and 2, 3 and 4 in the energy diagram in Figure X. Microwave irradiation at frequency w_1 will lead to excitation of the classical forbidden transition zero quantum transition and irradiation at w_2 will lead to excitation of the double quantum transition where an electron and nuclear spins are simultaneously flipped.

The mixing of state 1 to create $1' = 1 + q_2$ second order perturbation of the nonpseudo secular part of the hamitonian. The transition proability is equal to q_2 which is proportial to $1/B_0^2$ there for the efficiency of the S.E. mechanism rapidly decreases with increasing magnetic field.



Appendix B. DNP/EPR probe details

Cryostat:

Cryogenic cooling of the sample to liquid helium temperatures $<50 \text{ K}$ can yield high nuclear spin polarization (P_n) from DNP operation when irradiating with a solid-state MW source. We recently reported as high as $P_n = 62\%$ ^[35,55,150], which is in part due to high initial P_e (83% at 4 K and 7.049 T), long T_{1e} of (10^1 - 10^2) ms found for nitroxide radicals at 4K temperatures and high spectral diffusion rate for nitroxide radicals, found at high concentrations on the order of 20 mM, which is characteristic for DNP experiments and low temperature ^[37,52,55]. In order to operate at temperatures between 4-290 K, we employ a custom STVP-200-NMR continuous flow cryostat (Janis Research Co. LLC). A Sogevac

SV65B rotary vane pump (Oerlikon Leybold Vacuum) is connected to the outlet of the cryostat to evacuate the sample chamber, while liquid helium is flowed into the inlet from a 100 L helium dewar (PraxAir) using a continuous-flow liquid helium transfer line with flow control (Janis Research Co. LLC). Precise temperature control is maintained by the heating of the incoming liquid helium with a voltage controlled resistive heater, while the temperature is simultaneously measured with a Cernox temperature sensor (Lakeshore Cryogenics). The Cernox temperature measurement and heater voltage are controlled by a LabView program where a proportional-integral-derivative (PID) algorithm controls the heater voltage output from a 0-35 V, 15 A power supply to maintain a temperature stability minimum of ± 0.02 K. The cryostat is top-loaded into the bore of the magnet, and the cryostat has a hollow bore surrounded by a vacuum jacket where the DNP probe is top-loaded into and secured with a KF-50 clamp to create a vacuum seal. Refining the choice of components to achieve greater vacuum sealing will achieve even lower temperature operation using basically the same setup.

Cryo-temperature operation

In order to operate at temperatures between 4-290 K, we employ a custom STVP-200-NMR continuous flow cryostat (Janis Research Co. LLC). Precise temperature control is maintained by the heating of the incoming liquid helium with a voltage controlled resistive heater, while the temperature is simultaneously measured with a Cernox temperature sensor (Lakeshore Cryogenics).

Probe insert:

The probe insert, shown in Fig. 2a, is a support structure that houses the MW waveguide, the NMR probe and mechanical actuators for tuning and matching the NMR circuit. This entire probe insert is top-loaded into the cryostat bore so that the final position of the NMR coil and sample is at the sweet spot of the magnet, with only a small section of the waveguide protruding out of the cryostat to capture the incoming MW beam from the MW bridge through a transparent Polymethylpentene (TPX®) aperture. The corrugated MW waveguide (Thomas Keating, LTD) is held in the center of the probe insert and consists of a hollow cylinder made of german silver that is smooth on the outside but corrugated on the inside, where the microwaves guided to the sample is in contact with these corrugations. The corrugations of the waveguide ensure minimal microwave power loss (~ 0.5 dB) of the HE₁₁ MW mode. The inner diameter (ID) of the MW waveguide is 12.7 mm for most of the length, but tapers to 5.3 mm to concentrate the microwave beam into a smaller waist compatible with the sample size along the last 70mm of the waveguide. After this waveguide taper, another short (43 mm) waveguide extension (Fig. 2b) guides the 5.3 mm waist MW beam to the sample and NMR probe located at the sweet spot of the magnet. In the microwave diagnostics section, we will analyze the performance of four different waveguide extensions constructed from copper, zirconia, and a thin layer of gold with two types of plastic supports (Fig. 2c). The NMR or EPR probe module and sample are placed at the end of the waveguide extension. The NMR probe module consists of an Alderman-Grant ¹H coil inductively coupled to a pickup loop for transmission and detection (Fig. 2d), which is a modification to the design described previously ^[35]. The inductively coupled NMR circuit enables switching between different NMR frequencies by simply replacing the NMR coil, and also allows for coils with different geometries to accommodate different sample

shapes and sizes. For example, the Alderman-Grant ^1H coil can be replaced with a 2-turn saddle coil for X channel detection (^{13}C , ^{27}Al , ^7Li , etc.). To perform EPR, the NMR probe module is replaced with an EPR probe module that consists of a solenoid field modulation coil, wound with 100 turns of 30 AWG magnet wire on an 11 mm outer diameter (O.D.) quartz tube, in order to provide B_0 field modulation for CW EPR detection (Fig. 2e).

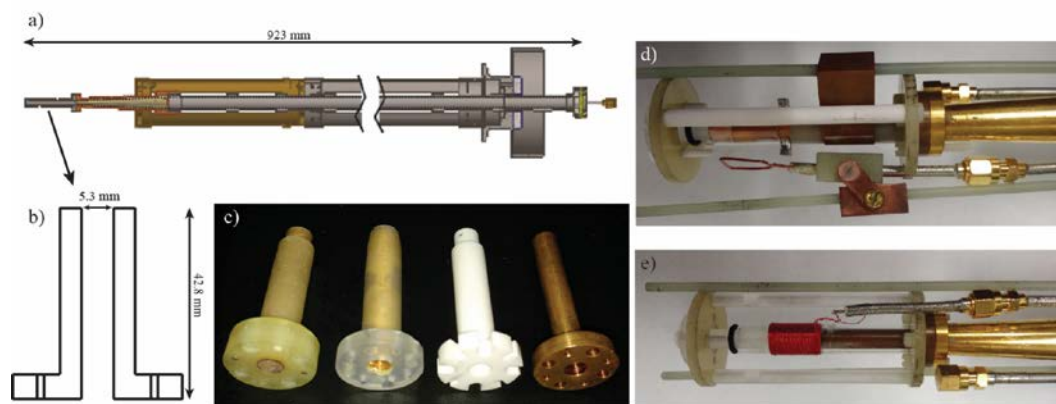


Figure 2. Details of the probe insert for NMR and EPR detection. (a) Structure of the probe insert with corrugated waveguide, (b) dimensions of the waveguide extensions, (corrugations not shown), (c) the four waveguide extensions listed from left to right: gold with Kel-F support, gold with plastic support, zirconia, and copper, (d) the probe modules with an inductively coupled ^1H Alderman-Grant coil for DNP/NMR detection, (e) a modulation coil for EPR detection.

MW bridge support structure:

The support structure for the MW bridge is mounted on top of an optical table (RS 1000TM, Newport Corp.) to minimize vibrations (although this is not so crucial for MWs in the mm-wave regime, so the optical table can be omitted). The support structure can be

constructed in any form and from any non-magnetic material that allows for vertical, horizontal, and angular position adjustment of the MW bridge relative to the orientation of the MW waveguide. The current support structure is constructed using T-slotted aluminum bars (McMaster-Carr) equipped with sliding rails (McMaster-Carr) to enable lateral movement of the bridge positioned above the superconducting magnet to allow removal of the cryostat and/or DNP probe, and to center the MW beam that couples into the waveguide. Four custom machined actuators mounted on the corners of the support structure are used for fine adjustment of the height and relative angle between the MW bridge and MW waveguide of the probe insert.

QO MW bridge:

The QO MW bridge consists of a custom machined 39.5" x 34.5" x 0.79" (width x length x thickness) aluminum breadboard for mounting the 200 GHz MW source and various QO components to form a QO circuit. They will be described separately below.

Appendix C. ^{79}Br Temperature Calibration and Stability

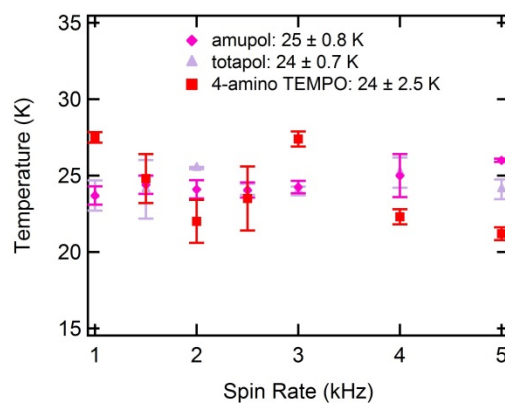


Figure C.1 T1n ^{79}Br measurement vs. Spinning Speed

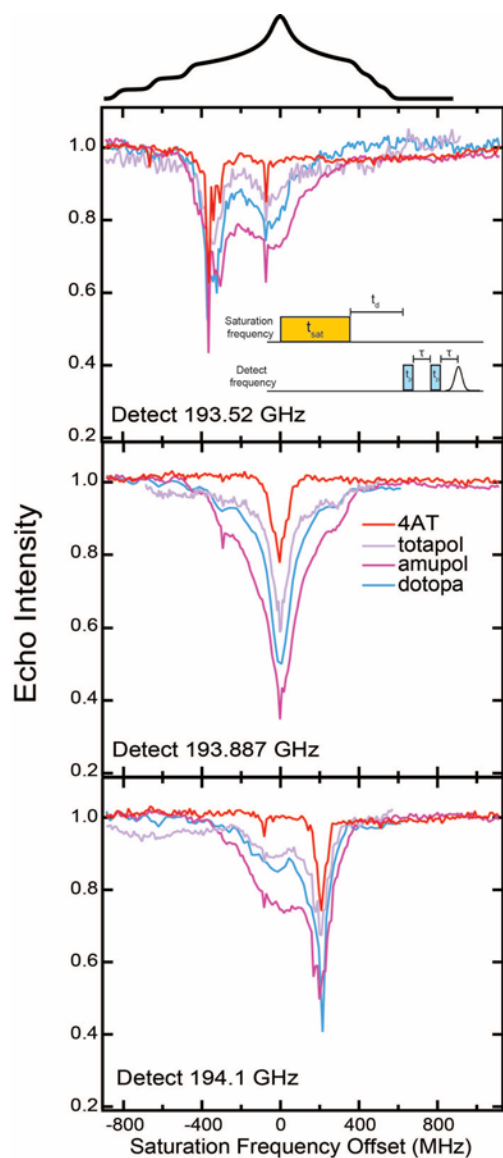


Figure C.2. ELDOR of 4AT, totapol, amupol, and dotopa at 20 mM spin concentration at detection frequencies of. (Top) 193.52 GHz, (Middle) 193.887 GHz, and (Bottom) 194.1 GHz

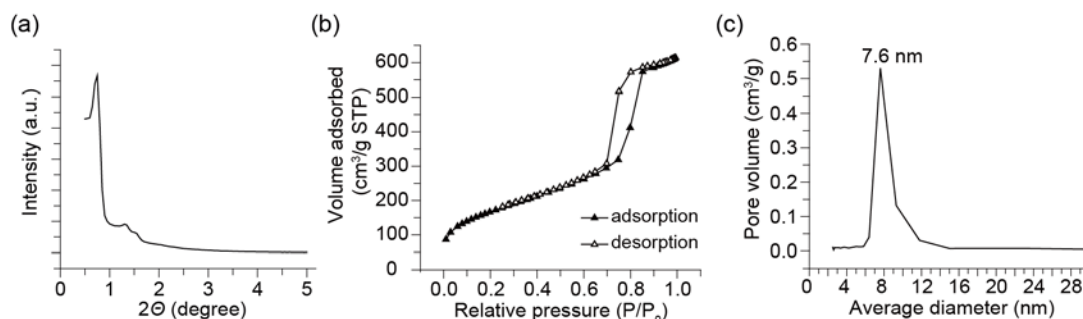
Appendix D. Supporting Information of Al-SBA-15 material

Synthesis of Al-SBA-15. The synthesis composition, conditions, and procedure followed the direct Al-SBA-15 synthesis reported by Ying *et al.*^[139] Specifically, 2.00 g of

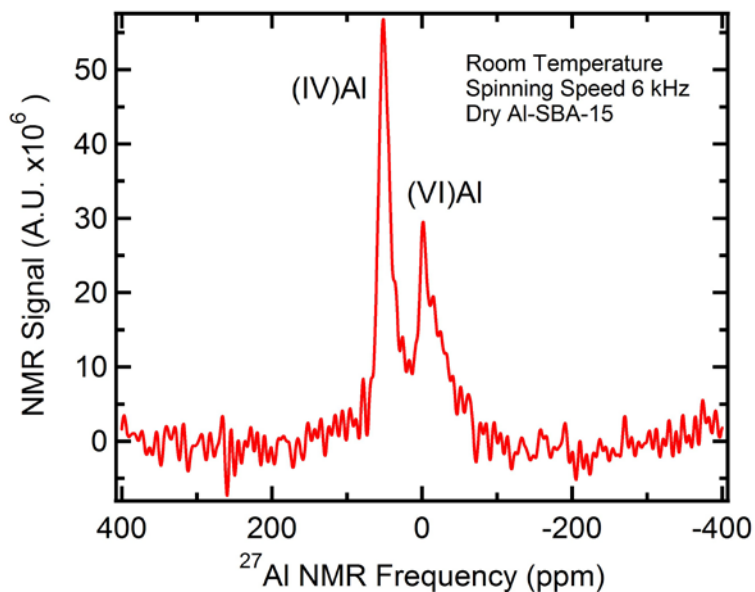
nonionic triblock copolymer surfactant EO₂₀PO₇₀EO₂₀ (P123, BASF) was dissolved in 75 mL of hydrochloric acid solution (HCl, pH = 1.5 prepared from 1N HCl_(aq), Fisher) to form solution A. Additionally, 3.27 g of tetramethyl orthosilicate (TMOS, 98 %, Sigma-Aldrich) and 0.22 g of aluminum isopropoxide (≥ 98 %, Sigma-Aldrich) were added to 5 mL of HCl_(aq) at pH = 1.5 to yield solution B with Si/Al = 20, which was vigorously stirred at room temperature for 3 h. Then, solution B was added dropwise into solution A under vigorously stirring condition, and the mixture was further stirred at 40 °C for 20 h. Subsequently, the whole mixture was transferred into an autoclave (poly(tetrafluoroethylene) (PTFE)-lined stainless steel Parr™) heated at 100 °C for 24 h. After hydrothermal synthesis, the product (designated as as-synthesized Al-SBA-15) was filtered, washed using excess deionized water, and dried at room temperature. Calcination of as-synthesized Al-SBA-15 was performed in thin beds under static air condition and followed the profile: room temperature ramp to 550 °C at 1 °C/min; hold at 550 °C for 12 h; then cool to room temperature. The resultant material was referred to as calcined Al-SBA-15.

Al-SBA-15 Characterization. The long-range order of calcined Al-SBA-15 was characterized using small-angle X-ray scattering (SAXS). The SAXS pattern (S.I. Figure 1a) was collected using a Rigaku SMART lab diffractometer and a Cu K α radiation ($\lambda = 1.5405$ Å) generated at 44 kV and 40 mA. The scanning angle range of a SAXS pattern was from 0.5 to 5.0° 2θ and the step size was set to 0.5 °/min. Elemental analysis was performed using Thermo jCAP 6300 model in Materials Research Laboratory (MRL) at UCSB, before calcined Al-SBA-15 materials were dissolved in *ca.* 2 wt % hydrofluoric acid (HF) and *ca.* 3 wt % nitric acid (HNO₃) solution at room temperature for several days. Nitrogen (N₂) adsorption/desorption isotherms (S.I. Figure 1b) were collected using the TriStar 3000

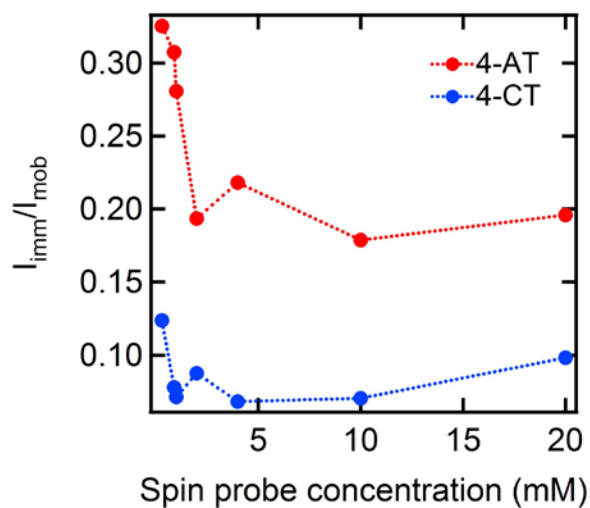
instrument. Calcined Al-SBA-15 samples were degassed under continuous N₂ flow at 200 °C overnight before the N₂ adsorption/desorption measurements. The pore size distribution curve (S.I. Figure 1c) was established using the Barrett-Joyner-Halenda (BJH) method based on the desorption isotherm.



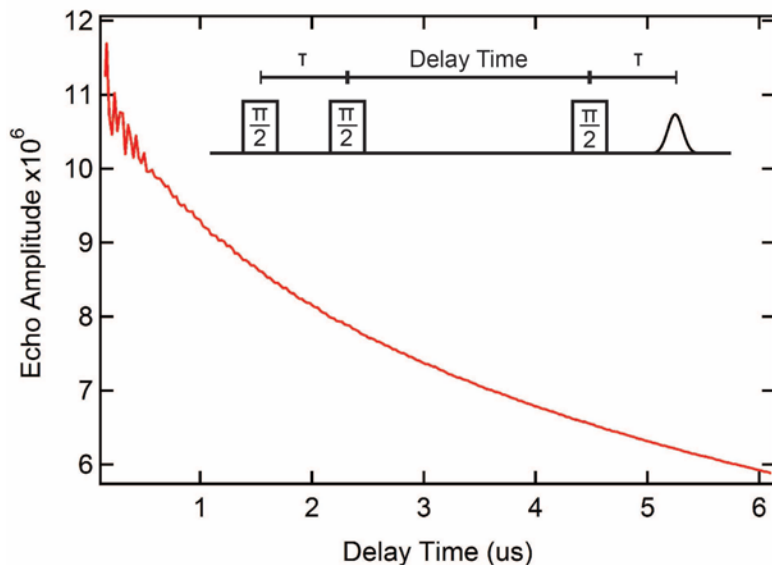
SI Figure 1. (a) Powder small-angle X-ray scattering pattern, (b) N₂ adsorption-desorption isotherms, and (c) pore size distribution of calcined Al-SBA-15.



SI Figure 2. ^{27}Al MAS NMR measured at 7 T with a custom Revolution NMR LLC MAS probe. This spectrum was measured with a one $\pi/2$ pulse measurement, with a recycle delay of 10 s using a Bruker Avance solid state spectrometer.



9.5 GHz cw EPR Instrument and Measurements. To qualitatively determine the strength of the adsorbed spin probe population of 4-AT and 4-CT the total concentration of imbibed spin probe to the Al-SBA-15 sample was varied and the $I_{\text{imm}}/I_{\text{mob}}$ determined as described in the text. S.I Figure 4 shows the $I_{\text{imm}}/I_{\text{mob}}$ dependence on total imbibed spin concentration for 4-AT and 4-CT. Most importantly, we observe an increase in $I_{\text{imm}}/I_{\text{mob}}$ with decreasing concentration of 4-AT, strongly suggesting that $I_{\text{imm}}/I_{\text{mob}}$ is a measure of relative adsorbed population that is maximal at low spin probe concentration, and whose fraction proportionally decreases with increasing 4-AT concentration that increases the fraction of free 4-AT.



240 GHz cw EPR Instrument and Measurement. To obtain the high field cw EPR spectrum the technique of rapid passage cw EPR was employed on a non-commercial EPR spectrometer operating at 8.56 T, as detailed in a previous publication.^[151] The EPR measurements are performed in induction mode with superheterodyne detection.^[101] The rapid passage method allows one to directly measure the undistorted absorption spectrum of the nitroxide line at liquid helium temperatures. Rapid passage conditions were achieved with a 8 μ L sample of 10 mM 4-amino TEMPO in a 50:40:10 v/v% d-glycerol:D₂O:H₂O solvent placed at the end of a 240 GHz waveguide at 8.56 T. A B₀ field modulation of 20 kHz, B₀ field sweep rate of 0.2 mT/s, and sweep width of 120 mT was used to directly measure the absorption cw EPR spectrum at 4 K. The frequency axis of the spectrum was linearly scaled with the gyromagnetic ration for 4-amino TEMPO.